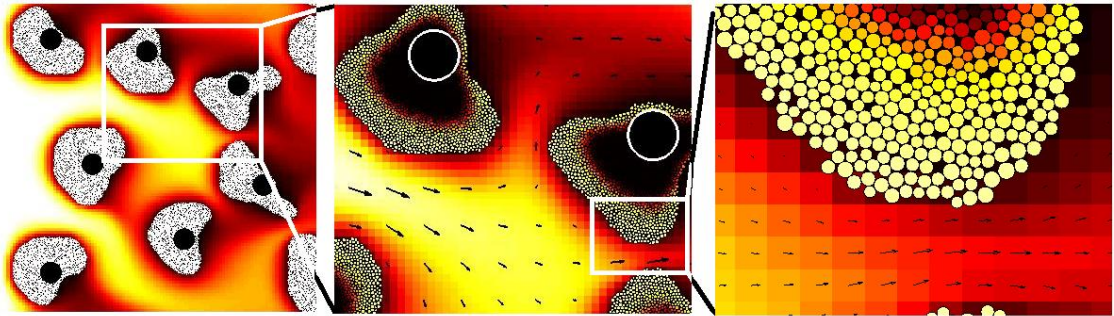


MULTI-SCALE MODELLING OF BIOFILM IN
SPONGE CARRIER MEDIA

September 2014

Magnus So

MULTI-SCALE MODELLING OF BIOFILM IN SPONGE CARRIER MEDIA



Magnus So

Graduate School of Environmental Engineering

The University of Kitakyushu

This dissertation is submitted for the degree of

Doctor of Engineering

September 2014

DECLARATION

This dissertation is the result of my own work and includes nothing, which is the outcome of work done in collaboration except where specifically indicated in the text. It has not been previously submitted, in part or whole, to any university or institution for any degree, diploma, or other qualification.

Magnus So

September 2014

Kitakyushu, Japan

ABSTRACT

This thesis describes a multiscale model of the reaction and mass transport processes in a sponge carrier media applied for waste water treatment. This was performed by dividing the sponge carrier media process into four spatial scales: reactor, sponge, biofilm and individual organisms. In this way the individual scales were modelled separately and the connection between different scales were solved by a proper set of boundary conditions. Firstly, an aerated sponge Moving Bed Biofilm Reactor (MBBR) was modelled by conducting a fluid dynamic and particle dynamic simulation, where sponge and air bubbles were simulated as particles. From the results, a pressure gradient boundary condition for the internal flow was developed. Secondly, a model of bio-clogging was performed by investigating the interaction of the biofilm growth and detachment with the porous structure of the sponge carrier media. The interaction was solved by the Lattice Boltzmann Methods (LBM) of hydraulic and mass transfer coupled with Individual-based Modelling (IbM) of the biofilm, where individual cells were modelled as particles. Finally, from analysis and generalizations of the results, a simple model for engineering purposes was developed with empirical relations of internal bio-clogging. By a new definition of a critical porosity for bio-clogging, the model could be calibrated with experimental results.

ACKNOWLEDGEMENTS

This research was carried out at the Graduate School of Environmental Engineering at The University of Kitakyushu, Fukuoka, Japan. This department are greatly appreciated for all kinds of support.

I would like to express my special appreciation and thanks to my advisor and chairman of the committee Professor Hidenari Yasui, you have been a tremendous mentor for me. I would like to thank you for encouraging my research and for allowing me to grow as a research scientist. Your advices on how to perform research, writing papers as well as on my career have been priceless.

I would like to thank my vice advisor and committee member Mitsuharu Terashima for your tremendous guidance in numerical modelling and fruitful and valuable comments during research and the writing of this thesis. I would also like to thank other committee members, Professor Kiwao Kadokami and Professor Masae Kido and for serving as my committee members even at hardship. I also would like to thank Professor Tetsuya Kusuda and Professor Atsushi Nogami for their guidance in numerical study at courses taken during my study.

I would like to thank former researcher Daisuke Naka for the efforts in organizing informative lectures regarding environmental issues. I would like to thank doctoral students Ian Jarvis and Liu Bing for valuable comments on presentations, journal papers and this thesis.

A special thanks to my family. Words cannot express how grateful I am to my mother-in law Tomoko So, father-in-law Masahiko So, my mother Margareta Hernebring, father Claes Hernebring, sister Malin Hernebring and brother Mårten Hernebring for all of the sacrifices that you've made on my behalf. I would also like to thank all of my friends who supported me in writing, and courage me to strive towards my goal. I would like to thank my beloved daughters Ellen and Julia for bringing me joy and everyday laughter. At the end I would like express appreciation to my beloved wife Reiko So who spent sleepless nights with and was always my support in the moments when there was no one to answer my queries.

CONTENTS

1 GENERAL INTRODUCTION	1
1.1 INTRODUCTION	1
1.2 SPONGE CARRIER MEDIA.....	1
1.2.1 <i>Why modelling sponge carrier media?</i>	2
1.2.2 <i>Multiple scales in sponge carrier media</i>	2
1.3 AIM AND OBJECTIVES	3
1.4 OUTLINE OF THIS THESIS	4
1.4.1 <i>Chapter 2: Literature review</i>	4
1.4.2 <i>Chapter 3: Modelling Development of a Sponge Carrier Process using CFD-DEM with Permeable Particles</i>	5
1.4.3 <i>Chapter 4: Modelling the Effect of Biofilm Morphology on Detachment</i>	5
1.4.4 <i>Chapter 5: Modelling Clogging and Biofilm Detachment in Sponge Carrier Media</i>	5
1.4.5 <i>Chapter 6: Modelling Bio-clogging of Multispecies Biofilms in Sponge Carrier Media</i>	6
1.4.6 <i>Chapter 7: Conclusions</i>	6
2 LITERATURE REVIEW.....	7
2.1 INTRODUCTION	7
2.2 BIOFILMS	8
2.2.1 <i>Brief history of biofilm research and wastewater treatment</i>	8
2.2.2 <i>Why do organisms form biofilms?</i>	8
2.2.3 <i>Dynamics of biofilm formation</i>	9
2.2.4 <i>Biofilm structure and composition</i>	11
2.2.5 <i>Metabolisms in biofilms</i>	13
2.2.6 <i>Symbiosis and competition in biofilms</i>	14

2.3 BIOFILM MODELLING	15
2.3.1 <i>History of modelling biofilms</i>	15
2.3.2 <i>Separations in time scales of biofilm processes</i>	15
2.3.3 <i>Modelling mass balance in the reactor</i>	16
2.3.4 <i>Modelling soluble flux into biofilm</i>	18
2.3.5 <i>Modelling biofilm particulate components and thickness</i>	20
2.4 BIOFILM IN POROUS MEDIA	23
2.4.1 <i>Characteristics of biofilm in porous media</i>	23
2.4.2 <i>Modelling bio-clogging in porous media</i>	24
2.5 BIOFILM IN SPONGE CARRIER MEDIA.....	26
2.6 PARTICLE METHODS FOR COMPUTATIONAL FLUID DYNAMICS	27
2.6.1 <i>Computational Fluid Dynamics</i>	27
2.6.2 <i>Modelling multiphase flow with particles and droplets</i>	28
2.6.3 <i>CFD-DEM</i>	32
2.6.4 <i>Lattice Boltzmann method</i>	32
2.7 SUMMARY OF AVAILABLE AND MISSING KNOWLEDGE	33
3 MODEL DEVELOPMENT OF A SPONGE CARRIER PROCESS USING CFD-DEM WITH PERMEABLE PARTICLES	35
3.1 INTRODUCTION.....	35
3.2 METHODS.....	37
3.2.1 <i>Model concept</i>	37
3.2.2 <i>Modelling sponge nitrification</i>	38
3.2.3 <i>Sponge hydrodynamics</i>	40
3.2.4 <i>Aeration tank model</i>	41
3.3 RESULTS.....	42
3.3.1 <i>Reactor hydrodynamics</i>	42

3.3.2	<i>Sponge effectiveness factor</i>	44
3.3.3	<i>Particle distribution and velocity with time</i>	47
3.3.4	<i>Gas hold up</i>	50
3.3.5	<i>Statistical evaluation of the shear stress in the reactor</i>	51
3.3.6	<i>Settling velocity, response time and Stokes number</i>	53
3.4	DISCUSSION	54
3.5	CONCLUSIONS	55
4	MODELLING THE EFFECT OF BIOFILM MORPHOLOGY ON DETACHMENT...	57
4.1	INTRODUCTION	57
4.2	METHODS	59
4.2.1	<i>Level Set Method</i>	59
4.2.2	<i>Implementation of local mechanical failure criteria on biofilm detachment</i>	61
4.2.3	<i>Modelled Shear Stress</i>	62
4.2.4	<i>Integration with Multidimensional Biofilm Models</i>	64
4.2.5	<i>Simulation strategy</i>	66
4.3	RESULTS	67
4.3.1	<i>Formation of biofilm with time</i>	67
4.3.2	<i>Comparison of biofilm formation under constant and pulse shear conditions</i>	68
4.4	DISCUSSION	70
4.5	CONCLUSIONS	72
5	MODELLING CLOGGING AND BIOFILM DETACHMENT IN SPONGE CARRIER MEDIA	73
5.1	INTRODUCTION	73
5.2	MODELLING FRAMEWORK	74

5.2.1	<i>LB hydrodynamics and mass transfer</i>	75
5.2.2	<i>Growth, decay and EPS degradation</i>	76
5.2.3	<i>Biofilm detachment</i>	77
5.3	RESULTS	79
5.3.1	<i>Distribution of velocity and oxygen in pores</i>	79
5.3.2	<i>Change of bio-clogging with time progression</i>	79
5.3.3	<i>Sensitivity analysis</i>	80
5.3.4	<i>Effect of operational conditions on bio-clogging in sponge carrier media</i>	81
5.3.5	<i>Long term simulation with varying rate of detachment and EPS production</i>	83
5.4	DISCUSSION	84
5.5	CONCLUSIONS	85
6	MODELLING BIO-CLOGGING OF MULTISPECIES BIOFILMS IN SPONGE CARRIER MEDIA	87
6.1	INTRODUCTION	87
6.2	METHODS	90
6.2.1	<i>Model compartments</i>	90
6.2.2	<i>Kinetic models</i>	91
6.2.3	<i>Modelling pore dispersion in a clogging sponge</i>	91
6.2.4	<i>Modelling biofilm growth and biofilm thickness</i>	92
6.2.5	<i>Modelling components in bulk liquid and clarifier</i>	93
6.2.6	<i>Simulation plan</i>	94
6.3	RESULTS	94
6.3.1	<i>Model calibration and sensitivity analysis of the monospecies model</i>	94
6.3.2	<i>Extension to multispecies model in IFAS configuration</i>	96
6.4	DISCUSSION	100

6.5 CONCLUSIONS	100
7 CONCLUSIONS.....	102
7.1 PRINCIPAL FINDINGS.....	102
7.2 THE DUAL CHARACTERISTICS OF SPONGE AS A MOVING BED AND POROUS MEDIA.....	103
7.3 FUTURE WORK.....	104
8 REFERENCES.....	106
9 APPENDICES	122

LIST OF TABLES

Table 3.1 Parameters for the CFD-DEM simulation.....	42
Table 4.1 Parameter values used in simulations	65
Table 5.1 Petersen matrix of the transformation processes in the biofilm.	76

LIST OF FIGURES

Figure 1.1. Multiple scales of a reactor with a sponge carrier media	3
Figure 2.1. Overview of the dynamics of biofilm formation: attachment, growth and detachment. P. Dirckx, Center for Biofilm Engineering, Montana State University, Bozeman, USA.....	9
Figure 2.2. Morphologies of <i>Pseudomonas aeruginosa</i> biofilms (Banin <i>et al.</i> , 2005)	12
Figure 2.3. Excretion of EPS of green algae indicated by arrows (Domozych, 2007)	13
Figure 2.4. Time scales of processes inside the biofilm (Picioreanu <i>et al.</i> , 2000) ..	16
Figure 2.5. Mass balance of soluble components (Wanner <i>et al.</i> , 2006)	17
Figure 2.6. Mass balance of particulate components (Wanner <i>et al.</i> , 2006)	18
Figure 2.7. CA biofilm model with random walking substrate diffusion (Picioreanu, 1996).....	21
Figure 2.8. IBM simulations of biofilm growth (Xavier <i>et al.</i> , 2005a)	22
Figure 2.9. Imaging of biofilm in porous media using (1) optical visualization and (2) X-ray absorption radiography (Davit <i>et al.</i> , 2011).....	24
Figure 2.10. Multiscale modelling of biofilm in porous media. Adapted from Kapellos <i>et al.</i> (2007a)	26
Figure 2.11. Photo of a sponge carrier media obtained from Seki wastewater treatment plant, Gifu prefecture, Japan.....	27
Figure 2.12. Biofilm inside sponge illuminated by FISH (Chae <i>et al.</i> , 2008).....	27
Figure 3.1. Slip velocity is affected by buoyancy forces (a), collision with walls and other particles (b) and sponge fluid response time (c).....	38
Figure 3.2. The biofilm distribution observed in a moving sponge.....	38
Figure 3.3. Flux of oxygen into biofilm ($X_A = 10 \text{ kg/m}^3$ and $l_b = 100 \text{ }\mu\text{m}$) plotted with pore oxygen concentration.	39

Figure 3.4. The different aerator configurations.....	41
Figure 3.5. Fluid velocity for the different aerators for $d = 10$ mm and $Q_A = 4$ m^3/m^2h	43
Figure 3.6. Particle spatial distribution and particle velocity for spiral roll, total floor coverage and dual spiral roll aeration configurations at $4 m^3/m^2/h$	43
Figure 3.7. Distribution of sponge slip velocity, U_s , for $d = 10$ mm and $Q_A = 4$ m^3/m^2h	44
Figure 3.8. Concentration distribution inside sponges for $d = 10$ mm, $S_{O_2,bulk} = 2$ g/m^3 and $1 \leq Da \leq 100$	44
Figure 3.9. Numerical simulation data and correlation of the effectiveness factor plotted with Damköhler numbers.....	45
Figure 3.10. Effectiveness factor for different aerator configurations, $d = 10$ mm and $S_{O_2,bulk} = 2$ g/m^3	46
Figure 3.11. Effectiveness factor for the spiral roll aerator and different sponge diameters for $S_{O_2,bulk} = 2$ g/m^3	46
Figure 3.12. Particle spatial distribution and particle velocities for different time instants for an aeration intensity of $4 m^3/m^2/h$	47
Figure 3.13. Particle spatial distribution and particle velocities for different time instants for an aeration intensity of $1 m^3/m^2/h$	48
Figure 3.14. Spatial distribution of sponge solid fraction in the reactor in the spiral roll configuration and different aeration intensities.....	49
Figure 3.15. Spatial distribution of sponge solid fraction in the reactor in the spiral roll configuration and different sponge sizes and aeration intensities.....	50
Figure 3.16. Gas hold up in the spiral roll configuration plotted with time and different aeration intensities.....	51
Figure 3.17. . Gas hold plotted with time for the different aeration configuration.....	51

Figure 3.18. Statistical probability of the shear stress at a single particle to exceed the value in x-axis during time step of 0.116 s for the different aerator configurations.	52
Figure 3.19. Statistical return period of the shear stress at each particle for the ..	52
Figure 3.20. Slip velocity plotted with time after exposure and sponge diameters.	53
Figure 3.21. Stokes number plotted with surface velocity and sponge diameters	54
Figure 4.1. The spatial domains of the biofilm and (a) the corresponding signed distance function, φ (b).	60
Figure 4.2. Modelling sloughing of biofilm by triangulating the surface points to localize possible cracks (a) and if internal stresses exceed cohesive strength, biofilm colonies are sloughed off (b).....	62
Figure 4.3. Shape of the surface plotted as the normalized roughness of the surface.	63
Figure 4.4. Fit of empirical relation in equation (4.2) (lines) against numerical results of Niavarani and Priezjev (2009) (points).	64
Figure 4.5. Illustration of particle movement during division and shoving (a-c) and the movement during decay and consolidation (biofilm shrinking) (d-f).....	66
Figure 4.6. Biofilm thickness plotted with different shear stress.	67
Figure 4.7. Biofilm morphology plotted with different shear stress. The colour scale shows the oxygen concentrations in surrounding liquid at day 30.	68
Figure 4.8. Average (solid line) and min/max values (vertical bars) of biofilm thickness shown for the 30 days constant shear.....	69
Figure 4.9. Maximum biofilm thickness at low shear conditions followed by a pulse increase of shear stress at day 30 (b).	69
Figure 4.10. Tortuosity of biofilm surface for constant shear stress and pulse shear stress conditions.	69

Figure 4.11. Biomass surface density for low shear conditions followed by a pulse increase of shear stress at day 30 (b).....	69
Figure 4.12. Effect of shear stress magnification on fraction detached biomass. ..	70
Figure 5.1. The iterative circle of the framework including hydrodynamics, mass transfer and consumption of oxygen due to microbial processes.....	75
Figure 5.2. The ratio of internal and surface detachment velocity obtained from equation (5.7) plotted with δ for different values of c	78
Figure 5.3. Contour lines of the detachment velocity function, u_{det} ($\mu\text{m}/\text{d}$) in equation (5.7) for the reference case, $k_{det} = 1000 \text{ m}^{-1}\text{d}^{-1}$ and $c = 1.6$	78
Figure 5.4. Results of oxygen (colour map), biomass distribution (white regions) and velocity distribution (arrows)($\text{g}/\text{m}^2\cdot\text{d}$) at day 10 for $S_{O_2, bulk} = 2 \text{ g}/\text{m}^3$ and $k_{det} = 1000 \text{ m}^{-1}\text{d}^{-1}$	79
Figure 5.5. Biofilm formation at day 1 (left) and day 10 (right) for $S_{O_2, bulk} = 2 \text{ g}/\text{m}^3$ and $k_{det} = 500 \text{ 1}/\text{m}\cdot\text{d}$	80
Figure 5.6. Time series of oxygen flux with the reference case and different k_{det} . The corresponding parameter sensitivity analyses at day 10 for the reference parameter sets are shown in (b).	81
Figure 5.7. Time series of permeability with the reference case and different k_{det} . The corresponding parameter sensitivity analyses at day 10 for the reference parameter sets are shown in (b).	81
Figure 5.8. Steady state oxygen flux, depending on bulk oxygen concentration and detachment coefficient k_{det}	82
Figure 5.9. Results of oxygen (grayscale), biomass distribution (white regions) and oxygen flux (numbers)($\text{g}/\text{m}^2\cdot\text{d}$) at different bulk oxygen concentrations and detachment coefficients.	82
Figure 5.10. Long term biofilm formation for the reference case, low detachment case and a case with high EPS production.....	83
Figure 5.11. Close up of the simulation at day 40 for the reference case, low detachment case and a case with high EPS production.....	84

Figure 6.1. The modelled system consisting of a mixed reactor (C_0) connected with biofilm compartments of the sponge (C_1 - C_4) by diffusive boundaries.....	90
Figure 6.2. Calibration of the mass transfer parameters k_{det} and ε_{crit} to experimental results of Matsui and Deguchi (2002).....	95
Figure 6.3. Linear regression coefficients from sensitivity analysis of the parameters in the monospecies denitrification model.	95
Figure 6.4. Soluble components in bulk liquid plotted with f_{rec}	96
Figure 6.5. Oxygen distribution in biofilm for the different compartments.	97
Figure 6.6. Variation of dissolved oxygen concentrations with f_{rec}	97
Figure 6.7. Particulate components in bulk liquid plotted with f_{rec}	98
Figure 6.8. Variation of particulate components with f_{rec} and within the biofilm grown in different compartments (C_1 - C_4) in the sponge carrier media.	99

LIST OF APPENDICES

Appendix 1. RFLOW Pre-Processor	123
Appendix 2. Nomenclature in Chapter 3	130
Appendix 3. List of Parameters Used in Chapter 4.....	132
Appendix 4. Equation derivations, Stoichiometric Tables and Parameter Lists from Chapter 6.....	134
Appendix 5. Shoving Algorithm	140
Appendix 6. Reaction, advection and diffusion Algorithm.....	141
Appendix 7. Lattice Boltzmann Method Algorithm	143
Appendix 8. Level Set Method Algorithm	145

1 GENERAL INTRODUCTION

1.1 Introduction

Every community in the world produces wastewater in some form. When untreated wastewater reaches natural water bodies it may lead to environmental and health problems caused by algal blooms, release of pathogens or toxic compounds. Wastewater treatment is therefore essential in order to protect the global environment and the public health. Biological wastewater treatment is the removal of organic compounds by the use of microorganisms. These organisms may attach to surfaces where they stick together to form biofilms. By inserting free floating carrier media, biofilm may form on their surfaces, which makes it possible to maintain high overall biomass concentration and reaction efficiency.

1.2 Sponge carrier media

Sponge carrier media is an ideal solution for upgrade of existing wastewater treatment plants (WWTP). Activated Sludge processes can be effectively upgraded by inserting sponge carrier media to create an Integrated Fixed-film Activated Sludge (IFAS) process (Morper, 1999). Upon such upgrade, a 2-3 fold increase in biomass concentrations and 1.6 increase in nitrification rates are possible (Deguchi and Kashiwaya, 1994). Sponge carrier media in Moving Bed Biofilm Reactor (MBBR) configuration can give effective post treatment of WWTP:s with high ammonia content (Morper and Linde, 2005). It is also applicable to pre-treatment for high rate partial nitritation processes (Bae *et al.*, 2014).

The reason for its efficiency is its high specific surface area of $2800 \text{ m}^2/\text{m}^3$ (carrier media basis) in its internal voids that allow large amount of biomass to attach as a biofilm (Chae *et al.*, 2008, Morper and Linde, 2005). The large amount of biomass, may on the other hand, lead to clogging in internal pores which can reduce reaction performance (Morper and Linde, 2005). In order to optimize performance of sponge carrier processes, it is of essential importance to understand the mass transfer processes in the internal voids.

1.2.1 Why modelling sponge carrier media?

Better understanding of the mass transfer processes can results in both capital and operational savings (Phillips *et al.*, 2007). Mathematical models can improve the understanding of the principal processes that are involved in the mass transfer phenomena inside fluidized sponges. One may think that mass transfer in sponge carrier media is controlled by diffusion only, but this is a very inaccurate picture. Experiments of (Matsui and Deguchi, 2002) indicated that hydraulics around the sponge carrier media has a big impact of the internal reaction rate. By modelling, the implication of this hypothesis can be investigated further.

Models can be used for applications were measurements are not possible, without disruption of the real environment. This aspect of modelling is very helpful for the case of sponge carrier media because of the difficulty of measuring concentrations of solutes within the pores of a fluidized sponge. The sponge carrier media has been modelled in past by using empirical design (Phillips *et al.*, 2007) or simple 1D models of biofilm (Lin, 2010). The problem is that these models do not take into consideration porous media inside the sponge carrier media. This is partly because of the complex behaviour of biofilms that grow inside porous structures. One may understand that flow inside porous media transport solutes to be consumed by the internal biofilm. However, the picture becomes more complicated by considering the effect of external reactor hydraulics and internal bio-clogging of the biofilm.

1.2.2 Multiple scales in sponge carrier media

Mass transfer in sponge carrier media is complex because there are many physical and chemical processes that are interacting between the reactor, sponge porous matrix and the biofilm. Figure 1.1 shows the scales of the sponge carrier media

system from the smallest organism scale to the largest reactor scale. When organisms in a biofilm grow, they exchange chemical solutes with the surrounding environment. Because of diffusive resistance within the biofilm, the distributions of solutes vary greatly from the biofilm surface to its interior which causes heterogeneities of the biofilm growth. Biofilm heterogeneities may cause problems as biofilm tends to grow near pore throats where nutrients are more abundant which may cause the biofilm to clog the passage of internal flow (Rittmann, 1993). This will affect the internal mass transfer and the biomass distribution over the entire sponge. The reactor scale determines the bulk properties of concentrations and loading rates as well as the shear stress and the pressure gradient that induces the internal flow. From these scales, a number of studies have been performed that focuses on the connections between them.

1.3 Aim and objectives

The ultimate goal of this dissertation was to understand the mass transfer processes of sponge carrier media occurring between the different scales just presented. In order to do this, interfaces between these scales have to be

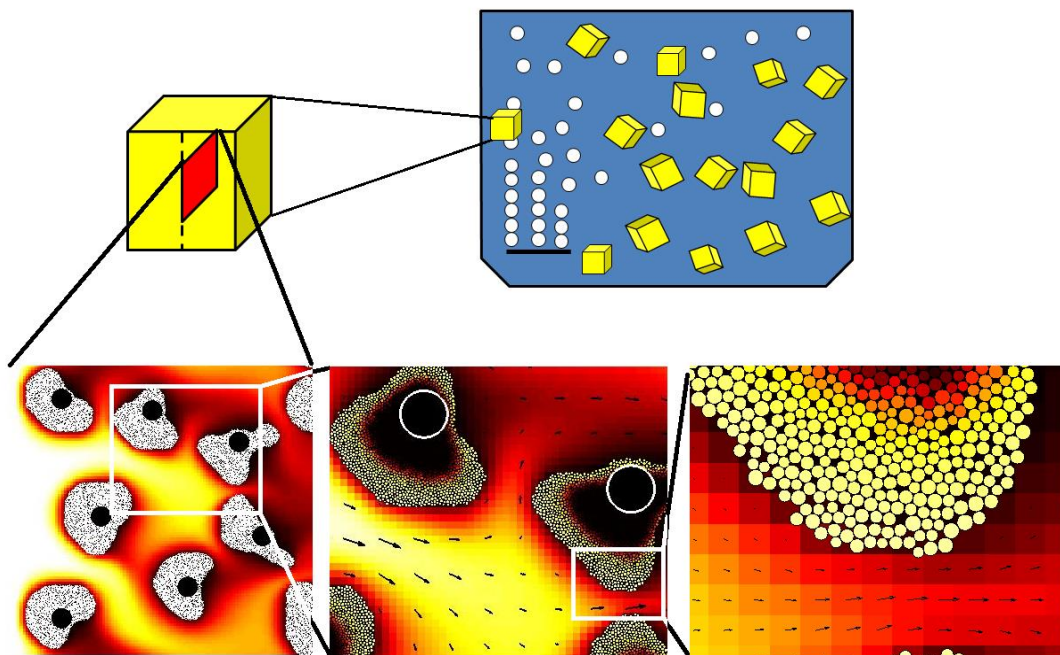


Figure 1.1. Multiple scales of a reactor with a sponge carrier media

constructed as relevant boundary conditions. The interfaces are as follows: reactor-sponge interface, biofilm-sponge interface and organisms-biofilm interface. These interfaces are each studied in detail and from the outcome of these studies a final study will bring these scales together in a simplified model.

- In the reactor-sponge interface, the aim is to understand the interaction of the reaction hydrodynamics with the internal reaction inside the sponge carrier media. This study corresponds to chapter 3, “Model Development of a Sponge Carrier Process Using CFD-DEM with Permeable Particles”.
- Organism-biofilm interface corresponds to chapter 4, “Modelling the Effect of Biofilm Morphology on Detachment”. The aim of this study is to investigate the effect of individual organisms on biofilm morphology and detachment.
- Biofilm-sponge interface corresponds to chapter 5, “Modelling Clogging and Biofilm Detachment in Sponge Carrier Media”. The aim is to study the effect of the presence of biofilm on the bio-clogging inside the sponge carrier media. This study involves interaction with the other interfaces in chapter 3 and chapter 4.
- In chapter 6, “Modelling Bio-clogging of Multispecies Biofilms in Sponge Carrier Media” the aim is to integrate the outcome of the previous studies, verify with experimental results and provide simple models of sponge carrier media that can be used by engineers.

1.4 Outline of this thesis

The outline of this dissertation includes: (1) General Background (this chapter), (2) Literature Review, (3) Modelling Development of a Sponge Carrier Process using CFD-DEM with Permeable Particles, (4) Modelling the Effect of Biofilm Morphology on Detachment, (5) Modelling Clogging and Biofilm Detachment in Sponge Carrier Media, (6) Modelling Bio-clogging of Multispecies Biofilms in Sponge Carrier Media and (7) Conclusions. A brief description of chapters 2-7 is given bellow.

1.4.1 Chapter 2: Literature review

In the literature review, a brief introduction of biofilms is given: research history, dynamics of biofilm formation and biofilm structure and composition. It is

followed by an up to date research about biofilm in porous media and how it can be applied for the sponge carrier media.

1.4.2 Chapter 3: Modelling Development of a Sponge Carrier Process using CFD-DEM with Permeable Particles

This chapter explains the reactor-sponge model interface and is the development of the boundary-value problem at the sponge carrier media surface. A computational fluid dynamics (CFD) simulation coupled with Discrete Element Method (DEM) is performed to dynamically simulate fluidized sponge carrier media inside a reactor. From the result of this simulation, a theory is formulated on how internal flow can be generated from outside hydraulic conditions.

1.4.3 Chapter 4: Modelling the Effect of Biofilm Morphology on Detachment

This chapter handles the organism-biofilm model interface and focus on how different biofilm morphologies are generated from different application of shear stress. By the use of Individual-based Modelling (IbM) of biofilms (Kreft *et al.*, 2001), the growth of individual cells are simulated in 2 dimensions. By cell division due to bacterial growth, a cluster of bacterial cells are formed which resemble the biofilm. The competition for substrates between individual cells is modelled by solving a system of partial differential equations covering reaction and diffusion phenomena inside the biofilm. Due to application of shear stress, there is a limit of the roughness of the biofilm surface due to biofilm detachment. An empirical relation for the effect of morphology on the local fluid shear stress is developed. From this relation, biofilm detachment is assumed to occur whenever the fluid shear stress exceeds the biofilm cohesiveness. By theoretical justification, a model for the biofilm detachment within a sponge carrier media is derived.

1.4.4 Chapter 5: Modelling Clogging and Biofilm Detachment in Sponge Carrier Media

In this chapter, a 2 dimensional model of biofilms grown in the internal pore space of the sponge carrier media is constructed. Biofilm was simulated using IbM and the hydraulics and oxygen mass transfer around pore structures and biofilm was simulated in detail using Lattice Boltzmann CFD methods (Succi, 2013). The effect

of limiting substrate concentration (oxygen) and detachment on internal bio-clogging will be demonstrated.

1.4.5 Chapter 6: Modelling Bio-clogging of Multispecies Biofilms in Sponge Carrier Media

This study focused on the integration of models by relevant simplifications that could be made based on realizations in previous studies. Bio-clogging was assumed to manifest as a transition point between pore molecular diffusion and advection at a critical hydraulic porosity of the sponge carrier media. This transition point was calibrated by comparisons with experimental results. In order to simulate Simultaneous Nitrification and Denitrification (SND), the model was extended with a multispecies model including heterotrophs, Ammonia Oxidizing Organisms (AOO) and Nitrite Oxidizing Organisms (NOO).

1.4.6 Chapter 7: Conclusions

Conclusions explain the principal findings from the chapters 3-6 and their implications and how different results between studies are connected with each other. It also shows how well the modelling results are in agreement of the initial hypothesis that biofilm in sponge carrier media behave similarly to biofilm in soils and that models of biofilm in soils should apply well for the description of sponge carrier media

2 LITERATURE REVIEW

2.1 Introduction

Biomass in sponge carrier media grows as biofilm. Understanding of these sessile communities is essential in order to understand the mechanisms of mass transfer in sponge carrier media. Sponge carrier media behave differently from other carrier media because of the internal porous matrix. The interaction between the biofilm and the porous matrix depend on various processes: biofilm growth, decay, detachment and bio-clogging. The literature review chapter is outlined as follows:

- The next subsection starts by presenting biofilms in general, for example: history, dynamics of biofilm formation, detachment and the role EPS.
- The third subsection deals with mathematical models of biofilms from simple empirical models to complex individual based models.
- The forth subsection presents biofilm in porous media and state of the art modelling in the field.
- Experimental work on biofilm in sponge carrier media is presented in fifth subsection.
- This is followed by a brief introduction of Computational Fluid Dynamics (CFD) in the sixth subchapter.
- Finally, the available and the missing knowledge in the field are summarized.

2.2 Biofilms

2.2.1 Brief history of biofilm research and wastewater treatment

In 1684, in a report to the Royal Society of London, Anthony van Leeuwenhoek reported the vast accumulation of microorganisms on dental plaque (van Leeuwenhoek and Dobell, 1932). Robert Koch (1843-1910) studied individual bacteria, and provided cure for serious diseases such as anthrax and tuberculosis. He developed approaches such as the pure culture methods that became the standard for all microbial infectious research. However, the focus on pure culture was so concentrated, that relevant questions regarding organisms in fixed culture were left aside.

In late 1870's the nutrient removal effect of irrigation fields was realized which lead to the development of the first trickling filter in 1903 which consists of tower with rock media inside, where wastewater is filtered from the top (Wiesmann *et al.*, 2007). However in these times, the mechanisms of biofilm nutrient removal were unknown and with the development of activated sludge treatment in 1912 (Ardern and Lockett, 1914), a major part of wastewater treatment was shifted to suspended culture technology (Benidickson, 2011). In 1920's and 1930's, interests of fixed microorganisms attached to surfaces emerged by studies on slimes on ships (Hilen, 1923), wastewater treatment systems and soil micro flora (Conn, 1932).

In the mid 1970's, Geesey *et al.* (1977) showed that biofilm are the natural habitat to microorganisms and that most microbes (about 99%) in nature are attached as biofilms. It was not until this time biofilm research intensified, which had a great impact on various fields such as environment, industry, health dentistry and medicine. Development of the first IFAS and MBBR biofilm technologies with sponge or plastic media were developed in the late 1980's and were great commercial successes (Morper and Linde, 2005, Odegaard *et al.*, 1993).

2.2.2 Why do organisms form biofilms?

Even though microorganisms in biofilms are limited by diffusion of oxygen and substrate for growth, the biofilm mode of growth gives several competitive advantages against the planktonic counterparts. This was studied by Jefferson

(2004) in human infections. The advantages for the biofilm mode of growth could be categorized into four groups: (i) defence, (ii) colonization, (iii) community and (iv) default mode of growth. Biofilm can be used as a defence as it is resistance to shear forces and the organisms can better withstand nutrient deprivation, pH changes, oxygen radicals, disinfectants and antibiotics. Attachment of planktonic organisms to surfaces to create biofilms can be used as a mechanism to colonize and remain in place in favourable environments. Observations of coordinated multicellular behaviour such as division of labour and quorum sensing has brought the view of biofilms as a corporate community or even as a multicellular organisms (Shapiro, 1998). By observations of biofilms grown on rock surfaces and planktonic organisms in lake water, Costerton (1978) brought the insight that most bacteria in nature exist in the form of a biofilm rather than in planktonic form.

2.2.3 Dynamics of biofilm formation

The dynamics of biofilm formation is illustrated in Figure 2.1 which includes: attachment, growth and detachment. A brief description of each development stage will be presented.

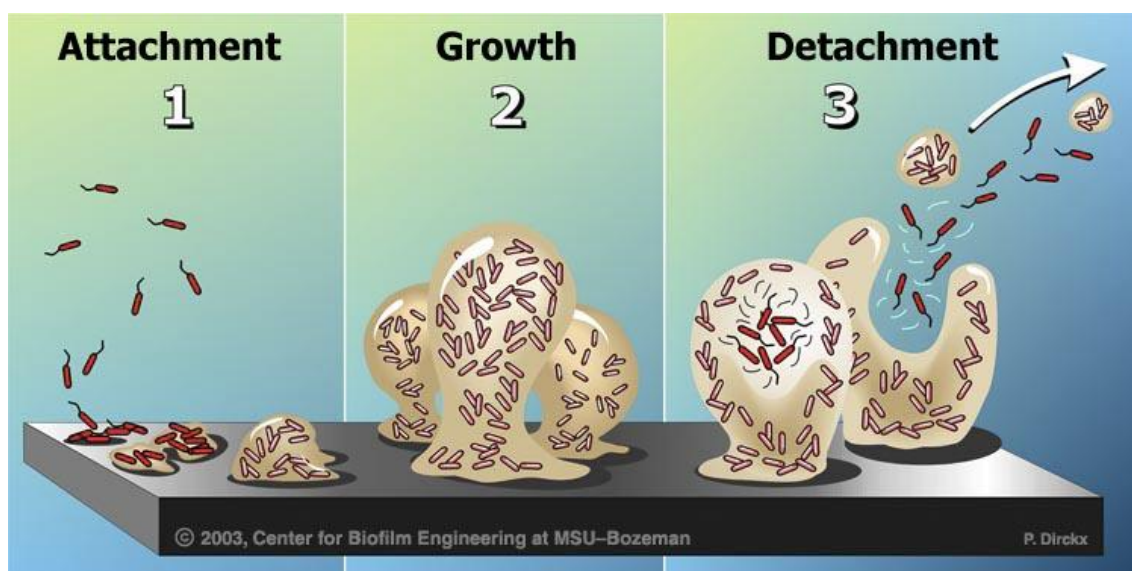


Figure 2.1. Overview of the dynamics of biofilm formation: attachment, growth and detachment. P. Dirckx, Center for Biofilm Engineering, Montana State University, Bozeman, USA.

2.2.3.1 Attachment

Biofilm attachment is the process where planktonic microorganisms adhere to surfaces or existing biofilms, and thereby becoming a part of a biofilm community. Biofilm attachment can be either passive or active. Passive biofilm attachment refers to effect of the environmental conditions on the microorganisms such as local hydrodynamics, Brownian movements and sedimentation (Ginn *et al.*, 2002). Active biofilm attachment is caused by the motility of the cells in various ways for example swimming with their flagella and buoyancy modifications for vertical motions (Bardy *et al.*, 2003). In the primary stage, attachment is reversible as the adhesive bounds to the surface are mostly weak van-der Waals forces. In the secondary stage, after which the initial colony have started to excrete Extracellular Polymeric Substances (EPS), attachment becomes irreversible as new planktonic cells are easily entrapped to the cohesive EPS matrix (Dunne, 2002).

2.2.3.2 Growth and maturation

After the organisms are being attached they immediately start to produce EPS that works as a glue to hold the biofilm together. The young biofilm starts to expand by cell division and EPS secretion, creating 3-dimensional structures of biofilms. Growth rates are affected by biological factors (species, predation) and physio-chemical factors (hydrodynamics, nutrient availability, pH etc). When biofilm thickness approaches the critical thickness of substrate penetration depth, growths rates slow down by diffusion limitation. Diffusion limitation causes stratification of substrates near biofilm surface which causes minor heterogeneities at the surface to be augmented, resulting in a finger shaped biofilm morphology (Picioreanu *et al.*, 1998).

2.2.3.3 Detachment and dispersal

Detachment and dispersal is the last step in the growth cycle where microorganisms are being released to the surrounding liquid. Biofilm detachment is considered to be the main mechanism to control growth in biofilm reactors (Rittmann *et al.*, 1992). It determines the steady state accumulation, solids retention time (SRT) and hence also the composition of the microorganisms occupying the biofilm (Morgenroth and Wilderer, 2000).

Bryers (1988) identified five different subgroups of biofilm detachment: erosion, sloughing, abrasion, human intervention, predator grazing. Erosion is considered as a continuous release of biomass at the surface caused by a surface shear stress. Sloughing is the release of chunks of biomass caused by internal mechanical failure. These two groups are common biofilm reactors and may be the result of reactor shear stress such as fluid shear stress (Peyton and Characklis, 1993, Picioreanu *et al.*, 2001, Rittman, 1982). Abrasion is the detachment caused by collision forces of between carrier media and is the dominated detachment process in MBBR (Gjaltema *et al.*, 1997, Tijhuis *et al.*, 1996). Human intervention is the detachment of biofilm caused by human activity for example cleaning of surfaces or adding EPS degrading enzymes to remove undesired biofilm in industrial and medical applications (Allison *et al.*, 1998, Boyd and Chakrabarty, 1995). Predator grazing is common for naturally grown biofilm were protozoa, insects and various vertebrates feed on the biofilm.

The groups of detachment identified by Bryers support the view of detachment as a passive process that results solely from the interaction of the biofilm with its surrounding environment, however recent research also suggest active components triggered by the organisms themselves. In *Pseudomonas aeruginosa* biofilms, certain EPS degrading enzymes are triggered by nutrient depletion which cause breakage and detachment of the biofilm (Boyd and Chakrabarty, 1995). This may work as a trigger for the organism to disperse to planktonic form and colonize new nutrient-rich environments (Jefferson, 2004). Biofilm detachment can also be controlled by quorum sensing and it has been found to be triggered in experiments by either inactivating (Hentzer *et al.*, 2002) or activating (Boles and Horswill, 2008) different types of quorum sensing signals.

2.2.4 Biofilm structure and composition

2.2.4.1 Biofilm heterogeneity

Biofilms are heterogeneous structures. Bishop and Rittman (1995) classified the heterogeneity of biofilms in four categories: (i) geometrical heterogeneity, (ii) chemical heterogeneity, (iii) biological heterogeneity and (iv) physical heterogeneity. Geometrical heterogeneity can be seen as a mushroom morphology

in Figure 2.2 which is the result of diffusion limitation described in previous section (2.2.3.2). Diffusion limitation also causes a chemical heterogeneity because of stratification of the limiting substrate being utilized in the biofilm. The stratification of the biofilm can promote biological heterogeneity, for example aerobic nitrifiers can live in the oxic parts of the biofilm surface, whereas denitrifying species live further inside the biofilm where oxygen has been depleted by the surface organisms. The porosity of the biofilm also varies in space as a more porous biofilm is commonly observed near the surface of the biofilm. This causes a physical heterogeneity of mechanical strength as porosity of biofilm is related to the mechanical strength (Ohashi and Harada, 1994). The fluffy biofilm near the surface easily detaches whereas the compact biofilm further inside can effectively resist mechanical stresses from the environment. Biofilm mechanical strength may also be affected by the available EPS.

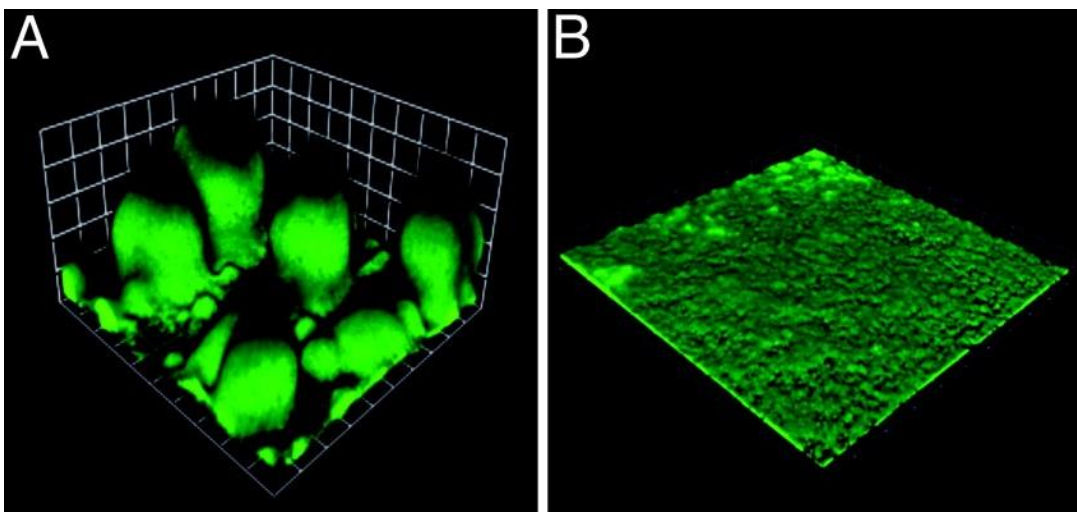


Figure 2.2. Morphologies of *Pseudomonas aeruginosa* biofilms (Banin *et al.*, 2005)

2.2.4.2 The role of extracellular polymeric substances on biofilm cohesion

EPS is the cohesive matrix of polymers produced by the organisms in the biofilm and constitute of about 50% to 90% percent of the organic matter (Wingender *et al.*, 1999). Production of EPS of green algae in a biofilm is shown Figure 2.3. The view of EPS as a binding material of the biofilm was suggested by Wilderer and Charaklis (1989): "organic polymers of microbial origin which in biofilm systems are frequently responsible for binding cells and other particulate materials together (cohesion) and to the substratum (adhesion)". Experimental works of

Ohashi and Harada (1994) indicated that the concentration of EPS in the biofilm did not have any impact on biofilm cohesion. However, there is experimental evidence that polysaccharides in EPS have a major role in biofilm cohesiveness (Boyd and Chakrabarty, 1995) as well as multivalent cation such as calcium and magnesium (Chen and Stewart, 2002). Contrary to Ohashi and Harada, Ahimou *et al.* (2007) observed a significant increase of cohesiveness with the increase of total EPS and fraction of polysaccharides. Contradicting experimental results can be an effect of different experimental methods or the complexity of EPS as it is composed of a diversity of macromolecules with diverse functionality, including polysaccharides, proteins, nucleic acids and lipids (Nielsen *et al.*, 1996).

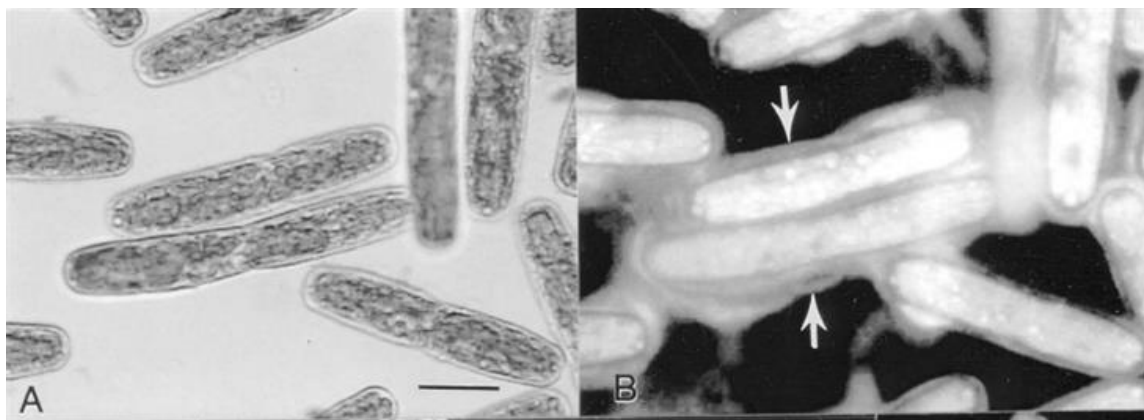


Figure 2.3. Excretion of EPS of green algae indicated by arrows (Domozych, 2007)

2.2.5 Metabolisms in biofilms

Numerous sorts of metabolisms can occur in biofilms which can be categorized in various ways according to how different species utilize nutrients and energy. The first distinction is regarding how the organisms obtain energy for living and growing, where chemotrophs utilize energy from chemical reactions and phototrophs utilize energy from sunlight. Another distinction is based on the reducing equivalents where lithotrophs obtain reducing equivalents from inorganic compounds and organotrophs obtain reducing equivalents from organic compounds. The final distinction relates to the source of carbon to be synthesised for biomass where autotrophs may utilize carbon dioxide whereas heterotrophs utilize carbon from organic compounds.

Heterotrophic organisms are more precisely defined as chemoorganoheterotrophic because they are chemotrophs that use organic compounds as both carbon and energy sources. They are very abundant in nature and are the major biomass component in municipal wastewater treatment plants. They are fast growers and utilized for their ability to degrade COD and the ability of some heterotrophic organisms to remove nitrogen oxides by denitrification.

Autotrophs means self-feeding and are the producers of the food chain. Although photoautotrophs are very common in nature, bioreactors consist mainly of chemoautotrophs that can be divided into the following groups: methanogens, halophiles, sulfur oxidizers and reducers, nitrifiers, anammox bacteria, and thermoacidophiles. Nitrifying organisms are common in wastewater treatment plants and utilized for their ability to reduce ammonia to nitrite or nitrate. They can be subdivided into Ammonia Oxidizing Organisms (AOO) that convert ammonia [NH₃] or ammonium [NH₄⁺] into nitrite [NO₂⁻] and Nitrite Oxidizing Organisms (AOO) that convert nitrite to nitrate [NO₃⁻]. Application of anammox (ANAerobic AMMONium OXidation) bacteria in wastewater treatment has recently received a lot of attention for the reaction that simultaneously reduce ammonia and nitrite to dinitrogen (van de Graaf *et al.*, 1990). With combination of AOO, total nitrogen removal can be performed with less oxygen consumption than conventional nitrification and denitrification, which means potential energy saving with minimum use of aerators.

2.2.6 Symbiosis and competition in biofilms

Metabolic symbiosis can appear in biofilm. Some species can utilize substrates that are produced by others. A typical example is Simultaneous Nitrification and Denitrification (SND) where nitrifiers converts ammonia to nitrogen oxides which can be denitrified by heterotrophic organisms. Denitrification also increases alkalinity which benefits nitrifiers. Another type of symbiosis occurs within the EPS matrix where exchange of genetic materials have been observed (Kreth *et al.*, 2009).

The dense population of organisms causes competition of the available nutrients. Nitrifiers can be outcompeted by fast growing aerobic heterotrophs for the

competition of oxygen. Some species may release antimicrobial substances in order to destroy or inhibit neighbouring cells (James *et al.*, 1995). In some biofilms, predator-prey interaction can significantly affect biofilm development, morphology and bacterial species (Núñez *et al.*, 2005).

2.3 Biofilm modelling

2.3.1 History of modelling biofilms

The first biofilm models were simple empirical “black-box” models of trickling filters (National Research council, 1946). Those empirical models are derived from a large set of data under relevant operating conditions. However, they cannot be used for operating conditions outside the validated range of the model and provide little insight into biofilm mechanisms (Wanner *et al.*, 2006). In the 1970s, incorporation of fundamental mechanisms of substrate flux and diffusive transport into the biofilm was performed (Harris and Hansford, 1976). These models could capture the decline of substrate reduction along the depth of the biofilm. In the 1980’s, models were developed for multiple substrates and multiple species with non-uniform distribution of biomass (Kissel *et al.*, 1984, Wanner and Gujer, 1985). At that time, it was not clear whether the assumptions neglected significant biofilm phenomena and the need of more mechanistic models were pointed out by Charaklis *et al.* (1989). Starting from the beginning of the 1990s and carrying on today, mechanistic multidimensional models incorporating biofilm morphology are under development (Hermanowicz, 1998, Picioreanu *et al.*, 1998, Wimpenny and Colasanti, 1997).

2.3.2 Separations in time scales of biofilm processes

Biofilm formation involves different processes that occur in a vast range of time scales up to 10 orders of magnitude. The processes for the different time scales are shown in Figure 2.4 and are sorted in three different observation windows: hydrodynamics, mass transport and biofilm structure. Each window contains a set of processes that have about the same ranges characteristic time. The processes outside the observation window have time scales that are different from the ones under interests and do not interact with processes within the observation window.

By a proper mathematical model construction, the separation of time scales makes it possible to reduce computational time without losing the accuracy. The processes that are much slower than the observation window can be regarded as “froze state”. For example the characteristic time for growth, detachment and decay is much longer than the characteristic time for the substrate to diffuse and be consumed by the biofilm. This means that reaction and diffusion can be calculated over a biofilm structure that does not change in shape within the time mass transport occurs. In the same way, processes that are much faster than the observation window can be regarded as pseudo-steady state. For example the reaction-diffusion processes can create a steady state oxygen profile within the biofilm which remain unchanged within the time of the observation window.

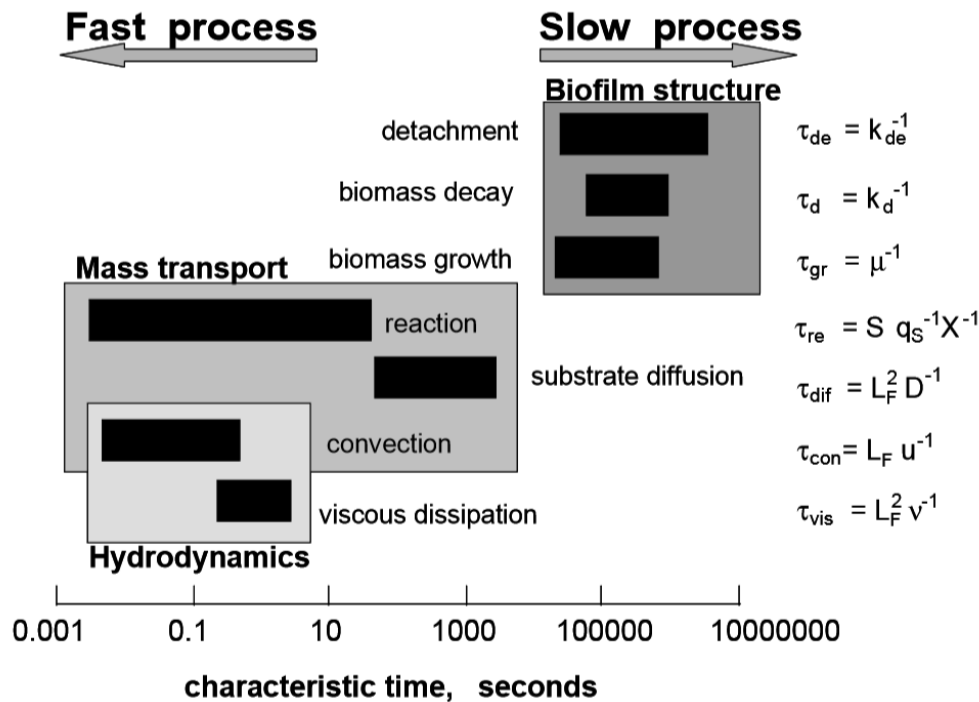


Figure 2.4. Time scales of processes inside the biofilm (Picioreanu *et al.*, 2000)

2.3.3 Modelling mass balance in the reactor

In order to calculate the reaction inside the biofilm it is necessary to set up a mass balance for the soluble (S_i) and particulate components (X_i) in the bulk liquid. The mass balance for the soluble components is shown in Figure 2.5 and for a reactor of volume V with influent flow Q_{in} it is given by

$$\frac{\partial S_{i,L}}{\partial t} = \frac{Q_{in}}{V} (S_{i,in} - S_{i,L}) - j_i a_F + r_{i,L} \quad (2.1)$$

where $r_{i,L}$ is the reaction rate in the liquid, j_i the flux into the biofilm and a_F the specific surface area of the biofilm. Similarly, mass balance of X_i in the bulk liquid is illustrated in Figure 2.6 and is given by

$$\frac{\partial X_{j,L}}{\partial t} = \frac{Q_{in}}{V} (X_{j,in} - X_{j,L}) - (k_{att} X_{j,L} + u_{det} X_{j,LF}) a_F + (\mu - b) X_{j,L} \quad (2.2)$$

where k_{att} is the attachment coefficient, u_{det} the detachment velocity and subscript LF means liquid-biofilm interface. For the case which the reaction is limited only on component i , it can be expressed as a Monod rate expression as follows

$$r_i = -q_{max,i,j} \frac{S_i}{S_i + K_{i,j}} X_j \quad (2.3)$$

where $q_{max,i}$ is the maximum specific utilization rate and K_i is the affinity coefficient and X_j is the concentration of biomass.

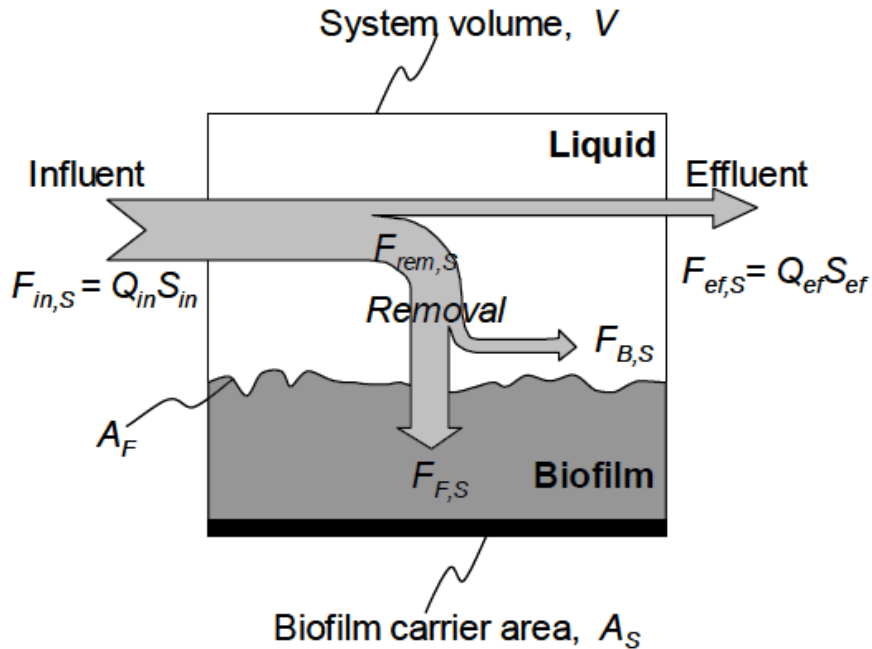


Figure 2.5. Mass balance of soluble components (Wanner *et al.*, 2006)

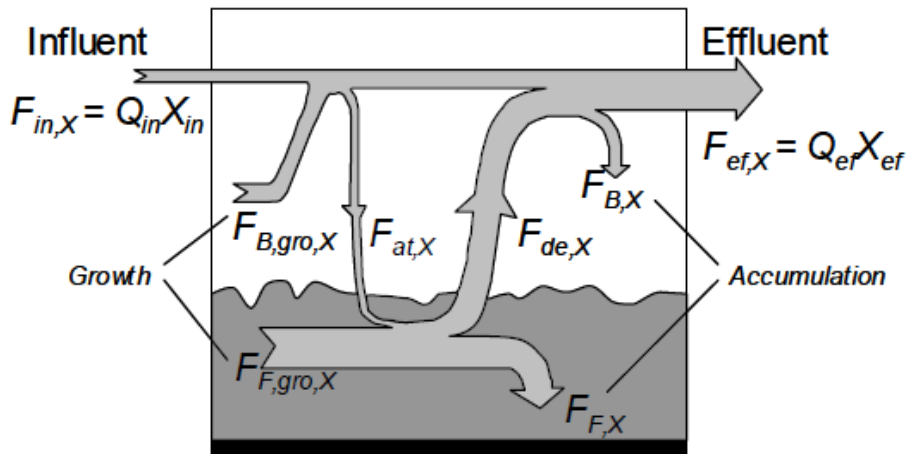


Figure 2.6. Mass balance of particulate components (Wanner *et al.*, 2006)

2.3.4 Modelling soluble flux into biofilm

In order to calculate the flux of substrate into a biofilm, the diffusion processes have to be taken into account. This subchapter explains how this can be achieved by empirical, analytical or numerical methods.

2.3.4.1 Empirical apparent affinity coefficients

The simplest expression of biofilm and floc kinetics involve the use of apparent affinity coefficients, $K_{i,app}$ to express the reaction with bulk concentrations $S_{i,L}$. To compensate for the lower internal substrate due to diffusion resistance $K_{i,app}$ is larger than the inherent value K_i . The advantages of these types of models is that the Monod rate expressions can be kept with only minor modification of the ASM models (Henze *et al.*, 2000). The flux into the biofilm can be expressed as

$$j_{i,F} = q_{\max,i,j} \frac{S_{i,L}}{S_{i,L} + K_{i,app}} X_{j,F} \delta_F \quad (2.4)$$

where δ_F is the biofilm thickness. $K_{i,app}$ depend on the size and characteristics of the biofilm or flocs. Pérez *et al.* (2005) suggested the following approximation for spherical flocs or biofilm granules of radius R_p

$$K_{i,app} = 1.84 \cdot 10^{-2} \frac{q_{\max,i,j} X_{j,F} R_p^2}{D_i} \quad (2.5)$$

2.3.4.2 Analytical biofilm models

Analytical models solve the biofilm diffusion-reaction equations by imposing simplifications on the reaction kinetics for which analytical solutions exist. Monod type reactions can be approximated as zero order reaction rate $r_i^{(0)}$ if $S_{i,L} \gg K_i$, as follows

$$r_{i,F} = -q_{\max,i,j} X_{j,F} \frac{S_i}{S_i + K_i} \approx -q_{\max,i,j} X_{j,F} \quad (2.6)$$

For zero order reaction kinetics, the flux into the biofilm is the reaction multiplied by the thickness of the active region in the biofilm

$$j_{i,F}^{(0)} = -r_{i,F}^{(0)} \delta_{active} \quad (2.7)$$

The active region is either limited by the biofilm thickness δ_F or the substrate penetration depth, δ_p whichever is the lowest

$$\delta_{active} = \min(\delta_F, \delta_p) \quad (2.8)$$

The substrate penetration depth is given by (Harremoes, 1978, Levenspiel, 1962)

$$\delta_p = \sqrt{\frac{2 \cdot D_i \cdot S_{LF,i}}{q_{\max,i,j} X_{j,F}}} \quad (2.9)$$

Because of the half order dependence of $S_{LF,i}$ on δ_p , the assumption of zero order reaction kinetics within the biofilms leads to an apparent reaction with half order kinetics for thick biofilm ($L_B > \delta$) and zero order kinetics for thin biofilms ($L_B < \delta$). The approximation of zero order reaction gives a simple analytical model with reasonable accuracy. With combination with first order reaction kinetics the accuracy can be improved further with weighted averaged approach (Kobayashi *et al.*, 1976).

2.3.4.3 Numerical solution of biofilm kinetics

In many cases biomass and biofilm is not homogeneous and not limited on a single substrate, in which case the biofilm kinetics has to be solved numerically. This involves solving the reaction-diffusion equation as follows

$$\frac{\partial S_i}{\partial t} = D_i \nabla^2 S + r_i \quad (2.10)$$

This can be solved numerically by Crank-Nicholson discretization (Anderson, 1995). A more complicate situation appears if mass transfer also proceed by advection. This add the consideration of the velocity \mathbf{u} in the advection-diffusion-reaction equation as follows

$$\frac{\partial S_i}{\partial t} = -\mathbf{u} \cdot \nabla S_i + D_i \nabla^2 S_i + r_i \quad (2.11)$$

This requires the distribution of \mathbf{u} to be known, which can be obtained by means of Computational Fluid Dynamics (CFD) which will be presented in section 2.6.

2.3.5 Modelling biofilm particulate components and thickness

There are various models to calculate the production and movement of particulate components in the biofilm. The methods can be of Eulerian type which means that changes of variables are monitored on fixed points in space or they can be of Lagrangian type which means that changes of variables are monitored by following movement of a mass property, for instance the biomass. The methods presented here are: Continuum models in 1 dimension, Cellular Automata (CA) and Individual-based Modelling (IbM).

2.3.5.1 Continuum models in 1 dimension

The continuum based models of biofilms are Eulerian type, where the mass balance of particulate components within the biofilm is given by

$$\frac{dX_{i,F}}{dt} = r_{i,F} - u_{X,F} \frac{dX_{i,F}}{dz} \quad (2.12)$$

where $u_{X,F}$ is the local advection velocity of particulate components in the biofilm normal to the substratum. Biofilm thickness can be solved dynamically by a balance of the surface growth velocity $u_{X,LF}$ and the detachment erosion velocity u_{det} as follows

$$\frac{d\delta_F}{dt} = u_{X,LF} - u_{det} \quad (2.13)$$

2.3.5.2 Cellular Automata biofilm models

CA biofilm models are also of Eulerian type and, as shown in Figure 2.7, they consist of a grid network of small mixed compartments where the biomass components are calculated as a state variable in each grid point. In the first generations of CA models, diffusion of substrate was simulated as random walker inserted at the liquid boundary. If the random walker has entered a grid point with biomass it may be consumed by a calculated probability based on kinetics, biomass and stoichiometry. When the total biomass in a grid point exceeds a critical concentration a fraction of this biomass is redistributed to a random neighbouring grid point. The set of rules of biomass spreading may vary depending on the CA algorithm used (Picioreanu *et al.*, 1998).

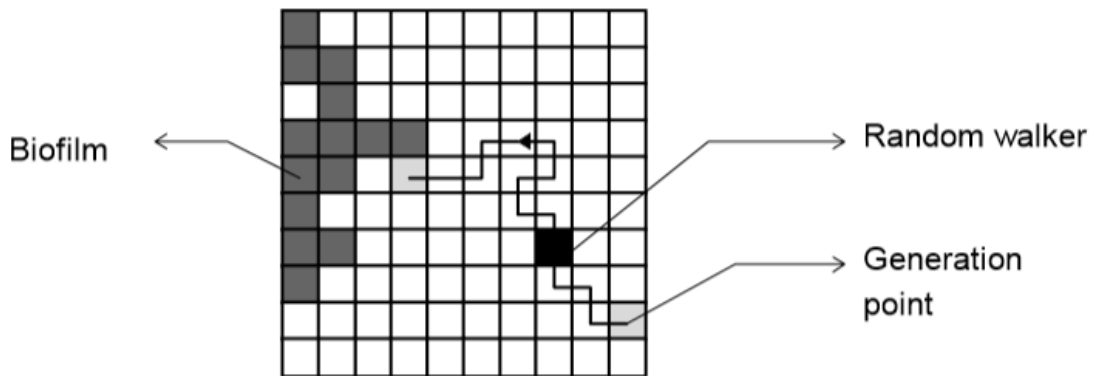


Figure 2.7. CA biofilm model with random walking substrate diffusion (Picioreanu, 1996)

2.3.5.3 Individual-based Modelling of biofilm

IbM are Lagrangian type of models and, as shown in Figure 2.8, they treat the individual organisms in the biofilms as spherical particles (Kreft *et al.*, 2001). Only one type of active biomass species is allowed in each particle, however each particle consists of a mixture of secondary biomass such as undegradable organics and EPS. Upon growth the mass of each particle is calculated by sets kinetic rate expressions for growth as follows

$$\frac{dm_{i,p}}{dt} = r_{i,p} \quad (2.14)$$

where $r_{i,p}$ is the mass specific reaction rate. The radii R_p of particles can be calculated by the following formula

$$R_p = \left(\frac{1}{4\pi} \sum_{i=1}^n \frac{m_{i,p}}{\rho_i} \right)^{\frac{1}{2}} \text{ in 2d} \quad R_p = \left(\frac{3}{4\pi} \sum_{i=1}^n \frac{m_{i,p}}{\rho_i} \right)^{\frac{1}{3}} \text{ in 3d} \quad (2.15)$$

When R_p in a particle reaches a critical value, division occurs where release of a daughter particle is simulated by adding a nearby particle that touches the mother cell. The mass in the mother cell loses 45-55% of its mass to its daughter cell. During cell expansions and divisions overlap of particles will occur unless an algorithm to distribute the cells is implemented. Firstly, for each particle, the distance, d , to the closest neighbouring particles needs to be obtained. In order to do this, the selection of N closest particles is obtained by the utilization of a nearest neighbour algorithm (Clarkson, 1983). This enables the calculation of the overlap radius with a neighbouring particle of radius R_n , (Kreft *et al.*, 2001)

$$R_{ov,p,n} = \max\left(\frac{k_{shov}(R_p + R_n) - d}{2}, 0 \right) \quad (2.16)$$

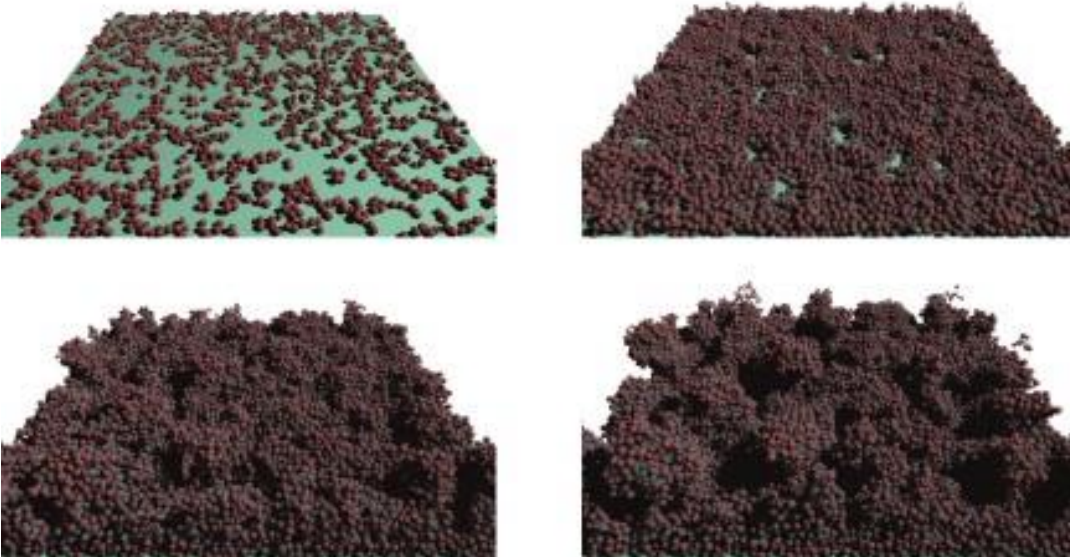


Figure 2.8. IBM simulations of biofilm growth (Xavier *et al.*, 2005a)

where k_{shov} is the shoving radius which control the water contents in the biofilm. The neighbouring particles will push each other and the position vector for current particle \mathbf{x}_p will change each iteration, m , until equilibrium state is reached

$$\mathbf{x}_p^{(m+1)} = \mathbf{x}_p^m - \sum_{n=1}^N R_{ov,p,n} \mathbf{n}_{p,n} \quad (2.17)$$

where $\mathbf{n}_{p,n}$ is the normal vector pointing from current to a neighbouring particle. In comparison to CA biofilm models, IbM gives more realistic biofilm morphology and clustering of individual cells. It also gives the freedom to implement cell-to-cell interactions such as the effect of cohesion (Kreft and Wimpenny, 2001).

2.4 Biofilm in porous media

2.4.1 Characteristics of biofilm in porous media

Porous media is a material that contains pores filled with air or water and are commonly composed of sand, soil or reticulated foam. The internal structure matrix usually has a very high surface area for attachment and growth of biofilm. Biofilm growth in porous media is of interest in a range of various fields such as water and wastewater treatment (Lazarova and Manem, 2000), natural biodegradation of organic contaminants in soils and aquifers (McCarty and Reinhard, 1981) and microbial enhanced oil recovery (Tanner *et al.*, 1991). Formation of biofilm in porous media have a large impact on permeability and the resulting mass transfer of soluble components (Cunningham *et al.*, 1991). The morphology of biofilms grown in porous media may differ substantially from uniform biofilm distribution to discontinuously formed biofilm colonies, which can be seen in Figure 2.9. Morphology depends on a range of different factors such as species of organisms, the structure of the porous medium, nutrient availability and hydrodynamic conditions (Rittmann, 1993).

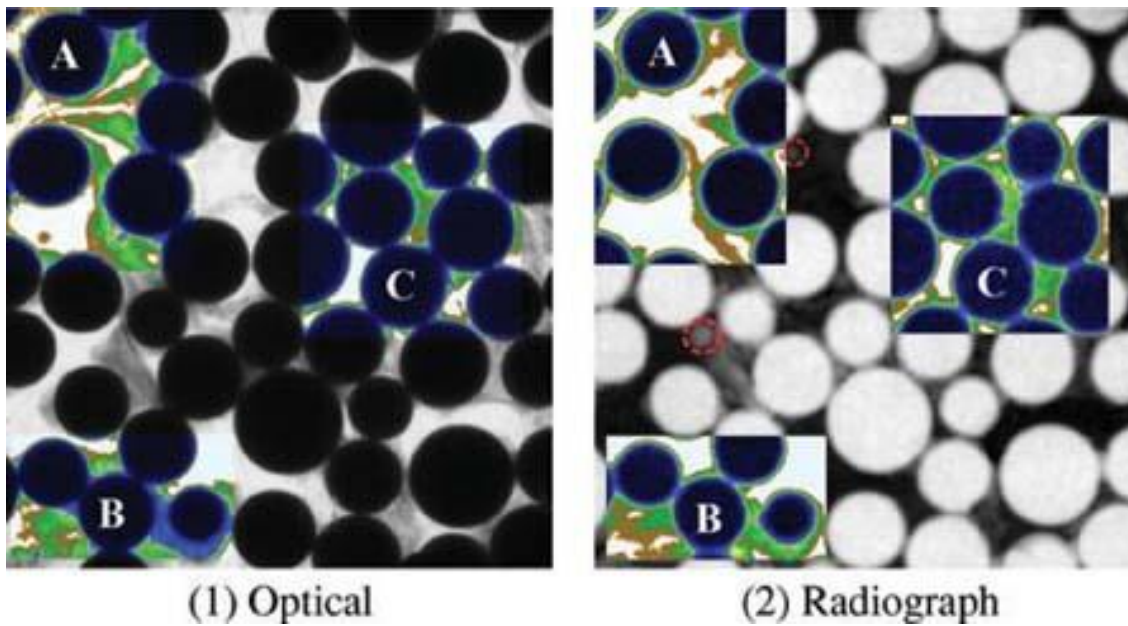


Figure 2.9. Imaging of biofilm in porous media using (1) optical visualization and (2) X-ray absorption radiography (Davit *et al.*, 2011).

From experiments, Paulsen *et al.*, (1997) could distinguish three different stages of biofilm growth. (i) Initially, biofilm grew homogeneously followed by (ii) development of surface heterogeneities and finally (iii) formations of biofilm strands spanning the pores and creation of water channels. Vayenas *et al.* (2002) observed in visualization experiments that biofilm thickness substantially decreased with the distance from the inlet and that a reduction in pore diameter resulted in thinner biofilms. Vandevivere (1995) showed in experiments that bio-clogging was more pronounced in fine grain system than coarse grain systems.

2.4.2 Modelling bio-clogging in porous media

Different groups of models of biofilm in porous media can be found in literature: (i) macroscopic scale models, (ii) microscopic scale models and (iii) hybrid models.

Macroscopic scale models are applicable if changes in the microscopic scales give negligible responses in the overall system behaviour (Clement *et al.*, 1996). The dynamics of these models are based on bulk change of parameters such as: porosity, specific surface area and permeability. Okubo and Matsumoto (1983) modelled the effect of presence of biofilm on the reduction of permeability by assuming the pore space to be consisting of a bundle of straight pores with uniform biomass, as follows

$$k_{rel} = \varepsilon_{rel}^2 \quad (2.18)$$

where k_{rel} and ε_{rel} are the relative permeability and porosity respectively, in comparison to porous media without biomass. Clement *et al.* (1996) found a similar relation but with a modified power factor of 16/9. These models are computationally efficient however the accuracy of predicting bio-clogging is poor if biomass is not grown homogeneously inside the porous media.

Microscopic scale models focuses on how the interaction of biofilm in pore scale affects the global properties of the system such as permeability. They can predict localized clogging in pores but become computationally demanding for large systems consisting of a large number of pores. A way to overcome this problem was to apply pore network modelling which makes it possible to model the effect of microbial growth on permeability in an artificial pore network without calculating every single pore (Thullner *et al.*, 2002). The following relation for bio-clogging of pore-networks was used:

$$k_{rel} = a \left(\frac{\varepsilon_{rel} - \varepsilon_{crit}}{1 - \varepsilon_{crit}} \right)^3 + (1 - a) \left(\frac{\varepsilon_{rel} - \varepsilon_{crit}}{1 - \varepsilon_{crit}} \right)^2 \quad (2.19)$$

where A and ε_{crit} was a fitting parameters.

Experimental evidence of a permeable biofilm (Stoodley *et al.*, 1994), motivated the study of multiscale modelling of biofilm in porous media. Figure 2.10 illustrates multiscale modelling performed by Kapellos *et al.* (2007a) who used a CA approach with conjunction with Lattice Boltzmann hydraulic solver. Implementation of biofilm permeability was done by addition of a Brinkmann effective viscosity term into the Navier Stokes equation. Biofilms in porous media applied for soils has also been coupled with IBM approach (Pintelon *et al.*, 2009). By addition of decay and lysis processes, preferential flow paths inside the porous media can be accurately modelled (Bottero *et al.*, 2013)

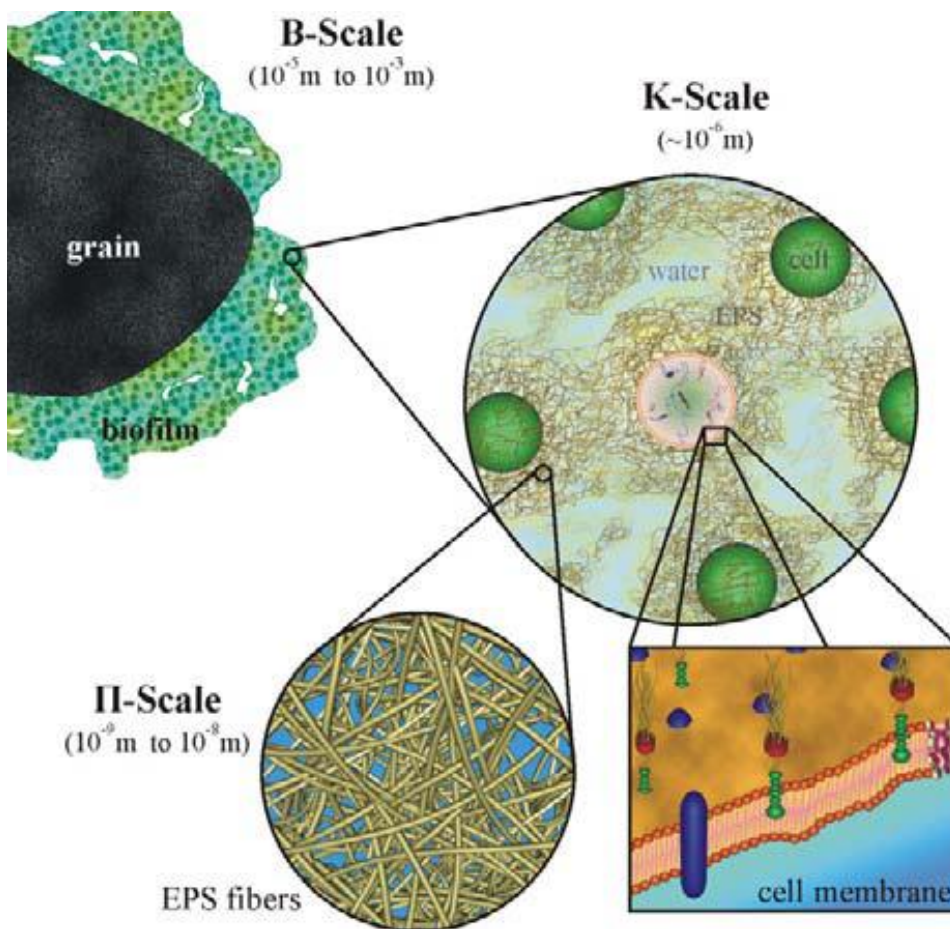


Figure 2.10. Multiscale modelling of biofilm in porous media. Adapted from Kapellos *et al.* (2007a)

2.5 Biofilm in sponge carrier media

A sponge carrier media with a diameter of 12 mm and sampled from a reactor in Gifu, Japan is shown in Figure 2.11. A magnification of biomass on the sponge skeleton, illuminated by fluorescent in situ hybridization (FISH) (Chae *et al.*, 2008) is shown in Figure 2.12. It clearly shows that the biomass inside the sponge carrier media grows as a biofilm. Because of the porosities of the sponge carrier media, the biofilms behave differently from ordinary moving bed carrier media. Kinetic test have revealed that the biofilm reaction of a fluidized sponge is affected by the internal porous media flow inside (Matsui and Deguchi, 2002). Biofilm in sponge

carrier media has very similar features to biofilm in porous media. As with soils, clogging of biofilm in sponge carrier media is an issue and they have to be jostled frequently with coarse air diffuser to detach excess biomass (Morper and Linde, 2005). Distribution of biofilm thickness is very similar to that of sand columns, with a thick biofilm layer near the surface and a thin biofilms at inner parts (Chae *et al.*, 2012).



Figure 2.11. Photo of a sponge carrier media obtained from Seki wastewater treatment plant, Gifu prefecture, Japan.

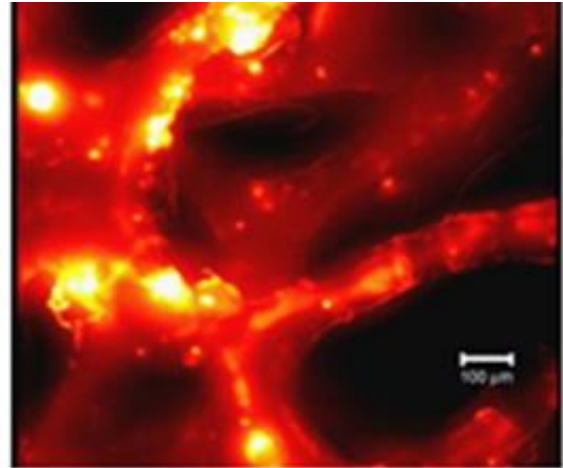


Figure 2.12. Biofilm inside sponge carrier media illuminated by FISH (Chae *et al.*, 2008).

2.6 Particle methods for computational fluid dynamics

Computational Fluid Dynamics (CFD) is a branch in fluid mechanics that uses various numerical methods to solve for motions of fluids. A general description is given here followed by different CFD methods applied for the research in this dissertation.

2.6.1 Computational Fluid Dynamics

CFD are applied to numerically solve the distribution of velocity \mathbf{v} and pressure p in the Navier-Stokes equations and the continuum equations. For an incompressible and Newtonian fluid, they are given respectively as follows (Anderson, 1995)

$$\frac{\partial \mathbf{u}}{\partial t} + \mathbf{u} \cdot \nabla \mathbf{u} = -\frac{\nabla p}{\rho} + \nu \nabla^2 \mathbf{u} + \frac{\mathbf{f}}{\rho} \quad (2.20)$$

$$\nabla \cdot \mathbf{u} = 0 \quad (2.21)$$

where ν is the kinematic viscosity and \mathbf{f} is the body force per unit volume. Solving CFD usually include these steps:

1. Defining of the geometry and the physical bounds
2. Division of the fluid geometry into discrete cells that resemble the mesh
3. Implement physical models such as equations of motion
4. Define boundary conditions to describe fluid behavior at inlets, outlets and walls
5. Start the simulation to iteratively solve the solution as steady state or in transient mode
6. Analyse of the results in a postprocessor

2.6.2 Modelling multiphase flow with particles and droplets

2.6.2.1 Particle drag equation and the drag coefficient

The drag force of a particle moving with a relative velocity to the surrounding fluid is quantified by the drag coefficient C_D through the equation

$$\mathbf{F}_D = \frac{1}{2} \rho_f C_D A |\mathbf{u}_f - \mathbf{u}_p| (\mathbf{u}_f - \mathbf{u}_p) \quad (2.22)$$

where ρ_f is the density of the fluid, A is a representative area facing the flow and \mathbf{u}_f and \mathbf{u}_p are the velocities of the fluid and particle respectively. C_D depends on the volume fraction of particles in the liquid and the particle Reynolds number defined by

$$Re_p = \frac{\rho_f d |u_f - u_p|}{\mu_f} \quad (2.23)$$

For single spherical particles, and $Re_p < 1000$, C_D can be obtained by Schiller-Neumann correlation as follows (Crowe *et al.*, 1997)

$$C_{D,Schiller-Neumann} = \frac{24}{\text{Re}_p} (1 + 0.15 \text{Re}_p^{0.687}). \quad (2.24)$$

The effect of the particle volume fraction on the drag coefficient will be explained in section 2.6.2.4.

2.6.2.2 Characterization of fluid-particle flow

The particle response time is important parameter for the characterization of the fluid-particle flow. In the absence of external forces, the equation of motion of a spherical particle is given by

$$m \frac{d\mathbf{u}_p}{dt} = \frac{1}{2} \rho_f C_D A |\mathbf{u}_f - \mathbf{u}_p| (\mathbf{u}_f - \mathbf{u}_p) \quad (2.25)$$

where m is the particle mass. By dividing equation (2.25) by the particle mass yields

$$\frac{du_p}{dt} = \frac{3C_D \rho_f}{4\rho_p d} |u_f - u_p| (u_f - u_p) \quad (2.26)$$

The inverse of the expression in front of $(u_f - u_p)$ on right hand side of equation (2.26) is the response time of a particle:

$$t_{res} = \frac{4\rho_p d}{3C_D \rho_f |u_f - u_p|} \quad (2.27)$$

A common simplification of equation (2.27) is to use the Stoke flow approximation, however this will not be accurate as the particle Reynolds number is much higher than unity. The response time can be used to estimate the degree of how particles follow fluid flow by the Stokes number which is the ratio of the response time to the characteristic time of the fluid as follows

$$St = \frac{t_{res} U_{char}}{L_{char}} \quad (2.28)$$

where U_{char} and L_{char} are the characteristic velocity and length scale of the fluid flow. If St is low, particles follow the fluid flow and if St is high particles deviates from the fluid flow.

Another important parameter, is the collision time which is the average time between particle collisions given by (Crowe *et al.*, 1997)

$$t_{col} = \frac{3d}{18\alpha_f |u_f - u_p|} \quad (2.29)$$

The particle-fluid flow can be dilute or dense which depends on the ratio between the particle response time and the particle collision time which may be given as follows (Crowe *et al.*, 1997)

$$\frac{t_{res}}{t_{col}} = \frac{8\alpha\rho_p}{C_D\rho_f} \quad (2.30)$$

For sponge reactors in water liquid, where the particle phase density is nearly equal to the fluid phase density, we may estimate the threshold α for dense flow to 0.125 by inputting $C_D \approx 1$ and $\rho_p \approx \rho_f$. The characterization of dilute and dense flow is important for the selection of models to be used.

2.6.2.3 Density driven multiphase flow

The pressure force per unit volume produced by buoyancy forces can be obtained by Archimedes principle

$$\nabla p = (\rho_p - \rho_f)\mathbf{g} \quad (2.31)$$

where \mathbf{g} is the gravitational vector pointing towards direction of the gravitational force (negative vertical direction). By inserting equation (2.31) into equation (2.25) the following relation is obtained:

$$\frac{d\mathbf{u}_p}{dt} = \frac{3C_D\rho_f}{4\rho_p d} |\mathbf{u}_f - \mathbf{u}_p| (\mathbf{u}_f - \mathbf{u}_p) + \left(\frac{\rho_p - \rho_f}{\rho_p} \right) \mathbf{g}. \quad (2.32)$$

2.6.2.4 Modelling Particle Clouds

Ergun (1952) found that the pressure drop through a packed bed was given as follows

$$\frac{\Delta p}{\Delta L} = 150 \frac{\alpha_p^2 \mu_f U_{sf}}{\alpha_f^3 d_p^2} + 1.75 \frac{\alpha_p \rho_f U_{sf}^2}{\alpha_f^3 d_p} \quad (2.33)$$

where $U_{sf} = \alpha_f u$ is the superficial velocity through the bed. By rewriting equation (2.23) in terms of a slip velocity, $|\mathbf{u}_f - \mathbf{u}_p|$, the following relation yields:

$$\nabla p = 150 \frac{\alpha_p^2 \mu_f (\mathbf{u}_f - \mathbf{u}_p)}{\alpha_f^2 d_p^2} + 1.75 \frac{\alpha_p \rho_f |\mathbf{u}_f - \mathbf{u}_p| (\mathbf{u}_f - \mathbf{u}_p)}{\alpha_p d_p} \quad (2.34)$$

from which, the interfacial momentum transfer coefficient from can be defined by

$$\beta_{Ergun} = 150 \frac{\alpha_p^2 \mu_f}{\alpha_f^2 d_p^2} + 1.75 \frac{\alpha_p \rho_f |\mathbf{u}_f - \mathbf{u}_p|}{\alpha_p d_p} \quad (2.35)$$

and the drag coefficient can be obtained as follows

$$C_{D,Ergun} = \frac{4\beta_{Ergun} d_p}{3\rho_f |\mathbf{u}_f - \mathbf{u}_p|} \quad (2.36)$$

Wen and Yu (1966) suggested the following modification to the Schiller-Neumann correlation in equation (2.23) when the solid fraction is high (Wen and Yu, 1966)

$$C_{D,Wen-Yu} = C_{D,Schiller-Neumann} \alpha_f^{-2.65} \quad (2.37)$$

Gidaspov suggested that Ergun correlation should be used in high solid fractions $\alpha_p > 0.2$, whereas Wen and Yu correlation should be used in low solid fractions $\alpha_p < 0.2$ (Gidaspow, 1994). RFLOW solver assumes that C_D is the maximum value obtained from these two correlations as follows

$$C_D = \max(C_{D,Wen-Yu}, C_{D,Ergun}) \quad (2.38)$$

2.6.2.5 Eulerian-Eulerian and Eulerian-Lagrangian approaches

As with biomass in biofilm (see section 2.3.5), the methods of monitoring changes in properties in space can be of Eulerian type which means that changes of variables are monitored on fixed points in space or they can be of Lagrangian type which means that changes of variables are monitored by following movement of a mass property. The most common approaches of modelling fluid-particle multiphase flows are the Eulerian-Eulerian (EE) and Eulerian-Lagrangian (EL) approaches. In EE approaches, both phases are regarded as Eulerian and the solver solves for the volume fraction of the individual phases. In EL models, the fluid is Eulerian and the particle phase is Lagrangian. EE models are more computationally

efficient but they cannot deal with particle-particle interactions that are dominant in dense flows which justifies the use of Lagrangian approaches.

2.6.3 CFD-DEM

CFD-DEM is the coupling of CFD with Discrete Element Method (DEM) to simulate fluid and particle interactions and were initially applied for fluidized bed simulations (Tsuji *et al.*, 1993). DEM is Lagrangian and solve for the Newton's law of motion on every single particle while the flow of the continuum gas or liquid is Eulerian and calculated by the local averaged Navier Stokes equations. Apart from drag force \mathbf{F}_D and gravity forces \mathbf{F}_G discussed in section 2.6.2, DEM calculates contact forces \mathbf{F}_C and friction forces \mathbf{F}_F during particle-particle and particle-wall collisions. \mathbf{F}_C can be obtained by sum of the spring forces of neighbouring particles as follows

$$\mathbf{F}_C = -k \sum_{i=1}^N R_{ov,i} \mathbf{n}_i \quad (2.39)$$

where k is the spring constant, $R_{ov,i}$ is the overlap radius of particle i and \mathbf{n} is the normal vector pointing at particle i . In DEM it is also possible to add attractive potential force \mathbf{F}_A which can solve for cohesion and adhesion for viscoelastic materials such as polymers. Each particle will respond to the total force \mathbf{F}_T on each particle which is the sum of all forces as follows

$$m \frac{d\mathbf{u}_p}{dt} = \mathbf{F}_T = \mathbf{F}_D + \mathbf{F}_G + \mathbf{F}_C + \mathbf{F}_F + \mathbf{F}_A. \quad (2.40)$$

2.6.4 Lattice Boltzmann method

Lattice Boltzmann method models the fluid as consisting of fictive particles. These particle interacts with each other by series of collision and streaming steps. The lattice is divided into a number discrete directions which represent the directions of possible collisions. The particle-like structure and local interactions make LBM method ideal for situation with complex boundaries such as flow porous media (Succi, 2013).

2.7 Summary of available and missing knowledge

This literature review, presented up to date research on biofilm and biofilm in porous media and the present methods of how these complex systems can be modelled. From what is known about biofilm in porous media, the following similarities between sponge carrier media and biofilm in soils has been observed.

- By FISH analysis it has been shown that the biomass inside the sponge carrier media grow as a biofilm on the internal porous matrix (Chae *et al.*, 2008).
- From kinetic tests of sponge carrier media in different hydraulic conditions, the reaction kinetics is similar to that of biofilm in porous media (Matsui and Deguchi, 2002).
- Biofilm tends to clog the internal voids which significantly could reduce reaction performance (Morper and Linde, 2005)

There is missing knowledge both in terms on of how biofilm in sponge carrier media behave and the methodology to simulate mass transfer in sponge carrier media. From the literature review, the following gaps in current knowledge was realized

- How is the degree of bio-clogging in sponge carrier media? How can bio-clogging be modelled?
- How does biofilm in sponge carrier media develop with time? Are there similarities with Paulsen *et al.* (1997) as an initial homogeneous biofilm followed by a clogging heterogeneous biofilm formation?
- What are the effects of carrier collisions on detachment? Does this form a significantly different biofilm than that found in sand columns?
- The sponge carrier media consist of a hierarchical of scales of porous media systems: sponge scales, pore scale and the biofilm. How can this multiscale system be modelled properly?

Based on the missing knowledge, a modelling study will be conducted in order to deepen the understanding of mass transfer and bio-clogging. In order to do this, interfaces has to be constructed to create relevant boundary value implementations.

- Sponge-reactor scale: An interface that models the effect of reactor dynamics on the internal pore hydraulics and reaction needs to be constructed. This is handled in chapter 3.
- Organism-biofilm scale: A model that generates local biofilm morphology based on individual growth and detachment of biofilm needs to be constructed. This is investigated in chapter 4.
- Biofilm-pore scale: A model needs to be constructed that investigates the effect of the biofilm on the pore clogging inside the sponge carrier media and how it affects the reaction rate. This is handled in chapter 5 and has been divided into two parts:
 - Model the biofilm growth based on reaction-advection diffusion equation inside the sponge carrier media
 - Solve for the biofilm detachment caused by abrasion due to carrier collisions.
- The final step in chapter 6 involves the integration of the models to a simplified model that contain the relevant inputs that are enough to describe mass transfer processes as whole without being too complex. In this way it can be utilized for the engineers for the modelling of mass transfer and bio-clogging in sponge carrier media.

3 MODEL DEVELOPMENT OF A SPONGE CARRIER PROCESS USING CFD-DEM WITH PERMEABLE PARTICLES

3.1 Introduction

This study explains the modelling of sponge carrier media in two steps. Firstly, simulations using Computational Fluid Dynamics coupled with Discrete Element Methods (CFD-DEM) were performed to model fluidized sponges in a reactor. The sponge slip movement in the reactor was used to calculate intraparticle forced convection and biofilm reaction by integrating models of porous catalytic pellets. In comparison to the original article which this chapter is based on (So *et al.*, 2012), it contains additional results and discussion in sections 3.3.3-3.4 about the multiphase flow dynamics and recommendation of future work.

A proper control of the oxygen transfer rate in MBBR (Moving Bed Biofilm Reactors) can prevent internal oxygen depletion and thus improving the reaction rate. Sponge carriers that are applied to activated sludge were used in this study. At present, there is limited technical information on how the sponge diameters or aeration systems can be optimized for given operating conditions.

An explanation to its efficiency is the high specific surface area at which the biomass can attach as biofilm (Chae *et al.*, 2008, Lin, 2010). However, limitations may be present for the mass transfer to the biofilm through the pore network which leads to oxygen depletion at a few millimetres depth (Morper and Linde, 2005, Nguyen *et al.*, 2010). The mass transfer limitation is also of importance for the choice of sponge size, and for a study by Guo *et al.* (2010), it was found that when the sponges diameters increased above 10 mm, nitrogen and organic removal decreased due to internal oxygen depletion.

The depth of oxygen depletion in order of millimetres is much higher than the penetration depth of a few hundred micrometres obtained considering only bacteria reaction and molecular diffusion as in biofilms. It suggests that convection along with diffusion inside sponges govern sponge biofilm reaction. This was clarified further by Matsui and Deguchi (2002), who conducted kinetic tests of cubic sponges. They found that the biological reaction rate was governed by flow of water inside the pores and it was dependent on hydraulic conditions outside the sponges. This may be referred to intraparticle forced convection and it has been an active research field for porous catalytic pellets (Rodrigues *et al.*, 1982). It was found that inside pellets of large pores (>100 μm), convection was dominating over diffusion and slip velocity of the fluidized pellets could augment the internal reaction rate.

In commercialized sponge carrier processes such as LINPOR™, the spiral roll aerator configuration is preferred over total floor coverage aeration. This is to avoid sponges accumulating on the surface as indicated by Morper and Linde (2005). However, for conventional activated sludge, total floor coverage aeration has shown higher bubble oxygen transfer because bubbles were retained longer due to disruption of the spiral flow pattern (Fujie *et al.*, 1997). At present, there is no study that has examined the effect of aerator configuration on intraparticle forced convection.

Based on the above, the purpose of this study was to model the internal reaction rate of sponge moving bed carriers and investigate to what extent the reaction depends on hydraulic conditions of the reactor. Using CFD-DEM, the slip velocity of

individual moving sponges can be obtained and used to calculate the internal velocity. To evaluate the impact of sponge size on mass transfer limitation for the reaction rate, different sponge diameters were used in this study.

3.2 Methods

3.2.1 Model concept

Figure 3.1 describes the different phenomena that make the sponges slip against surrounding liquid: settling/rising (a), particle collisions (b) and slow response time of the sponge (c), (Crowe *et al.* 1998). If there is a slip velocity, pressure drop along the particle is created, resulting in internal flow in the pores of the sponges which is illustrated in Figure 3.2.

According to Rittman (1993), biofilm in porous media can be assumed to be homogeneously distributed along a surface for the range of nutrient loadings occurring in waste water treatment. Based on this, sponges in a virtual reactor were modelled as having non-growing 100 μm biofilm of nitrifying bacteria distributed along the walls of the sponge skeleton. The biofilm thickness is similar to the ones obtained for sponge MBBR by Chae *et al.* (2008) and Lin (2010); 50-150 μm and 75 μm respectively. A nitrifying biofilm requires oxygen to be transported through the porous network before it can be transported through the biofilm by molecular diffusion (Rittmann, 1993). Therefore, the internal velocity, illustrated in Figure 3.2, is an important limiting factor for reaction because of the large specific surface area of biofilm and the small pore sizes. According to Darcy's law, a velocity in porous media can be created by a pressure drop (Nabovati *et al.*, 2009). This can be achieved in sponge cubes if they move at a different velocity to the surrounding liquid (Rodrigues *et al.*, 1982). This is the actual case because large particles, such as sponges, cannot exactly follow fluid motion but move with a slip velocity due to slow response to outside forces such as buoyancy and fluid acceleration (Crowe *et al.*, 1997).

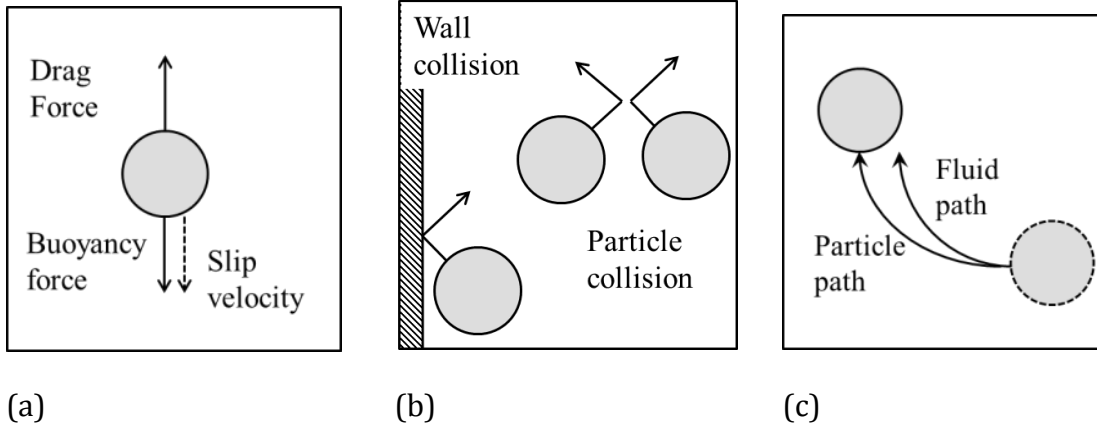


Figure 3.1. Slip velocity is affected by buoyancy forces (a), collision with walls and other particles (b) and sponge fluid response time (c)

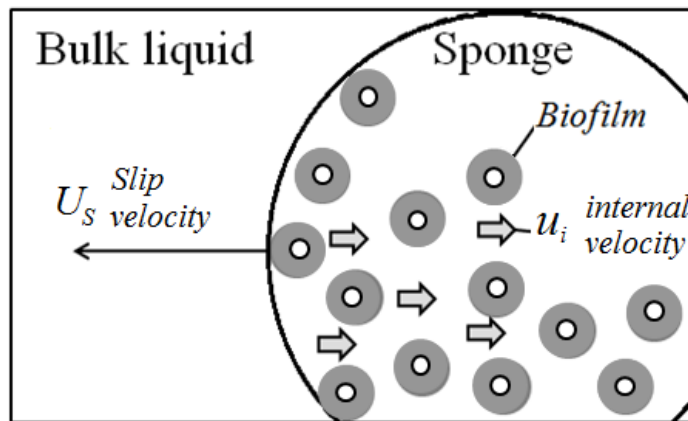


Figure 3.2. The biofilm distribution observed in a moving sponge

3.2.2 Modelling sponge nitrification

Oxygen was assumed to be the rate limiting substrate and the oxygen utilization rate (OUR) was governed by the Monod rate expression (Wanner *et al.*, 2006). Combined with Fick's law of diffusion (Levenspiel, 1962) the localised change of oxygen with time was modelled by equation (3.1):

$$\frac{\partial S_{O_2}}{\partial t} = D_{O_2} \nabla^2 S_{O_2} - q_{max} \left(\frac{S_{O_2}}{S_{O_2} + K_{O_2}} \right) X_A \quad (3.1)$$

3.2.2.1 Biofilm reaction curve

Equation (3.1) was solved numerically using Crank Nicholson discretization scheme (Anderson, 1995) for a biofilm thickness $l_b = 100 \mu\text{m}$, autotroph biomass concentration of $X_A = 10 \text{ kg/m}^3$ and affinity constant $K_{O_2} = 0.4 \text{ g/m}^3$. As a preliminary result, the flux of oxygen into the biofilm was obtained as in Figure 3.3. By applying a best fit curve of the oxygen flux, J_b , an apparent affinity coefficient $K_{O_2,app} = 1.4 \text{ g/m}^3$ for the biofilm oxygen flux could be obtained, as shown in equation (3.2).

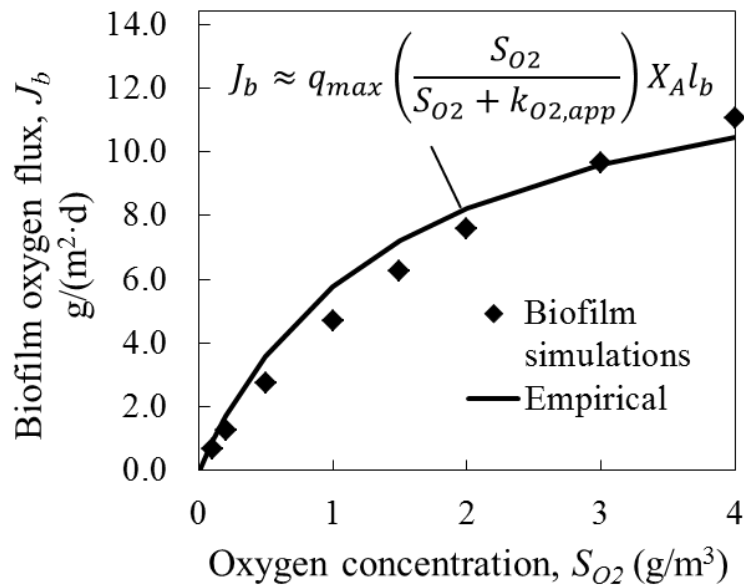


Figure 3.3. Flux of oxygen into biofilm ($X_A = 10 \text{ kg/m}^3$ and $l_b = 100 \mu\text{m}$) plotted with pore oxygen concentration.

$$J_b \approx q_{max} \left(\frac{S_{O_2}}{S_{O_2} + K_{O_2,app}} \right) X_A l_b \quad (3.2)$$

3.2.2.2 Sponge mass transfer

By having the apparent affinity coefficient of the biofilm oxygen flux, the sponge pore reaction and mass transfer in spherical sponges could be obtained. Convection inside sponges was modeled with an apparent diffusivity, D_{app} (m²/s) (Rodrigues *et al.*, 1982) shown as a function of internal velocity, u_i , sponge diameter, d , and Peclet number, λ , as in equations (3.3-3.4):

$$D_{app} = \frac{u_i d}{6} \left(\frac{1}{\tanh \lambda} - \frac{1}{\lambda} \right)^{-1} \quad (3.3)$$

$$\lambda = \frac{u_i d}{2} \frac{\tau}{D_{O_2} \Phi \kappa} \quad (3.4)$$

With the given modifications and assumption of spherical sponges, equation (3.1) was modified into equation (3.5) for the internal oxygen transfer and reaction:

$$\frac{\partial S_{O_2}}{\partial t} = \frac{D_{app}}{r^2} \frac{\partial}{\partial r} \left(r^2 \frac{\partial S_{O_2}}{\partial r} \right) - J_b a_b \quad (3.5)$$

where the last term, $J_b a_b$, is the overall Oxygen Utilization Rate (OUR), obtained by multiplying the biofilm oxygen flux by the specific surface of the biofilm a_b . Thus, the overall OUR is dependent on sponge diameter d , biofilm area a_b , porosity Φ and the internal velocity, u_i .

3.2.3 Sponge hydrodynamics

The magnitude of the internal velocity, u_i , can be calculated by Darcy's law (Nabovati *et al.*, 2009) as shown in equation (3.6):

$$u_i = \frac{k}{\mu} |\nabla p| \quad (3.6)$$

The sponges were spherical with diameters 5, 10 and 20 mm, with S30R foam (30 pores per inch) and void 97%. They correspond to commercialized sponges such as LINPOR™ except for the cuboid shape (15 x 12 x 12 mm) (Morper and Linde, 2005). By using a geometric model of the foam network (Duan *et al.*, 2006), the reduced porosity with biofilm $\Phi = 60\%$ and specific surface area, $a_b = 4200 \text{ m}^2/\text{m}^3$, were obtained for attached biofilm of 100 μm . The permeability, $k = 7 \cdot 10^{-9} \text{ m}^2$ was calculated from a relation by Nabovati *et al.* (2009) for fibrous porous media with a fibre thickness of 260 μm . For a cloud of sponges moving with slip velocity, U_s , the magnitude of the pressure gradient, $|\nabla p|$, can be obtained by Ergun law (Rodrigues *et al.*, 1982) as in equation (3.7):

$$|\nabla p| = \frac{150\mu(1 - \alpha_l)^2 U_s}{\alpha_l^2 d^2} + \frac{1.75(1 - \alpha_l)\rho_l U_s^2}{\alpha_l d} \quad (3.7)$$

Equation (3.7) is accurate for dense flows with liquid fractions below 0.8. Thus, the slip velocity, U_s , is used as a model interface to connect reactor hydrodynamics to the internal velocity, u_i . The slip velocity of sponges, U_s , can be solved for a given reactor using a CFD-DEM.

3.2.4 Aeration tank model

3.2.4.1 Aeration tank and configurations

In the CFD-DEM solver, an identical tank to the one of Sekizawa *et al.* (1985) was used with dimensions $W = 6.85$ m and $H = 5$ m. As illustrated in Figure 3.3 three aeration systems were modelled: spiral roll, total floor coverage and dual spiral roll aeration. The average sponge volume fraction ($\bar{\alpha}_s = 30$ %) and wet density ($\rho_s = 1003$ kg/m³) were fixed and different aeration intensities (0.25, 0.5, 1, 2, 4 and 8 m³/m²h) were tested. The spiral roll type was also tested with different sponge diameters (5, 10 and 20 mm). The diffuser in the spiral roll configuration was

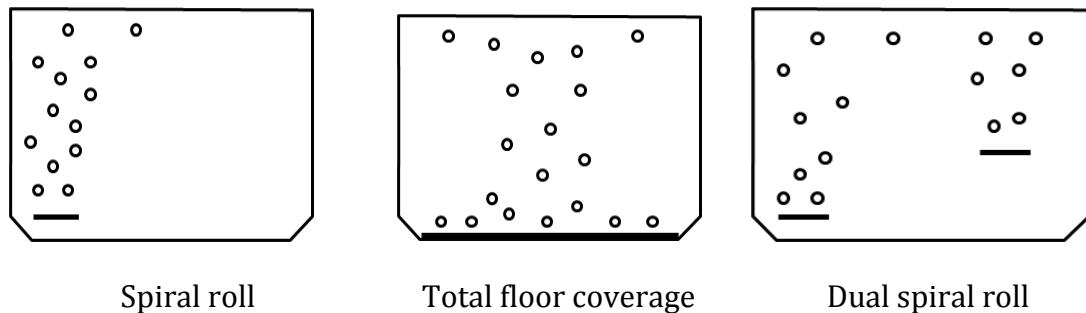


Figure 3.4. The different aerator configurations.

placed at $x = 0.5$ - 1.5 m, $y = 0.5$ m and the dual spiral roll configuration has the left diffuser placed identically and with an additional one placed at $4.85 < x < 5.85$ and $y = 1.5$. Regarding the dual spiral roll configuration, the relative strength to the total was 60 % and 40 % for the left and right aerator respectively.

3.2.4.2 CFD-DEM solver

CFD-DEM simulations using R-flow software (Rflow Co. Ltd., Japan) were performed. The flow velocity field was obtained by solving Navier Stokes equations for turbulent flow using k - ϵ model (Anderson, 1995). Sponges and air bubbles were modelled as individual moving and colliding particles using DEM (see section

Table 3.1 Parameters for the CFD-DEM simulation

Expression	Unit	Air bubbles	Sponges
Density	kg/m ³	1.4	1003
True particle diameter	m	0.003	0.005-0.02
DEM particle diameter	-	0.03	0.1
Restitution coefficient	-	0.7	0.7
Slide friction coefficient	-	0.5	0.5
Volume fraction	-	0-0.8 %	30 %
Number of particles		0-40,000	38,900

2.6.3). Gidaspov drag model, that includes Ergun law in equation (3.7), was used as a solver for the particle drag analysis (Gidaspow, 1994)(see section 2.6.2.4)The parameters of the CFD-DEM simulations are given in Table 3.1. In the DEM simulation the particle diameter was modelled as being larger than true size to reduce the number of particles and the computational time. However for the estimation of the drag in the CFD model, the true particle sizes were used. The results were checked for convergence of gas hold up and for a reference velocity point. In order to check particle number dependence, additional simulations were run with triple the amount of particles.

3.3 Results

3.3.1 Reactor hydrodynamics

The different aerator configurations resulted in three different flow patterns as shown in Figure 3.5, representing instantaneous fluid velocity for aeration intensity 4 m³/m²h. The highest ascending velocity was found in the spiral roll configuration in the bubble zone above the diffuser. The flow field for the total floor coverage aerator had a double spiral flow pattern and was unstable with time. For the dual spiral roll configuration, the low velocity region below the right aerator indicates a dead spot in the velocity field. Figure 3.6 shows the spatial distribution and the particle velocities of the sponges for the different aeration

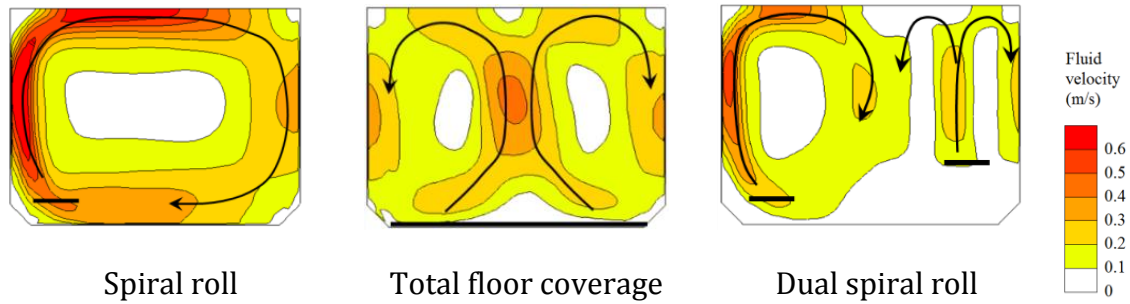


Figure 3.5. Fluid velocity for the different aerators for $d = 10$ mm and $Q_A = 4$ $\text{m}^3/\text{m}^2\text{h}$.

configuration for aeration intensity of $4 \text{ m}^3/\text{m}^2/\text{h}$. For the dual spiral roll configuration, some sponges below the right diffuser were settled out of circulation in contrast to other aeration configurations.

In order to analyse the aeration impact on the internal mass transfer of sponges, the lateral distribution of slip velocity for a random selection of 5000 sponges was plotted in Figure 3.7 for all different aeration configurations. As seen in the figures, regions of high slip velocity correspond to the bubbly zones above the aerators and the regions near the walls. The higher sponge slip velocity was caused by the delay of sponges to respond to the high acceleration occurring in this region (Crowe *et al.*, 1998). Outside these areas, the slip velocity was lower and dominated by sponge settling. This is shown by the median value to be closely corresponding to the terminal slip velocity of 9.2 mm/s , that was obtained by replacing the pressure gradient (∇p) in equation (3.7) by the average buoyancy force per unit volume acting on sponges ($\bar{\alpha}_s g(\rho_s - \rho_l)$). For the dual spiral roll configuration a group of sponges with very low velocity existed on the right side. This is due to the stagnant zone below the right diffuser, where the local velocity is too low to provide complete fluidization.

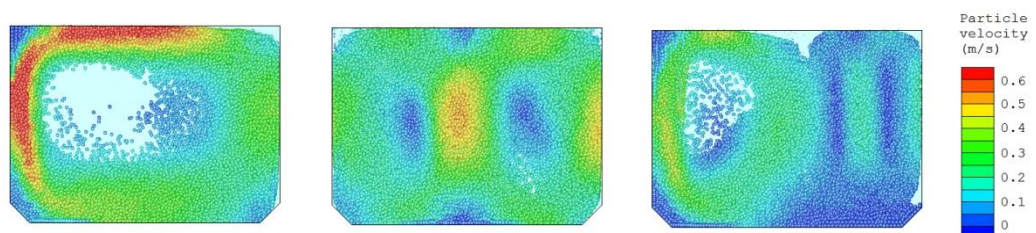


Figure 3.6. Particle spatial distribution and particle velocity for spiral roll, total floor coverage and dual spiral roll aeration configurations at $4 \text{ m}^3/\text{m}^2/\text{h}$.

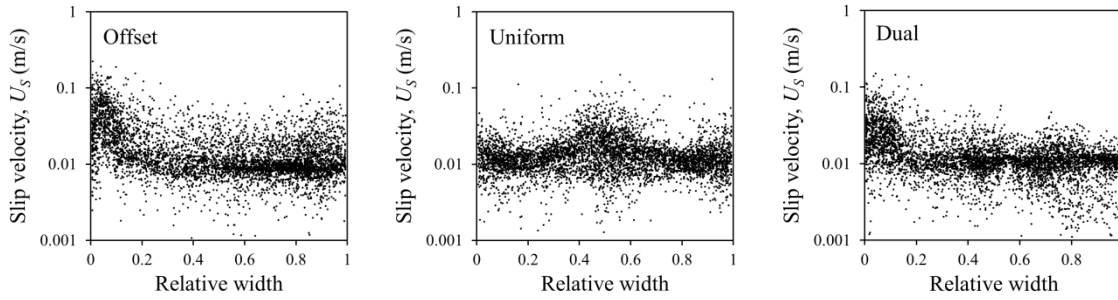


Figure 3.7. Distribution of sponge slip velocity, U_s , for $d = 10$ mm and $Q_A = 4$ $\text{m}^3/\text{m}^2\text{h}$.

3.3.2 Sponge effectiveness factor

From the diffusivity and reaction calculations of the sponges' interior, the concentration distribution could be obtained.

Figure 3.8 shows the local pore DO concentration inside sponges with different Damköhler numbers Da (-) which is the ratio of the potential biofilm utilization rate to the convection rate as shown in equation (3.8):

$$Da = \frac{J_{b,bulk} a_b}{S_{O_2}} \frac{d}{2u_i} \quad (3.8)$$

where $J_{b,bulk}$ is the oxygen flux of the biofilm in the case of no pore mass transfer limitation. From Figure 3.8 it is seen that the concentration of oxygen declines

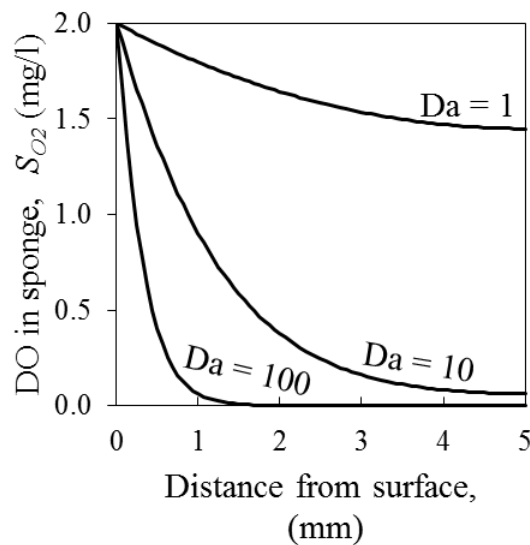


Figure 3.8. Concentration distribution inside sponges for $d = 10$ mm, $S_{O_2,bulk} = 2$ g/m^3 and $1 \leq Da \leq 100$.

with distance from the surface. By increasing the Damköhler number by decreasing the internal velocity, the concentration curve becomes lowered because of lower availability of oxygen for reaction and at $Da > 10$, oxygen depletion occurred in the centre. From the DO distribution, the overall biofilm flux, \bar{J}_b was obtained. The effectiveness factor, E , was calculated as the ratio of biofilm flux with pore diffusion limitation, \bar{J}_b , to the flux that would be present without pore diffusion limitation, $J_{b,bulk}$, as in equation (3.9)

$$E = \frac{\text{Average flux with pore diffusion}}{\text{Flux without pore diffusion}} = \frac{\bar{J}_b}{J_{b,bulk}}, \quad 0 \leq E \leq 1. \quad (3.9)$$

Results of effectiveness factor obtained from reaction and diffusion calculations are shown in Figure 3.9. The solid line is an empirical correlation, as given by equation (3.10)

$$E \approx \left(\frac{K_D}{K_D + Da} \right)^n \quad (3.10)$$

where $K_D = 6.8$ and $n = 1/2$ are empirical coefficients. The marker points have been calculated with different bulk oxygen concentrations (1, 2 and 4 g/m³), sponge diameters (5, 10 and 20 mm) and internal velocity range from 10⁻⁵ to 10⁻² m/s. If

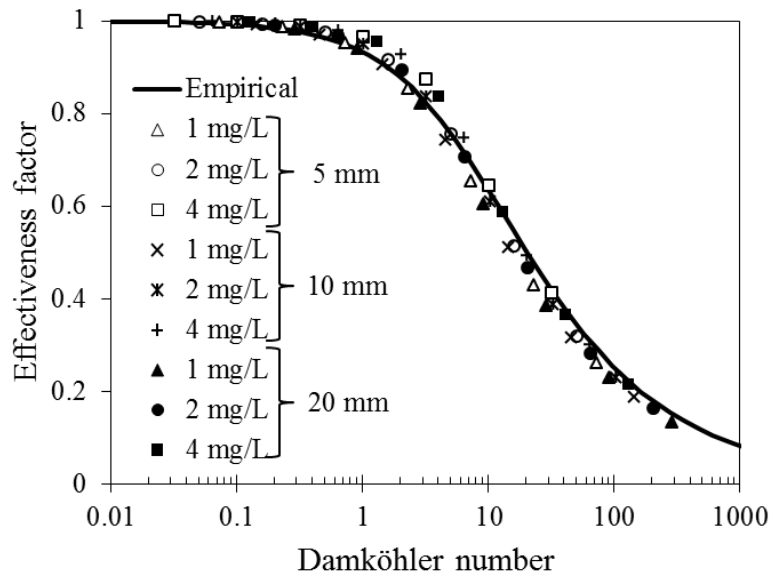


Figure 3.9. Numerical simulation data and correlation of the effectiveness factor plotted with Damköhler numbers.

the internal velocity is lower than 10^{-5} m/s, the correlation becomes inaccurate for 5 mm sponges, because molecular diffusion in pores becomes important. However, this occurs only if the corresponding slip velocities are less than 10^{-3} m/s, which did not occur under normal operating conditions ($1 \leq Q_A \leq 8$ m³/m²h).

To quantify the performance of the reactor, an overall effectiveness factor, \bar{E} , was defined by volume averaging the effectiveness factor in the mesh as in equation (3.11):

$$\bar{E} \approx \frac{1}{\bar{\alpha}_S WH} \int_0^H \int_0^W \alpha_S E dx dy \quad (3.11)$$

The resulting overall effectiveness factor for a fixed bulk liquid concentration of 2 g/m³ is given in Figure 3.10 and Figure 3.11 for different aerator configurations and sponge diameters respectively. In both figures, there exists a drop in effectiveness factor at low aeration intensities due to the fact that sponges were settled out of circulation to a stagnant region. Thus, the fluid velocity at aeration intensities below 1 m³/m²h was too low to provide complete fluidization. Above 1 m³/m²h the further increase in effectiveness factor is caused by the increase in slip velocity because of the higher generated velocity and acceleration of liquid flow. In Figure 3.10, it is seen that the overall difference between the aerator configurations is not significant. However, it should be noted that gas hold-up,

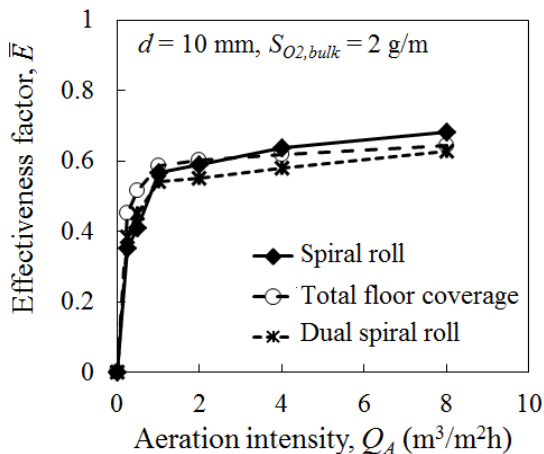


Figure 3.10. Effectiveness factor for different aerator configurations, $d = 10$ mm and $S_{O_2,bulk} = 2$ g/m³.

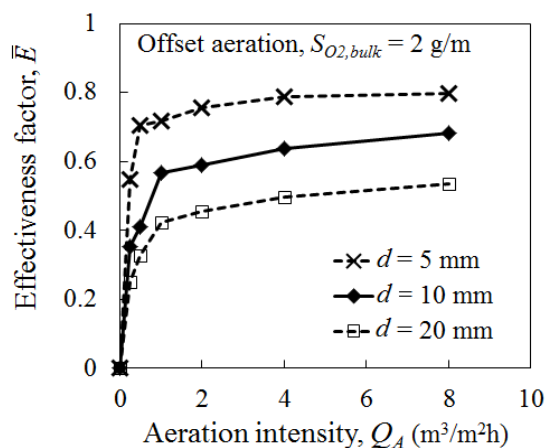


Figure 3.11. Effectiveness factor for the spiral roll aerator and different sponge diameters for $S_{O_2,bulk} = 2$ g/m³.

which is closely related to k_{LA} (Sekizawa *et al.*, 1985), was different among aerator configurations so oxygen transfer from air bubbles to the liquid may differ considerably. In Figure 3.11 it is shown that the overall effectiveness factor is to a large degree affected by sponge diameter and during normal operating conditions ($1-8 \text{ m}^3/\text{m}^2\text{h}$) the reduction of reaction was 47-58 % for 20 mm sponges.

3.3.3 Particle distribution and velocity with time

Figure 3.12 show the particle spatial distribution and particle velocity for different time instants for a moderate aeration intensity of 4 m/h. As initial conditions, the particles were settled to the bottom and formed a packed bed. The bed started to move slightly at 8 seconds in the region above the diffuser. At 16 seconds, a plume was formed which develops into a spiral pattern at 30 s and all particles were fluidized after 1 minute. At 5 minutes, the sponges started to occupy the peripheral regions of the reactor which persisted through 10 minutes and 20 minutes.

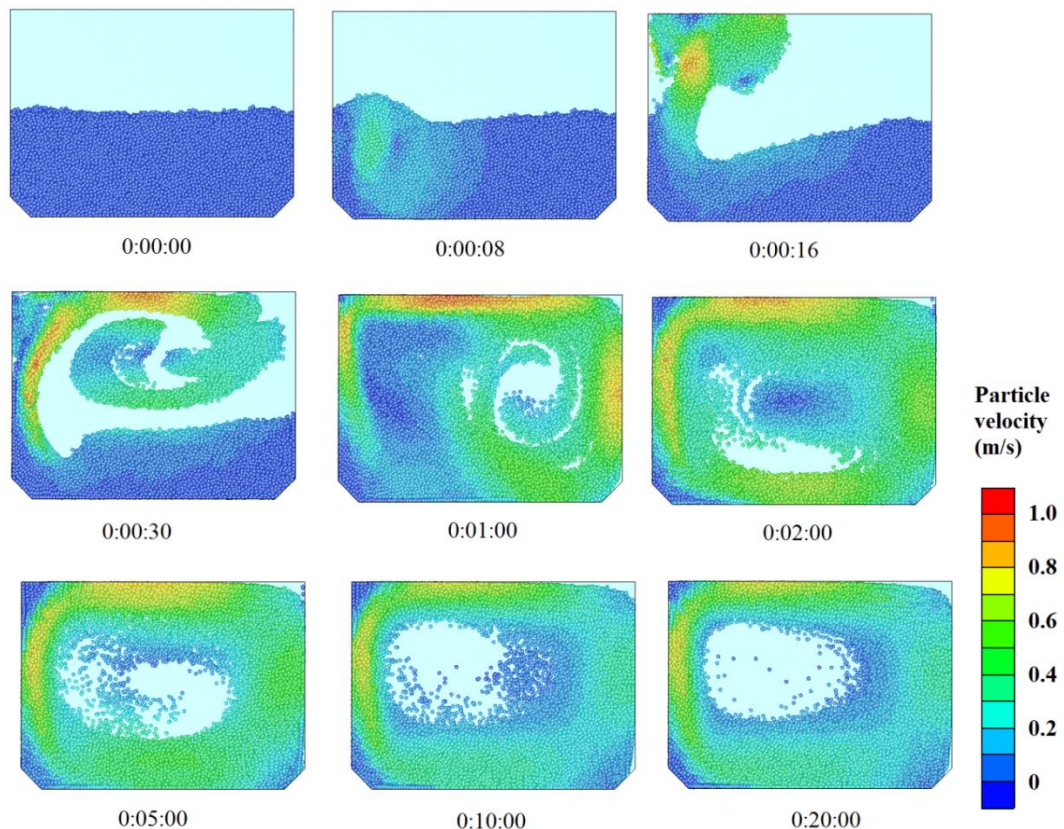


Figure 3.12. Particle spatial distribution and particle velocities for different time instants for an aeration intensity of $4 \text{ m}^3/\text{m}^2/\text{h}$.

Figure 3.13 show the particle spatial distribution and particle velocity for different time instants for low aeration intensity 1 m³/m²/h. Initially and until 1 minute, the development of particle distributions was similar to that of moderate aeration intensities but with a slower rate of change. For instance, the snapshot at 1 minute for 1 m/h is similar to the snapshot at 30 seconds for 4 m/h. However, in contrast to moderate aeration intensities the velocities in some regions are not enough to fluidize the sponges even after 20 minutes. Complete fluidization occurred after 40 minutes after which steady state was reached.

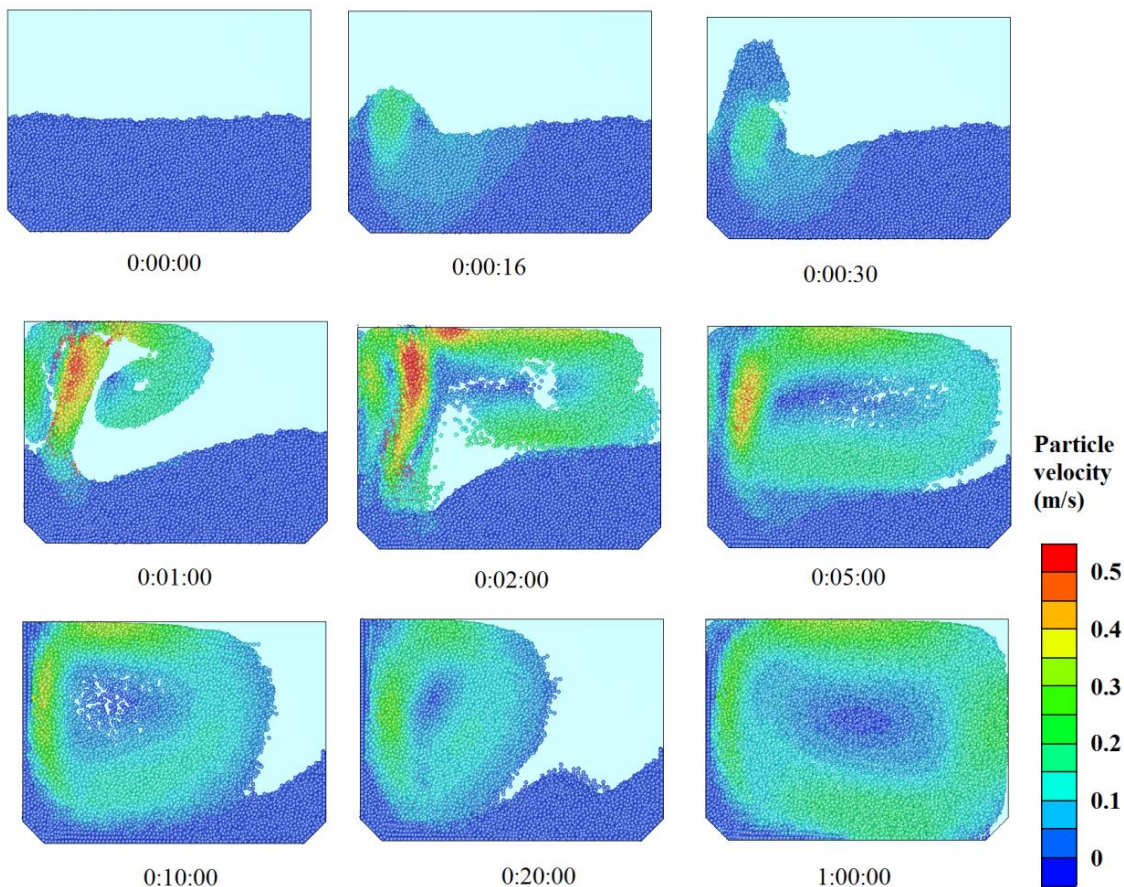


Figure 3.13. Particle spatial distribution and particle velocities for different time instants for an aeration intensity of 1 m³/m²/h.

Figure 3.14 show the particle spatial distribution and particle velocities for the spiral roll configuration and varied aeration intensity. At an aeration intensity of 0.25-0.5 m³/m²/h most of the sponge are settled to the bottom. At 0.5 m³/m²/h, a major part of the sponge are fluidized. However, there is still a settling region present just below the diffuser. An almost complete fluidization occurs at 1 m³/m²/h

with no presence of settling regions. At $2 \text{ m}^3/\text{m}^2/\text{h}$, a part of the sponge move into the peripheral region of the reactor. This tendency is augmented further at $4 \text{ m}^3/\text{m}^2/\text{h}$ and at $8 \text{ m}^3/\text{m}^2/\text{h}$. A possible reason for these phenomena is the slow response time of the sponges which may cause the sponge movement to deviate from the movement of the liquid. This pattern can also be the result of the dense characteristics of the fluid-particle flow (Crowe *et al.*, 1997).

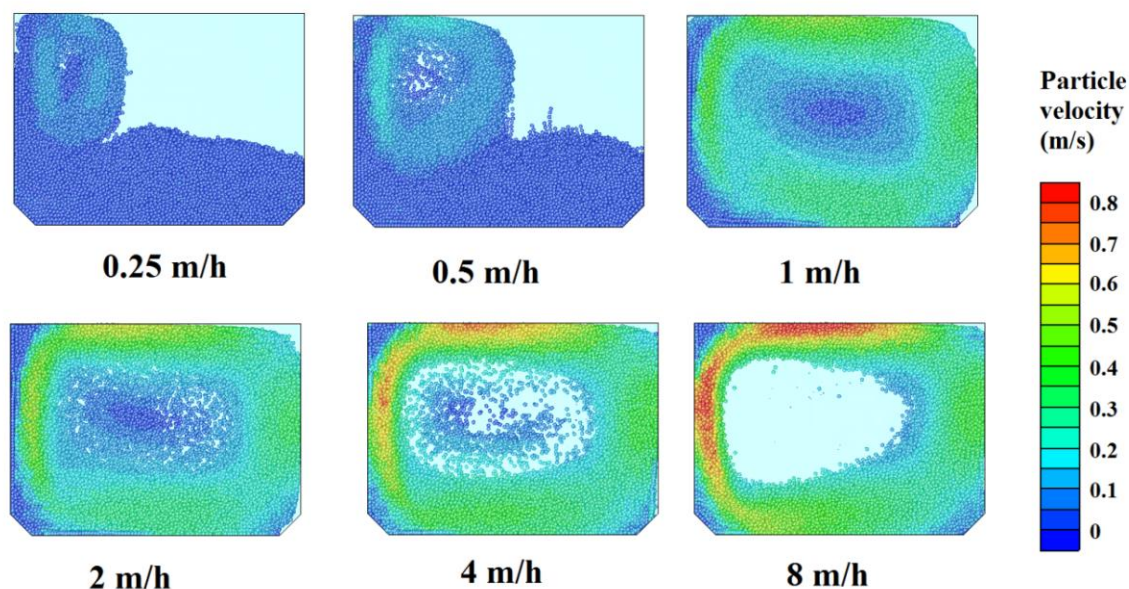


Figure 3.14. Spatial distribution of sponge solid fraction in the reactor in the spiral roll configuration and different aeration intensities.

Figure 3.15 show the spatial distribution of solid fraction from small sponges (5 mm) and large sponges (20 mm) in the spiral roll configuration. The different sponge sizes show very similar settling properties. The larger velocity that is required to fluidize the larger sponges (see terminal velocity in section 3.3.6) is compensated by the lower energy dissipation of the flow due to the lower overall drag forces.

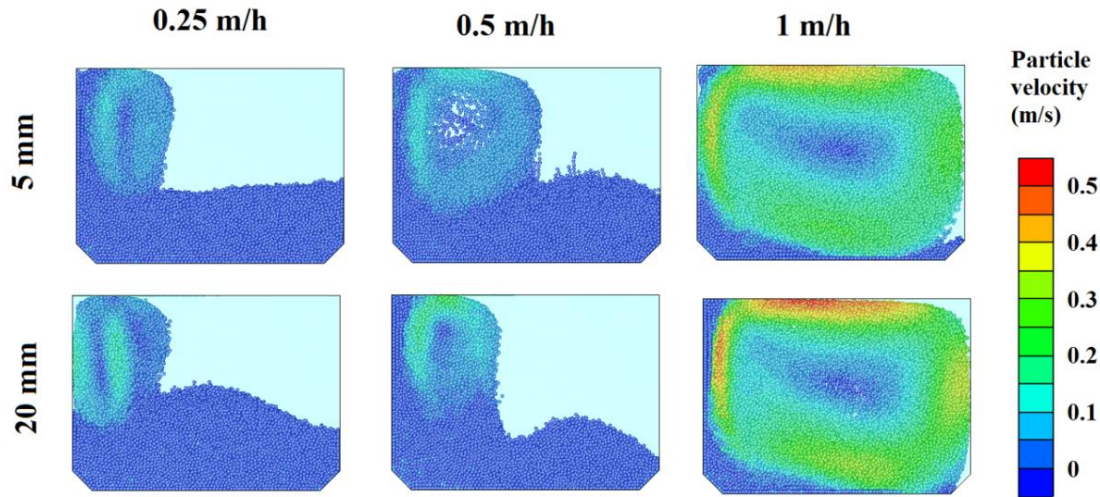


Figure 3.15. Spatial distribution of sponge solid fraction in the reactor in the spiral roll configuration and different sponge sizes and aeration intensities.

3.3.4 Gas hold up

The gas hold up is one of the most influential parameters that affect the oxygen transfer from the bubbles to the liquid by the k_{LA} parameter. Gas hold up is plotted in Figure 3.16 for the spiral roll configuration. As expected, higher aeration intensities caused higher gas hold up in the reactor. The time series of gas hold up were used to check for pseudo steady state which is indicated when the gas hold up shows minor fluctuations in the smaller time scales. Steady state was quickly reached at 1 m/h and 2 m/h and the higher the aeration intensity the longer time for the steady state to be reached. Comparison of gas hold up for different aeration configurations is shown in Figure 3.17 for an aeration intensity of 4 m/h. The flow regime of the total floor coverage configuration was highly unstable which gave a highly fluctuating gas hold up and poor convergence to pseudo steady state. Highest gas hold up was found for the total floor coverage configuration followed by dual spiral roll configuration. The are two major mechanisms that cause a higher gas hold up in these two configurations in comparison to spiral roll: (i) lower velocity in the bubbly zone which increase the retention time of the bubbles and (ii) increased turbulence and granular interaction which keeps bubbles entrapped in the liquid.

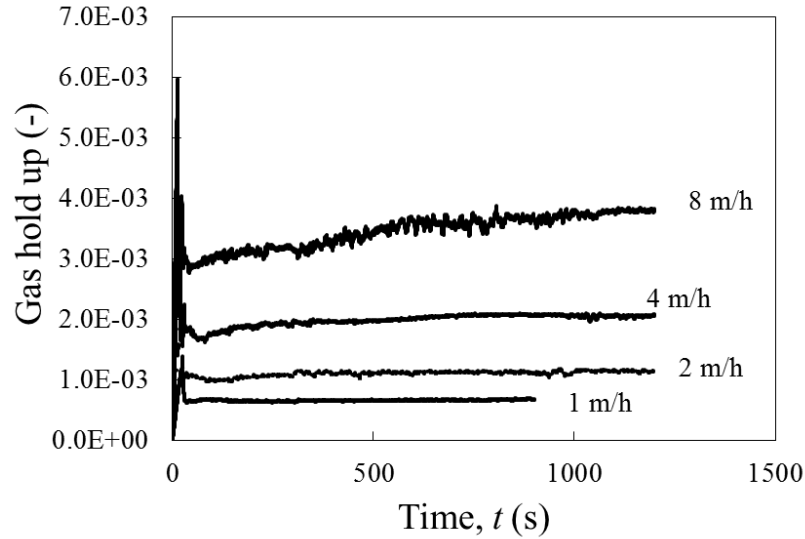


Figure 3.16. Gas hold up in the spiral roll configuration plotted with time and different aeration intensities.

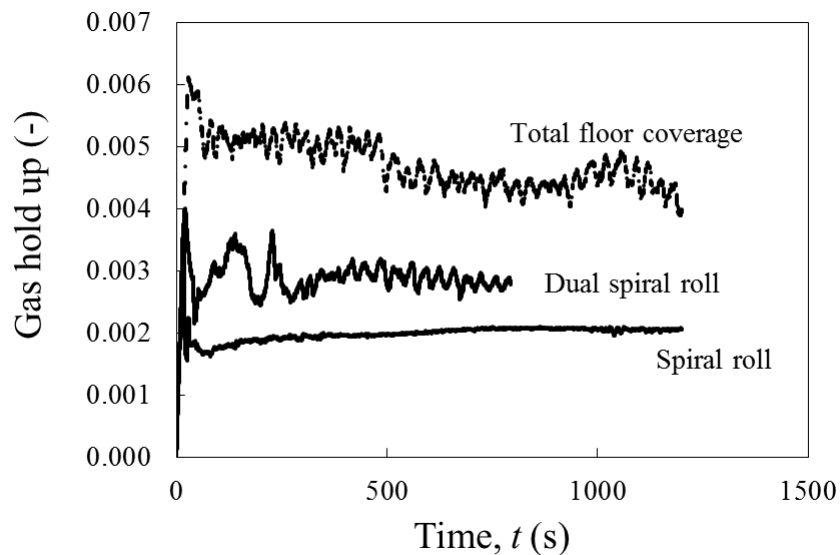


Figure 3.17. Gas hold plotted with time for the different aeration configuration.

3.3.5 Statistical evaluation of the shear stress in the reactor

The statistical distribution of the shear stress of the sponge may answer question about biofilm detachment growing inside and outside the porous matrix of the sponges. From the CFD-DEM simulations, $7 \cdot 10^5$ data samples were taken after the result of gas hold up reached pseudo steady state. Figure 3.18 shows the statistical probability of the shear stress to exceed the value in x-axis under a time step of 0.116 seconds. In Figure 3.19 the resulting return periods of corresponding shear

stresses are shown. According to the results, the overall shear stress is the highest in the spiral roll configuration and lowest in the dual spiral roll configuration. As a result, the return periods for the high shear stresses > 10 Pa that cause biofilm detachment is longer for the Dual spiral roll and the total floor coverage configuration.

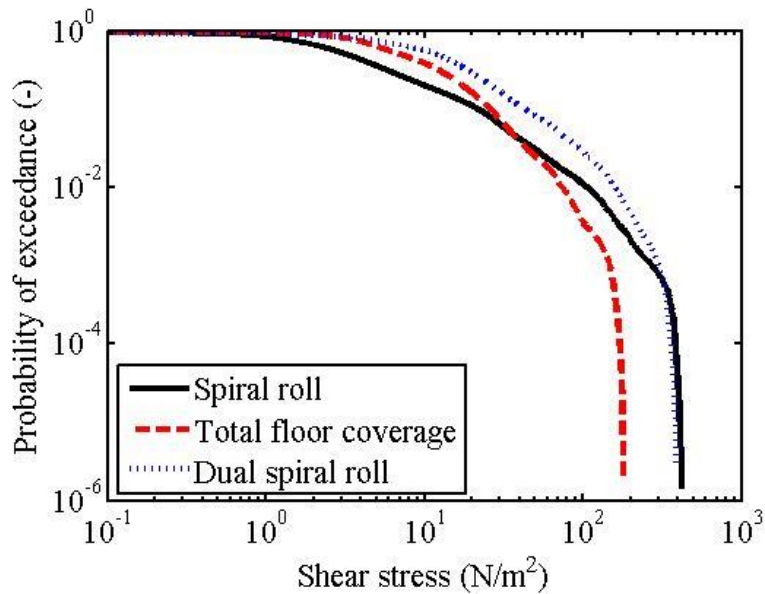


Figure 3.18. Statistical probability of the shear stress at a single particle to exceed the value in x-axis during time step of 0.116 s for the different aerator configurations.

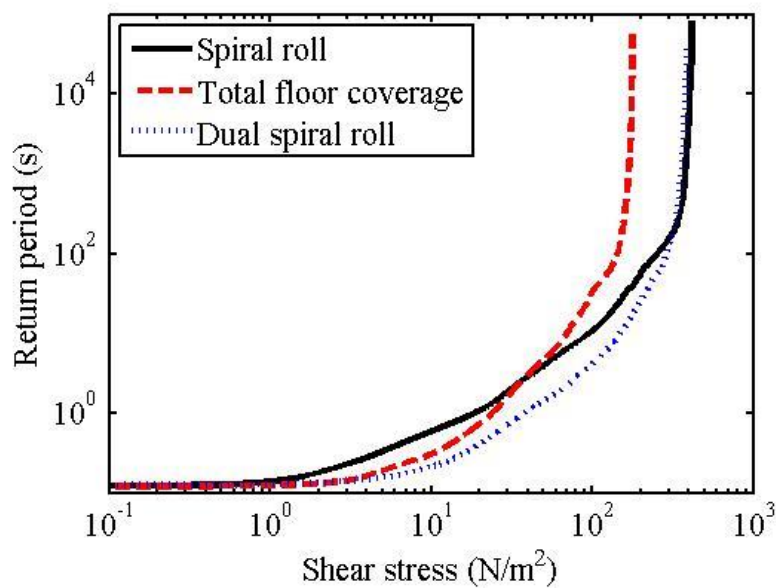


Figure 3.19. Statistical return period of the shear stress at each particle for the

3.3.6 Settling velocity, response time and Stokes number

The behaviour of the solid fraction in the reactor can be explained by settling velocity, response time and the Stokes number. Figure 3.20. Show the settling (slip) velocity plotted with time. The slip velocity increase with time until it reaches the steady state value, the terminal settling velocity U_T . The terminal slip velocity is largely dependent on the size of the sponge where a larger sponge gives a higher U_T . As the response time, t_{res} is largely dependent on the sponge diameter, the slip velocity approaches U_T with a rate inversely proportional to the size of the sponge. As demonstrated in section 0, the Stokes number it is the relative value of the particle response time to the characteristic time of the fluid. Figure 3.21 show the Stokes number plotted with the characteristic velocity in the reactor. The overall values of the Stokes numbers are small which means that the effects of slow response time should be minor.

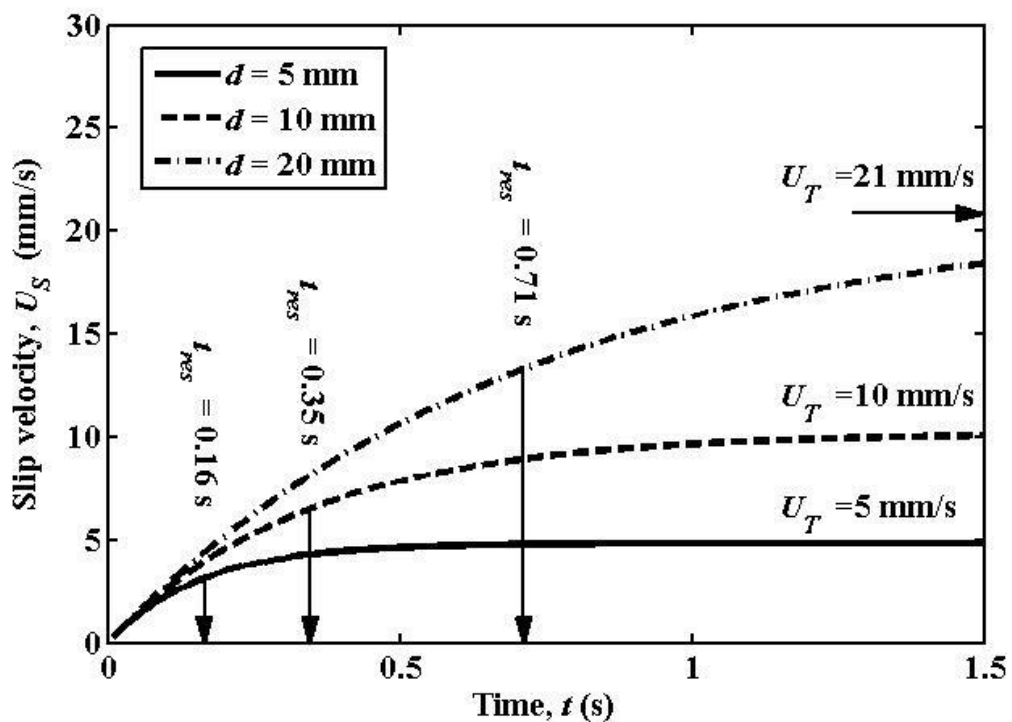


Figure 3.20. Slip velocity plotted with time after exposure and sponge diameters.

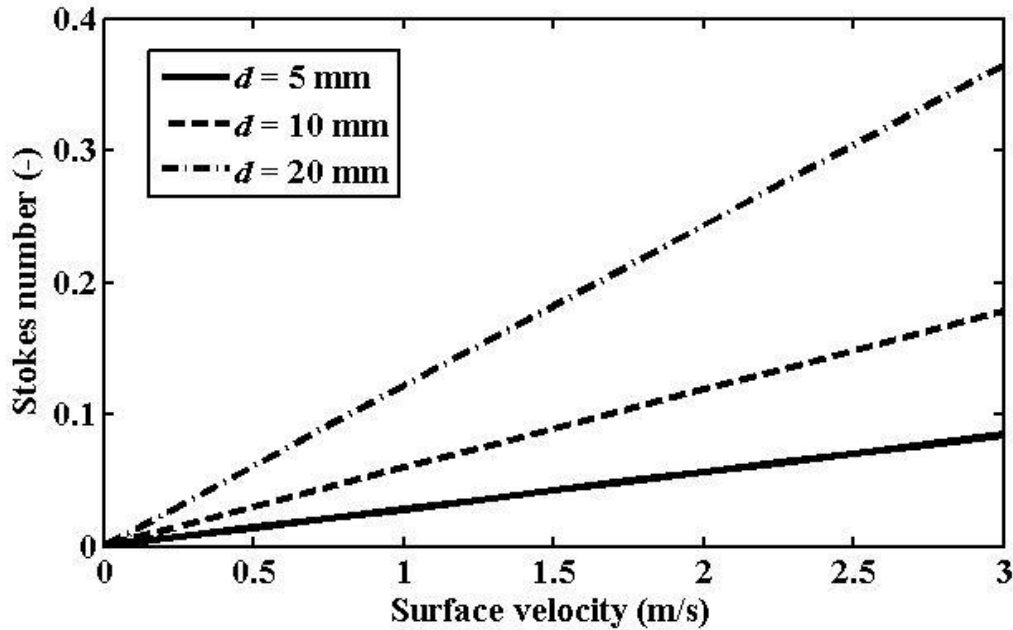


Figure 3.21. Stokes number plotted with surface velocity and sponge diameters

3.4 Discussion

CFD-DEM was used to simulate sponge and air bubbles as particles in a reactor. As explained in section 0 the flow regime of a sponge carrier reactor can be considered as dense if the solid fraction is higher than 12.5%. In the dense regime the flow is characterized by particle collisions which require Lagrangian methods such as CFD-DEM. In this study, the sponge volume fraction was 30 % which was well within the dense regime. Another advantage of CFD-DEM was its ability to simulate sponge settling in cases of low aeration intensities.

A novel method of utilizing CFD-DEM was applied to this study by modelling the sponge as moving porous catalytic pellets. By combining the different parameters into a single non-dimensional variable, Da , the model could explain previous experimental results of augmentation of reaction rate due to hydraulic conditions (Mastui and Deguchi 2002) and the reduction of reaction in large sponges (Guo *et al.* 2010).

By CFD-DEM the statistical distribution of the shear stress could be investigated. The shear stress was investigated in terms of return periods. These return periods should be put in relation to the rate of growth of the biofilm. For example if the

growth rate of the microorganisms in the biofilm of a sponge carrier media is 1/d it will take about a day for the biofilm to recover from damage. The shear stress with return period of 1 day was about 200 N/m². This is much higher than the usual cohesive strength of the biofilm of about 10 N/m² (Coufort *et al.*, 2007). This means that at the surface of the sponge, there is no chance for the biofilm to recover from damage between detachment events. This explains the observation that the biofilm in real reactors grows in the interstitial voids inside the sponge carrier media rather than on the surface because of damping of shear stress. In section 5.2.3, this is studied in more detail by a detachment model with declining rate of detachment with the intracarrier distance.

The results from this study will need a further validation by experimental results. In chapter 7, the substrate flux into the sponge will be calibrated based on kinetic tests (Matsui and Deguchi, 2002) of fluidised sponges in a laboratory reactor. For the hydrodynamics comparisons will be done with experimental results of fluidized sponges in a lab scale reactor. The parameters that can be calibrated are drag coefficients of the non-spherical particles and slide friction coefficients. There are also plans to run the simulation by coupling the two-fluid Euler model for air-liquid with DEM for sponges. In this way it would be possible to improve the accuracy of the turbulence dispersion of the air bubbles.

3.5 Conclusions

Expressing biofilm diffusion with apparent affinity coefficient and the pore mass transfer by the internal velocity; the biofilm reaction inside sponges were modelled. By using CFD-DEM, the slip velocity was obtained and used as a model interface to connect the reactor hydraulics to the internal velocity. Accordingly, the following results were obtained:

1. The reaction rate was found to be governed by a non-dimensional variable, Damköhler number, Da , and an empirical relation for the effectiveness factor was obtained.
2. By coupling the relation to reactor hydrodynamics, it could explain the previous observations that oxygen depletion occurs inside larger sponges

and that biofilm reaction is dependent on hydraulic conditions of the bulk liquid.

3. For the mass transfer from bulk liquid to the sponges, aeration intensity showed a significant impact whereas no significant difference between aerator configurations could be seen.

4 MODELLING THE EFFECT OF BIOFILM MORPHOLOGY ON DETACHMENT

4.1 Introduction

Biofilm detachment is the release of microorganisms from an attached microbial film to the surrounding liquid. It is considered to be the main mechanism to control growth in biofilm reactors (Rittmann *et al.*, 1992). It determines the steady state accumulation, solids retention time (SRT) and hence also the composition of the microorganisms occupying the biofilm (Morgenroth and Wilderer, 2000). In biofilm reactors, there are two major types of biofilm detachment: erosion and sloughing. While erosion is a continuous process at the surface, sloughing is the release of chunks of biofilm from its internal depth (Rittman, 1982, Peyton and Characklis, 1993). Observation of massive biofilm detachment in experimental reactors due to step increase of shear stress has been observed in numerous experiments (Bakke, 1986, Choi and Morgenroth, 2003, Coufort *et al.*, 2007, Paul *et al.*, 2012). Because current empirical models greatly underestimate biofilm detachment in these conditions, this paper describes the development of a new model which more accurately describes biofilm detachment during dynamic change in shear stress.

The first biofilm models of detachment were empirical volumetric rate expressions that varied with shear stress (Rittman, 1982), biomass concentration (Trulear and Characklis, 1982) or biofilm thickness (Bakke *et al.*, 1984). Wanner and Gujer (1986) modified the empirical approach by introducing the concept of detachment velocity. It was defined as the net velocity the biofilm front retreats back towards the substratum as a result of detachment. The concept of detachment velocity was extended by Xavier *et al.* (2005b) for multidimensional biofilm models by assuming that erosion of the biofilm surface could be modelled as a two dimensional continuous function using Level Set Method (LSM). The computational load of these models were minimal but they lacked physical relevance, because they did not solve for the actual breakage of biofilm that causes detachment. Moreover, these models underestimate detachment in cases where shear stress suddenly increases. The detachment rates caused by step increase of shear stress can be of several orders of magnitude larger than detachment rates under a fixed shear stress (Choi and Morgenroth, 2003).

A possible option to solve for shear stress variation in time, is to use mechanistic approaches that solve for the entire continuum mechanics inside the biofilm (Picioreanu *et al.*, 2001, Alpkvist and Klapper, 2007). By using Computational Fluid Dynamics (CFD), the surface shear stress caused by fluid flow was computed. By coupling with Finite Element Method (FEM), the failure of biofilm was predicted when the internal stresses exceeded a critical value, the biofilm strength. This was a more accurate representation of biofilm detachment because the actual breakage of biofilm that caused detachment was calculated. According to the results of Picioreanu *et al.* (2001), biofilm surface detachment due to erosion was higher in local surface peaks due to the higher local shear stress. The disadvantage of these types of models was the high computational load required to perform CFD. This was especially problematic if one wants to simulate biofilm formation over a long period of time where thousands of CFD simulations may be required each time the shape of the biofilm changes.

The model of biofilm detachment in this paper is a combination of the numerically efficient approach of Xavier *et al.* (2005b) and the mechanistic approach of Picioreanu *et al.* (2001). An expression was developed that could simulate the

impact of biofilm local heterogeneities on local shear stress and the resulting effect on biofilm detachment. A recursive algorithm of biofilm detachment was constructed for which erosion of the biofilm surface occur when the shear stress exceeded the strength of the biofilm. A model for biofilm sloughing was implemented by calculation of the bending moment and the internal shear stress in local biofilm structures.

The detachment methods were successfully integrated into an Individual-based Model (IbM) platform of biofilm growth where the individual microbial cells were simulated as particles. The model was also able to simulate massive detachments that occur when the shear stress suddenly increases. The results provide insight on how to maintain useful biofilms in a biofilm reactors or how to effectively remove biofilms in applications where they cause problems (fouling, heat exchangers, diseases etc.).

4.2 Methods

This chapter starts by explaining the implementation of the LSM to calculate interface movements and how it is applied for biofilm detachment. This was done by applying local material failure criteria to the surface and the internal of the biofilm. The following subsections describe how the newly developed detachment model is implemented in multidimensional biofilm models.

4.2.1 Level Set Method

The goal is to calculate the propagation of the interface Γ surrounding the biofilm domain Ω due to detachment. The spatial domains, Ω and Γ are shown in Figure 4.1 (a) together with the biofilm particles. From here it is assumed that, due to erosion, the interface with positions $\mathbf{x} \in \Gamma$ moves with velocity \mathbf{v}_{det} in the negative direction of the interface normal \mathbf{n}_{LF} as follows:

$$\mathbf{v}_{det} = -v_{det} \mathbf{n}_{LF}. \quad (4.1)$$

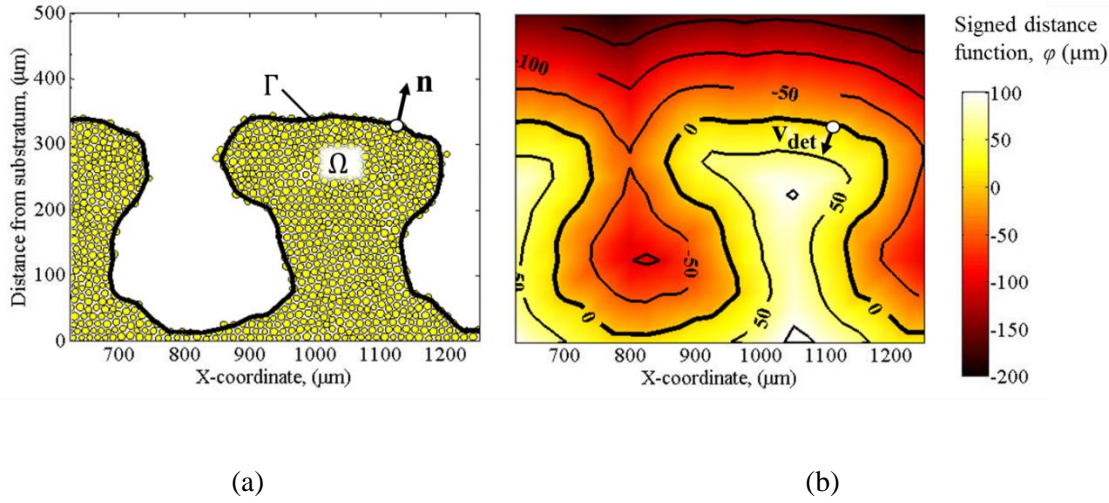


Figure 4.1. The spatial domains of the biofilm and (a) the corresponding signed distance function, φ (b).

Direct calculation of the movement of Γ may cause numerical problems as the curve may twist significantly and cause knots to form. A solution to this problem is the implementation of the LSM. Firstly, the distance $d(\mathbf{x}, t)$ from Γ in the 2 dimensional space is calculated. A level set function $\varphi(\mathbf{x}, t)$ is then defined with the following properties:

$$\varphi(\mathbf{x}, t) = \begin{cases} d(\mathbf{x}, t) > 0 & \text{for } \mathbf{x} \in \Omega \quad (\text{inside biofilm}) \\ -d(\mathbf{x}, t) < 0 & \text{for } \mathbf{x} \notin \bar{\Omega}, \quad (\text{outside biofilm}) \\ 0 & \text{for } \mathbf{x} \in \Gamma \quad (\text{at biofilm surface}) \end{cases} \quad (4.2)$$

φ is shown together with \mathbf{v}_{det} in Figure 4.2 (b). φ is also called the “signed distance function” due to the switching between positive and negative distance functions. Propagation of Γ was solved by the Level Set Equation where the interface movement is analysed by convecting the values of φ with a fictive level set velocity field \mathbf{v} :

$$\frac{\partial \varphi}{\partial t} = -\mathbf{v} \cdot \nabla \varphi = -v_n |\nabla \varphi| \quad (4.3)$$

where v_n is the normal velocity component of the closest interface velocity. Equation (4.3) was solved by using Godunov's first order upwind differencing scheme (Godunov, 1959). For biofilm detachment, Xavier *et al.* (2005b) implemented a special type of level set method called Fast Marching Level Set

(FMLS). The drawback of FMLS is the requirement of non-zero speed of progression which means that detachment due to erosion everywhere has to be higher than zero for this method to work.

4.2.2 Implementation of local mechanical failure criteria on biofilm detachment

Erosion of biofilm was assumed to occur according to von Mises yield criteria (von Mises, 1913) at the position on the surface where the local equivalent tensile stress, τ_{eq} , exceeds biofilm cohesiveness, σ_b . This was done by LSM that was described in previous subsection and the retreat of the biofilm surface was calculated iteratively with the following relation

$$v_{det} = \begin{cases} 0 & \text{if } \tau_{eq} \leq \sigma_b \\ \frac{\tau_{eq} / \sigma_b - 1}{\tau_{eq} / \sigma_b} \delta_{max} & \text{if } \tau_{eq} > \sigma_b \end{cases} \quad (4.4)$$

$$\tau_{eq} = \sqrt{3} |\tau_{shear}| \quad (4.5)$$

where δ_{max} (m) is the maximum allowed displacement distance, equal to half the grid size resolution (25 μm) and τ_{shear} is the surface shear stress. The relation in equation (4.5) comes from von Mises yield criteria, in the condition of pure shear stress (von Mises, 1913) which was assumed at the surface of the biofilm. Because the relation in equation (4.4) is recursive, it is executed repeatedly until there is no point on the surface where α exceeds unity. This is a fundamental difference to the model proposed by Xavier *et al.* (2005b) who assumed erosion to be explained by a continuous function in space and time. Sloughing of biofilm was calculated by estimation of the internal stresses. By Delaunay triangulation, the possible cracks inside the biofilm colonies could be localized, which are shown in Figure 4.2 (a). As shown in Figure 4.2 (b), sloughing occurred along the possible crack with the highest internal equivalent stress $\tau_{eq,i}$, in the case it is higher than the internal biofilm cohesiveness $\sigma_{b,i}$:

$$\sigma_{b,i} < \tau_{eq,i} = 6 \frac{\Delta S}{c^2} \left| \sum_{n=1}^N \tau_{shear,n} \mathbf{t} \times (\mathbf{x}_n - \mathbf{x}_P) \right| \quad (4.6)$$

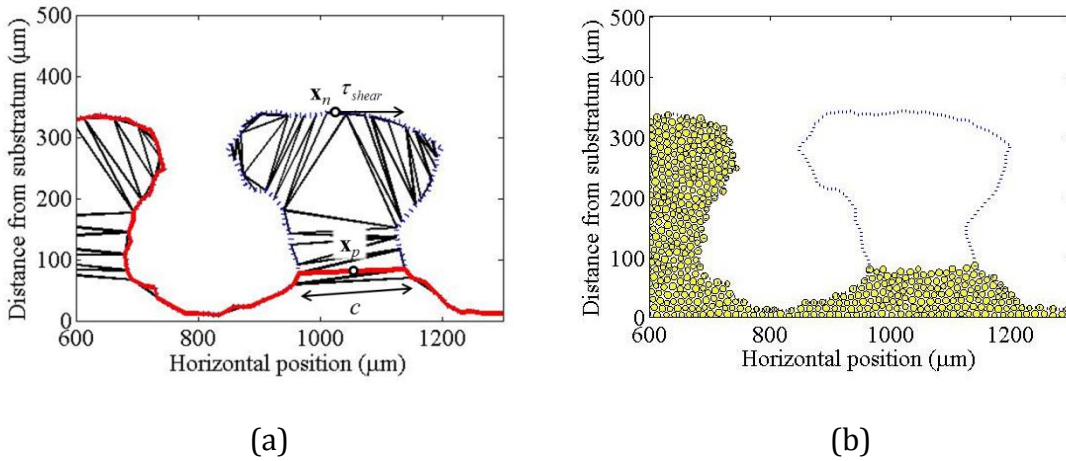


Figure 4.2. Modelling sloughing of biofilm by triangulating the surface points to localize possible cracks (a) and if internal stresses exceed cohesive strength, biofilm colonies are sloughed off (b).

where Δs is the distance between curve points, c is the crack length, n is the index of the set of surface points around biofilm colonies, \mathbf{t} is the tangent of the surface points, \mathbf{x}_n is the surface position and \mathbf{x}_p is the position of the center of the cracks. All biomass that lies outside the newly calculated surface will be removed and a new biofilm surface is obtained. Because biofilms are much more cohesive on the inside (Ohashi and Harada, 1994, Paul *et al.*, 2012), the internal cohesion $\sigma_{b,i}$ that was used for sloughing was assumed to be 10 times higher.

4.2.3 Modelled Shear Stress

An empirical model was developed to simulate the effect of local morphology on local surface shear stress and was fitted with results obtained from numerical simulations of Niavarani and Priezjev (2009). Niavarani and Priezjev (2009) performed CFD simulation on rough surfaces of sinusoidal shapes

$$z = \bar{z} + a \sin(kx) \quad (4.7)$$

where z (m) is the vertical position perpendicular to flow direction, a (m) is the amplitude, k (m^{-1}) is the wave number and x (m) is the horizontal position along the surface. As shown in Figure 4.3, the composite normalized variable $k \cdot a$

determines the shape of the surface. Niavarani and Priezjev (2009) investigated how the local shear stress, τ (Pa), varied with $k \cdot a$ under laminar flow conditions.

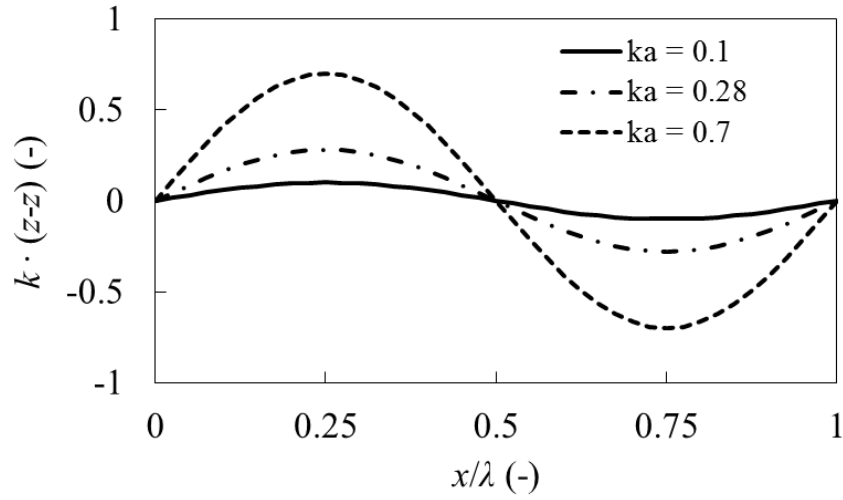


Figure 4.3. Shape of the surface plotted as the normalized roughness of the surface.

As shown in Figure 4.4, two distinct observations could be made: (i) the peak of the shear stress corresponds to the peak of the sine curved surface (at $x/\lambda=0.25$) and (ii) larger variations of shear stress are found for a larger $k \cdot a$. Based on these observations we assume in our model that the shear stress on a biofilm surface depend on the local deviation of z against its average and maximum as follows

$$\tau_{\text{shear}}(z, k) = \tau_{\text{ref}} \left(1 + Ak(z - \bar{z}) \right) e^{Bk(z - \max(z))} \quad (4.8)$$

where A (-) and B (-) were used as fitting parameters to fit equation (4.8) with the numerical results of Niavarani and Priezjev (2009). The wavelength $\lambda = 2\pi/k$ for the biofilm surface, was determined to $450 \mu\text{m}$ from observations of the distance between biofilm fingers, from which $k = 1.4 \cdot 10^4 \text{ m}^{-1}$ was obtained. τ_{ref} is determined by ambient shear conditions and for a laminar flow in a rectangular channel it can be estimated by

$$\tau_{\text{ref}} = 6 \frac{\mu \bar{U}}{W} \quad (9)$$

where \bar{U} (m s^{-1}) is the mean velocity, μ ($\text{Pa} \cdot \text{s}$), the viscosity of fluid and W (m) is the width of the channel.

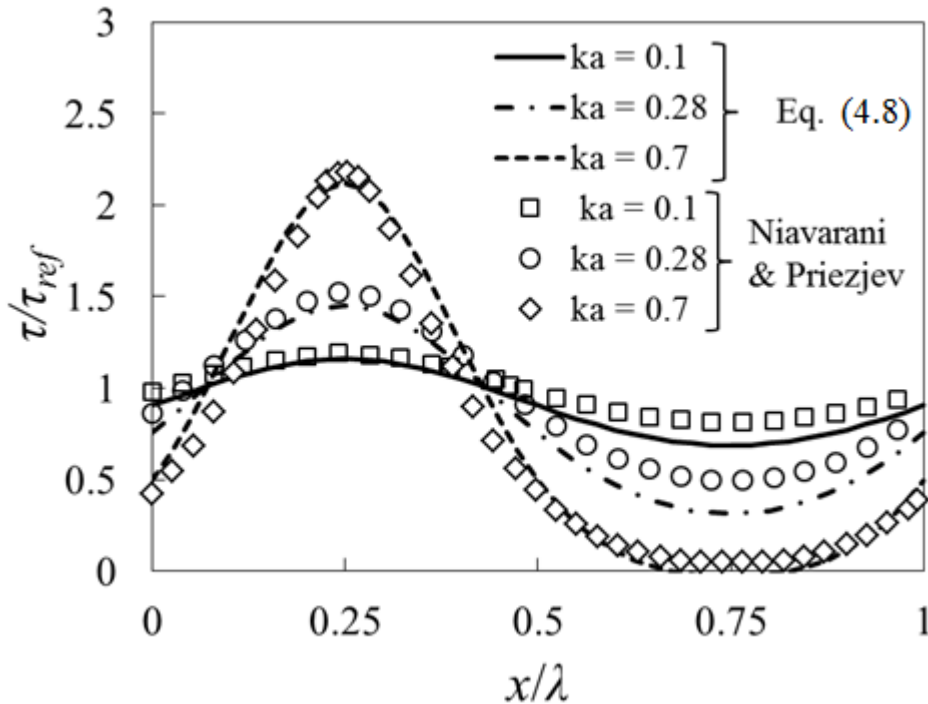


Figure 4.4. Fit of empirical relation in equation (4.2) (lines) against numerical results of Niavarani and Priezjev (2009) (points).

4.2.4 Integration with Multidimensional Biofilm Models

The numerical framework to model biofilm formation consisted of the following steps:

- i. Initial conditions
- ii. Reaction-diffusion algorithm to solve for the oxygen distribution
- iii. Growth and decay of particulate components
- iv. Division of biofilm particles
- v. Shoving of biofilm particles to reduce particle overlap
- vi. Consolidation of biofilm to reduce cavities
- vii. Detachment

As initial conditions (i), a layer of 100 particles of random radii of 5-8 μm are placed along a flat wall. The rest of the processes are simulated in a loop with a time step of 2 hours were the resulting biofilm was composed of about 3000 particles. The parameters used in the simulations are shown in Table 4.1. The framework was simulated using MATLAB® with Statistics Toolbox™. The simulations were run on a conventional PC with an Intel® Core™ i7 Processor.

In the reaction-diffusion algorithm (ii), oxygen S_{O_2} in the biofilm was obtained by using Crank-Nicholson method to solve the reaction-diffusion equation given by

$$\frac{\partial S_{O_2}}{\partial t} = -D_{O_2} \nabla^2 S_{O_2} - \frac{1 - Y_H}{Y_H} \mu_B \frac{S_{O_2}}{K_{O_2} + S_{O_2}} X_B \quad (4.10)$$

where t (d) is time. Around the biofilm, a 200 μm thick diffusion boundary layer was applied. After obtaining the oxygen concentrations, growth and decay (iii) of bacteria was solved. The mass of bacteria m_B and inert m_I in each particle was solved by

$$\frac{\partial m_{B,p}}{\partial t} = \left(\mu_B \frac{S_{O_2}}{K_{O_2} + S_{O_2}} - b \right) m_B \quad (4.11)$$

$$\frac{\partial m_{I,p}}{\partial t} = b f_I m_B \quad (4.12)$$

The radius of the particles could be obtained from the sum of the mass components and a defined density of biomass, ρ_i

Table 4.1 Parameter values used in simulations

Symbol	Value	Expression	Unit	Remark/source
A	1.6		-	This study
B	1.1		-	This study
b	0.6	Decay coefficient	d ⁻¹	(Henze <i>et al.</i> , 2000)
D _{O2}	2·10 ⁻⁴	Diffusion coefficient	m ² d ⁻¹	(Rittmann <i>et al.</i> , 2004)
f _I	0.1	Inert fraction from decay	-	(Henze <i>et al.</i> , 2000)
K _{O2}	0.2	DO affinity coefficient	gm ⁻³	(Henze <i>et al.</i> , 2000)
S _{O2, bulk}	2	DO in bulk	gm ⁻³	
Y _B	0.67	Yield of bacteria	-	(Henze <i>et al.</i> , 2000)
μ _B	6	Max. spec. growth of X _B	d ⁻¹	(Henze <i>et al.</i> , 2000)

$$R_p = \left(\frac{1}{4\pi} \sum_{i=1}^n \frac{m_{i,p}}{\rho_i} \right)^{\frac{1}{2}} \quad (4.13)$$

Upon growth the radius of the particles increased until a threshold value, 8 μm , upon which the particles underwent division (iv). As shown in Figure 4.5 (a-b), a part of the biomass in the mother cell was transferred into a new daughter cell. Figure 4.5 (b-c) illustrates a shoving algorithm (v) that was applied to reduce the overlap of particles caused by growth and division (Kreft *et al.*, 1998). In order to avoid formation of cavities, calculation of consolidation (biofilm shrinking) (vi) was performed to move surrounding particles towards region of decay (Xavier *et al.*, 2005b). This was done by triangulating the biofilm particles and adding attracting spring forces that resembles the cohesive properties of the biofilm. The resulting movement due to consolidation is shown in Figure 4.5 (e-f). At the end of the cycle, detachment (vii) was calculated in the procedure previously described. After each time step of the cycle, the location of a new biofilm surface was calculated and the particles outside this surface are removed.

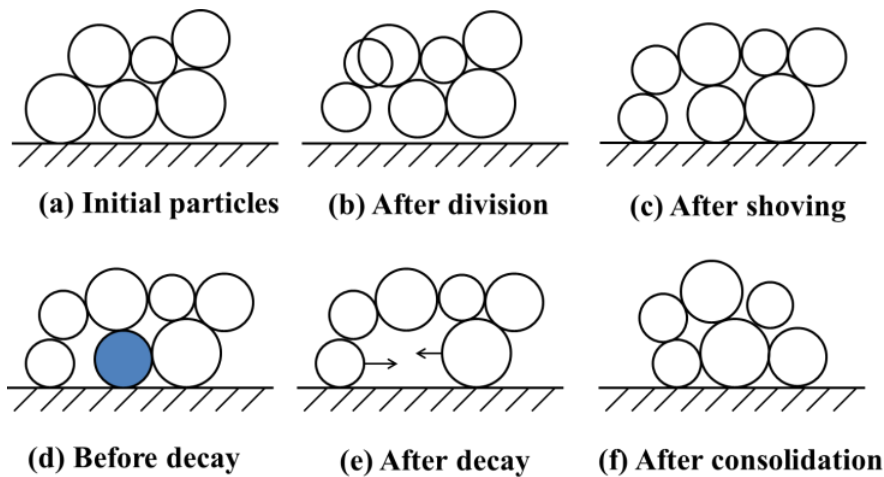


Figure 4.5. Illustration of particle movement during division and shoving (a-c) and the movement during decay and consolidation (biofilm shrinking) (d-f).

4.2.5 Simulation strategy

The simulations were performed with the parameters in Table 1 to investigate the effect of cultivation shear stress and the pulse shear stress on biofilm detachment. In order to study the overall effect of the shear stress on biofilm morphology, a

reference normalized shear stress was defined as the ratio of the reference shear stress to biofilm cohesiveness σ_b (Pa) as follows

$$\alpha_{ref} = \frac{\tau_{ref}}{\sqrt{3} \cdot \sigma_b} \quad (4.14)$$

where the factor $\sqrt{3}$ in the denominator comes from equation (4.5) so that no biofilm can exist for $\alpha_{ref} > 1$ due to erosion. The simulations were performed in two steps. Firstly, biofilm simulation was performed with a constant cultivation shear stress α_{ref} (0.025-1) during 30 days. At day 30 a step increase of shear stress α_{max} (0.05-1) was applied and the resulting detachment was modelled.

4.3 Results

4.3.1 Formation of biofilm with time

Results of biofilm thickness and its morphology are shown in Figure 4.6. Initially, biofilm grew rapidly and then eventually, due to diffusion resistance, the slope of the growth curve flattened out. The average biofilm thicknesses at each time instant were similar among the different shear stresses, however the variation between minimum and maximum were significantly higher at lower shear stresses.

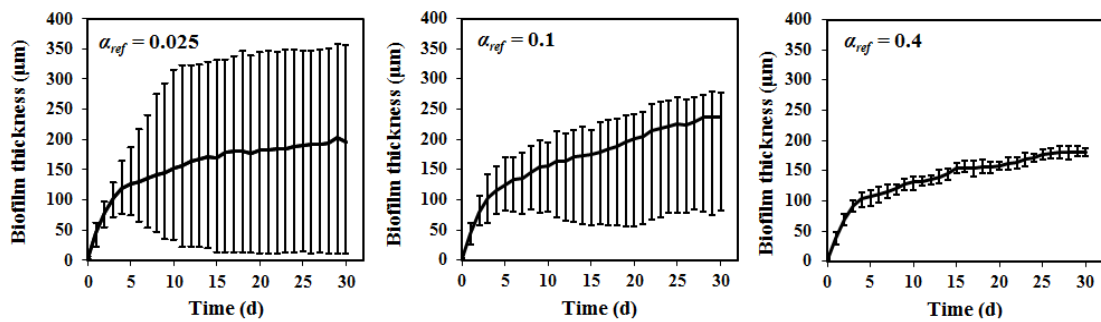


Figure 4.6. Biofilm thickness plotted with different shear stress.

The explanation of the variations of maximum and minimum biofilm thickness lies in the shape of the biofilm which can be seen in Figure 4.7. The low shear case ($\alpha_{ref} = 0.025$) developed a mushroom shaped biofilm whereas a completely flat biofilm developed at higher shear stress ($\alpha_{ref} = 0.4$). The parameter To at the bottom in Figure 4.7 is the tortuosity of the biofilm curve. It is a morphology variable and is

defined as the ratio of the length of the curve of the biofilm surface to the length of the shortest distance between the curve ends.

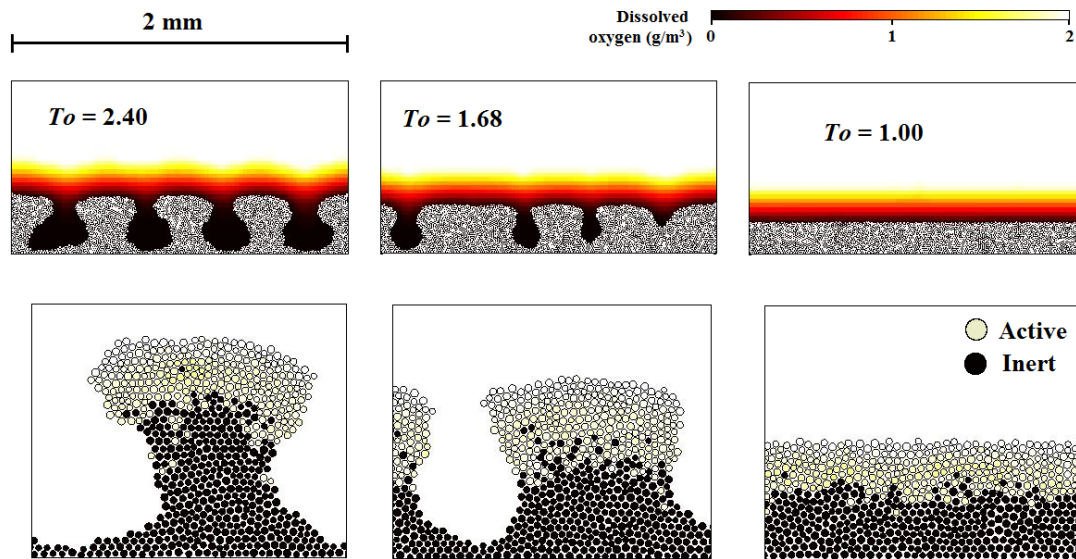


Figure 4.7. Biofilm morphology plotted with different shear stress. The colour scale shows the oxygen concentrations in surrounding liquid at day 30.

4.3.2 Comparison of biofilm formation under constant and pulse shear conditions

The resulting biofilm thicknesses after 30 days of simulation with constant shear stress are shown in Figure 4.8. Starting from low α_{ref} , the average biofilm thickness does not vary much with until α_{ref} exceeds a value of 0.2 after which the average biofilm thickness decreased rapidly. The maximum and minimum biofilm thickness on the other hand varied significantly, especially in the lower range of shear stresses.

The results of the biofilm thickness from pulse shear stress simulations are shown in Figure 4.9. The curves for different α_{ref} are clearly separated which means that the biofilms cultivated in different shear stresses respond differently to an applied shear stress. More biofilm remains for a biofilm grown at high α_{ref} than biofilm in low α_{ref} . The resulting tortuosity after applying constant and pulse shear are shown in Figure 4.10. With increasing shear stress, the tortuosity decreases towards unity. The results for constant and pulse shear conditions show similar trends and values.

It appears that for a certain shear stress, there exists a corresponding threshold value of tortuosity, above which heterogeneities of the biofilm are quickly eroded.

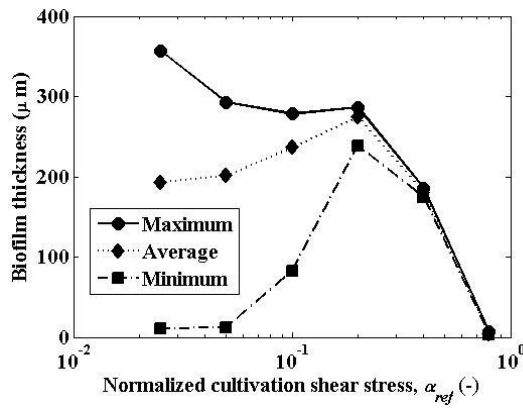


Figure 4.8. Average (solid line) and min/max values (vertical bars) of biofilm thickness shown for the 30 days constant shear

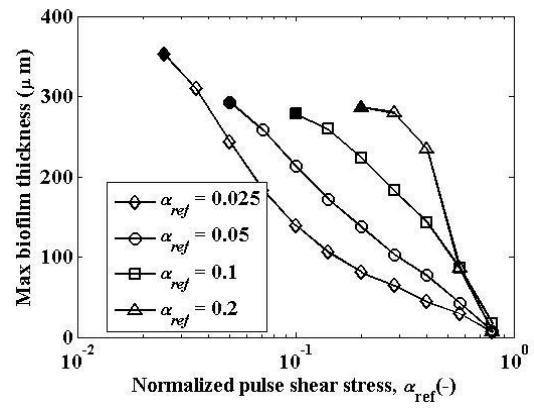


Figure 4.9. Maximum biofilm thickness at low shear conditions followed by a pulse increase of shear stress at day 30 (b).

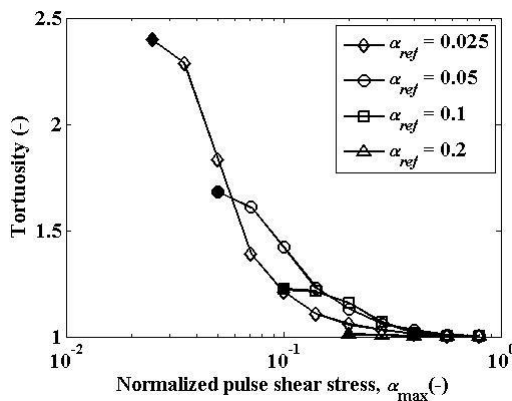


Figure 4.10. Tortuosity of biofilm surface for constant shear stress and pulse shear stress conditions.

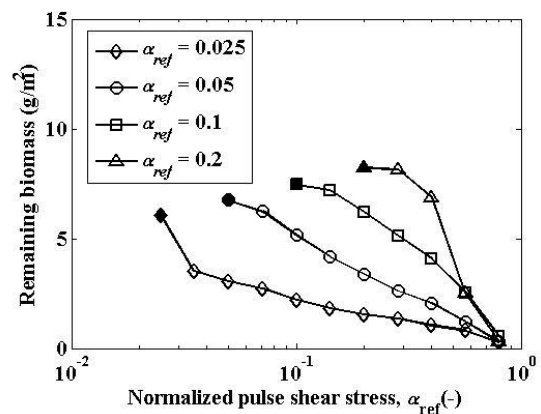


Figure 4.11. Biomass surface density for low shear conditions followed by a pulse increase of shear stress at day 30 (b).

The effect of pulse shear stress on remaining biofilm biomass can be seen in Figure 4.11. For $\alpha_{ref} = 0.025$ a sudden decrease occurs even at low normalized increase of shear stress.

The effect of shear stress magnification of biofilm detachment can be seen in Figure 4.12. For $\alpha_{ref} = 0.025$ a sudden jump occurs at low increase of shear stress.

This was due to triggered sloughing events that detached entire biofilm mushroom colonies. The data for biofilm with a cultivation shear stress in the range $0.05 \leq \alpha_{ref} \leq 0.1$ almost follow a common trend line. However, it also appears that if α_{ref} approaches close to unity, another deviation from the data occurs for $\alpha_{ref} = 0.2$. This is because of high erosion that occurs when the bulk shear stress approach the cohesiveness of the biofilm.

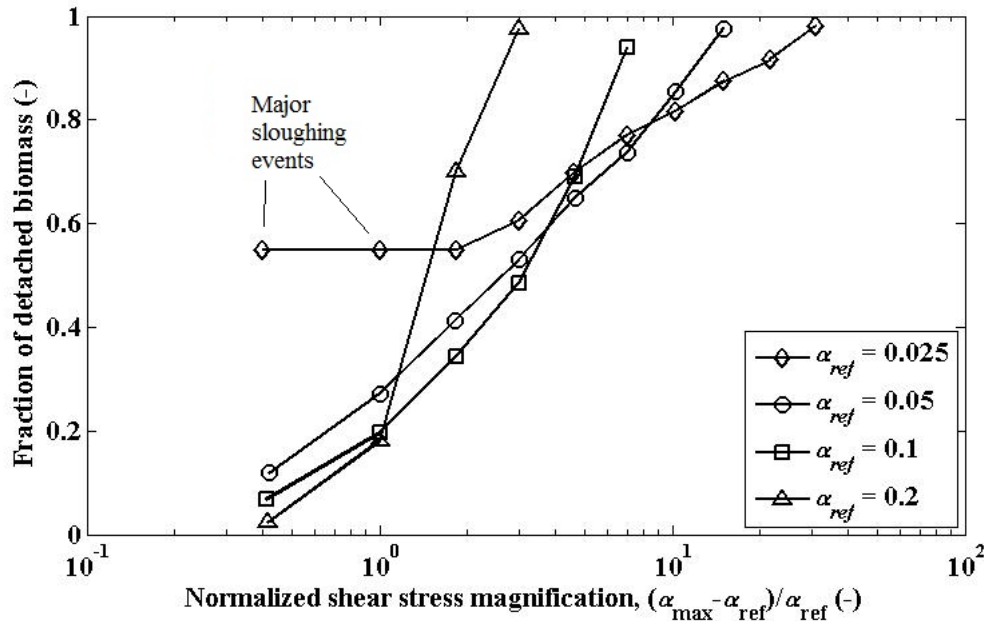


Figure 4.12. Effect of shear stress magnification on fraction detached biomass.

The data ranges show good agreement with Choi and Morgenroth (2003) who observed 30% - 40% of biofilm being detached as the shear stress was tripled (normalized shear stress increase by 2). During the cultivation stage, no sloughing event was recorded. However, in accordance to previous experimental results (Choi and Morgenroth, 2003), sloughing was more pronounced after step increase of shear stress.

4.4 Discussion

There are two mechanisms that lead to the development of mushroom shaped biofilms: (i) higher availability of oxygen in convex parts of biofilm surface which lead to higher local growth and (ii) consolidation of biofilm in decaying regions which move particles towards depressed regions of biomass net production.

Without biofilm detachment initial perturbation of the biofilm surface becomes augmented with time and eventually mushroom shaped biofilm structures are formed.

The observation that less biofilm remains during pulse shear conditions than for constant shear conditions is important in the consideration of cleaning biofilm from surfaces. This observation has been previously seen in several experiments (Coufort *et al.*, 2007, Paul *et al.*, 2012). It appears that one explanation for the weaker biofilm developed in low shear conditions is explained by the shape of the biofilm itself as the shear stress is locally higher when the surface roughness is high. However, in order to remove all biomass, α_{ref} has to be increased to unity. This can also be done by decreasing the biofilm strength by introducing enzymes that degrades the Extracellular Polymeric Substances (EPS). Ideally these chemical should be added after a pulse shear increase where the biofilm thickness has been reduced and the diffusive time for the chemical to penetrate the biofilm has substantially decreased

Since the biofilm cohesion in this study is constant it is necessary to include the effect of the biofilm composition on biofilm cohesiveness. This will be provided in a future paper where the effect of biofilm porosity and Extracellular Polymeric Substances (EPS) on biofilm cohesiveness and detachment will be investigated. In this model, a coupling of generation of EPS and cohesion will be performed. EPS generation can be modelled by utilizing existing models in literature where it can be a part of the mass inside particles (Kreft and Wimpenny, 2001) or as a continuum state variable surrounding the particles (Alpkvist *et al.*, 2006). The novel contribution of the future work is to construct a model of biofilm cohesiveness as a function of the local availability of EPS and porosity and relate it to the shear stress in biofilm to solve for the detachment. In this way, the effect of organisms producing more or less EPS on biofilm detachment can be studied. A model of porosity needs also to be developed as experimental results has shown that the biofilm gradually becomes more compact with time. This kind of model can explain development of compact and strong biofilms that has been observed in previous experimental results (Paul *et al.*, 2012).

4.5 Conclusions

This study provides a numerically efficient method to model how different biofilm morphologies are formed in different environments and an insight on how biofilms can be controlled. This could be performed using a biofilm detachment model integrated into an IBM framework. In the low shear case, biofilm fingering occurred as a combined result of higher growth rates at peaks which gradually augmented biofilm roughness with time. Higher shear stress caused a higher rate of detachment at peaks which suppressed the formation of biofilm fingers.

More biomass was detached from a biofilm that underwent pulse increase of shear stress than biofilms that underwent constant shear stress. This is due to biofilm shape, where the rougher biofilms developed in low shear stress conditions are more susceptible to detachment than the smooth biofilms developed in high shear conditions. Sloughing was more apparent in pulse shear conditions where the release of chunks of biofilm occurred due to internal failure.

5 MODELLING CLOGGING AND BIOFILM DETACHMENT IN SPONGE CARRIER MEDIA

5.1 Introduction

Matsui and Deguchi (2002), who conducted kinetic tests of sponge carrier media, found that apart from molecular diffusion, the biological reaction rate was governed by internal pore convection (mass transfer by fluid flow). This observation, together with fluorescent in situ hybridization observations (Chae *et al.* 2008), suggested that a major part of the reaction occurs by the biofilm attached to the skeletal porous media of the sponge carrier. Biofilm in porous media reduce the permeability of liquid flow in a way that drastically affects mass transfer by clogging (Rittmann 1993). Clogging biofilm has been observed in sponges applied to IFAS processes whereas a less clogging biofilm is found for sponge applied for nitrification (Morper and Linde, 2005). In practise, clogging in IFAS can be reduced by increasing the reactor shear stress, and hence the biofilm detachment due to abrasion, by jostling of sponge media by coarse air diffusers (Morper and Linde, 2005).

Biofilm can be simulated by discrete particles by applying Individual-based Modelling (IbM) (Kreft *et al.* 1998; Kreft *et al.* 2001). IbM was shown to have the ability to track individual cells each with a specified quantity of different biomass

components. Lattice Boltzmann Method has been successfully applied in the simulation of hydrodynamics and mass transfer around biofilm structures (Picioreanu *et al.*, 2001). Pintelon *et al.* (2009) studied clogging in soils in a framework of single species IbM biofilm model and applied Lattice Boltzmann (LB) for the hydrodynamics and mass transfer inside the pores. By using this framework, biofilm formed colonies that were able to block pores in the network, locally reducing the permeability of the porous media.

The main aim of the modeling work presented here was to investigate what factors affect biofilm formation and clogging in sponge carrier media. The model framework was designed to simulate trends observed in experimental results (I) permeability reduction with biofilm growth (Rittmann 1993), (II) effect of hydraulics on biological reaction rate (Matsui and Deguchi, 2002) and (III) effect of shear induced detachment on the permeability and biological reaction rate (Morper and Linde 2005). The framework used in this paper is a development of the framework of Pintelon *et al.* (2009) to be applied for sponge carrier media. In contrast to soils, sponge carrier media is a soft material that deforms upon collisions. A biofilm detachment model for sponge carrier media was developed that considered the internal damping effect during carrier collisions. The IbM biofilm model simulated microorganisms that produce EPS (Extracellular Polymeric Substances) upon growth. EPS production is essential as it occupies a lot of space per unit COD mass which increase the clogging inside sponge carrier media.

5.2 Modelling framework

The algorithm of the sponge carrier media, developed in MATLAB® is shown in Figure 5.1. It combines LB hydrodynamics and mass transfer of the sponge pore water with a biofilm model for the biomass. Biomass was initialized by randomly placing biomass particles at the sponge skeletal surface. The positions of biofilm particles formed the geometric obstacles in the LB hydrodynamic solver after which LB mass transfer was calculated to obtain the oxygen distribution. The oxygen distribution was used as an input in the IbM model where growth, division, shoving and detachment were simulated before finishing the iterative loop. The parameter values used in this study are listed in table 5.1.

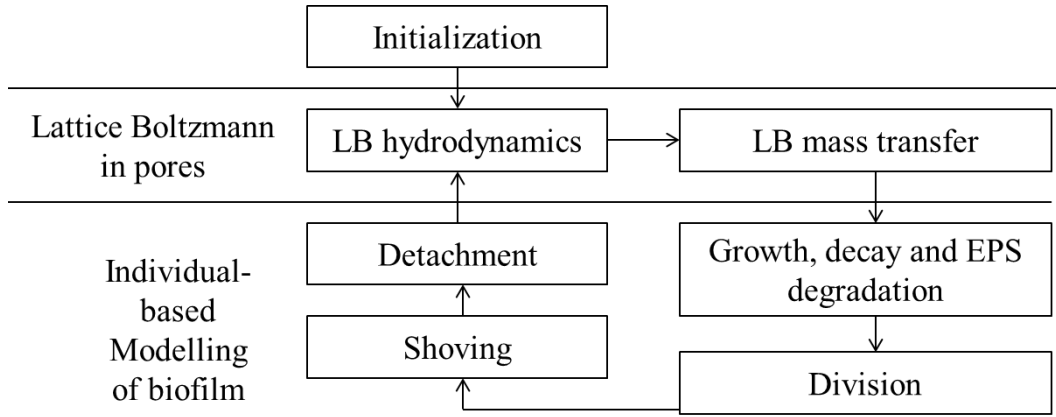


Figure 5.1. The iterative circle of the framework including hydrodynamics, mass transfer and consumption of oxygen due to microbial processes.

5.2.1 LB hydrodynamics and mass transfer

A sponge of 10 mm in diameter, 28 pores per inch and an empty porosity of 0.97 was modelled in the simulation. To simulate the flow entering the sponge carrier media the pressure gradient along the sponge needed to be calculated. For an aerator in a spiral roll configuration, the sponges will most of the time be present outside the bubbly zone in a sinking stage (So *et al.*, 2012). Therefore it was assumed that the pressure gradient was in equilibrium with the negative buoyancy (sinking) as follows:

$$\nabla p = (\rho_s - \rho_w)g\alpha_s \quad (5.1)$$

Two different LB methods were used to solve the hydrodynamics and the mass transfer on a square grid network of 30 μm mesh size. For the hydrodynamics, LB method with Lattice Bhatnagar-Gross-Krook (LBGK) approach in 2D (Succi, 2013) was used to solve for the velocity vector \mathbf{u} (m/d) in Navier-Stokes equations;

$$\frac{\partial \mathbf{u}}{\partial t} + \mathbf{u} \cdot \nabla \mathbf{u} = -\frac{1}{\rho_w} \nabla p + \nu \nabla^2 \mathbf{u} \quad (5.2)$$

$$\nabla \cdot \mathbf{u} = 0 \quad (5.3)$$

No-slip boundary conditions was applied at the biofilm surface and constant pressure was applied at the outlet. For simplicity biomass reaction was assumed to be rate limited on oxygen. A LB scheme based on Flekkøy (1993) was used to solve

for the oxygen concentration, S_{O_2} , (g/m^3), in the advection-diffusion-reaction equation;

$$\frac{\partial S_{O_2}}{\partial t} = -\mathbf{u} \cdot \nabla S_{O_2} - D_{O_2} \nabla^2 S_{O_2} + r_{O_2} \quad (5.4)$$

where r_{O_2} ($\text{g}/\text{m}^3\text{d}$) is a (negative) reaction source term of S_{O_2} . Bulk liquid was completely mixed with fixed oxygen concentration, no flux boundary conditions were applied at the walls and zero oxygen gradient was applied at the outlet.

5.2.2 Growth, decay and EPS degradation

The process map and parameters used in this study were obtained from Alpqvist *et al.* (2006) which includes microorganisms (X_B), inert (X_I) and EPS (X_E) (g/m^3). X_E was generated by the growth of X_B . Petersen matrix in table 5.2 was used to link the processes with the soluble, S_i , and particulate, X_i , state variables.

In lbM, growth of microorganisms increased the radius of biomass particles until a threshold value, $8 \mu\text{m}$, upon which the particle was divided into two. A shoving algorithm was used to reduce the overlap of particles caused by growth and division (Kreft *et al.* 1998). During decay and EPS degradation a reverse shoving process was performed to bring shrinking particles closer to each other as described by Xavier *et al.* (2005a).

Table 5.1 Petersen matrix of the transformation processes in the biofilm.

Process name	Soluble components	Particulate components			Process rate
		S_{O_2}	X_B	X_I	
1 Growth of microorganisms	$-\frac{1 - Y_B - Y_E}{Y_B}$	1		$\frac{Y_E}{Y_B}$	$\mu_H \frac{S_{O_2}}{K_{O_2} + S_{O_2}} X_B$
2 Decay of microorganisms		-1	Y_I		$b_H X_B$
3 Degradation of EPS				-1	$b_E X_E$

5.2.3 Biofilm detachment

At the biofilm surface, the interface speed $u_{interface}$ (m/d) in the normal \mathbf{n} (-) direction of the biofilm was given by;

$$u_{interface} = \mathbf{n} \cdot \mathbf{u}_j - u_{det} \quad (5.5)$$

where \mathbf{u}_j is the movement of nearest biomass particle, u_{det} (m/d) is the biofilm detachment velocity. A distance function from the biofilm surface was resolved on a square grid and $u_{interface}$ was solved using Level Set Method (LSM) (Sethian, 1996, Xavier *et al.*, 2005b). After each calculation of the LSM, the position of the interface was recalled back again on iso-curves where the distance function was zero. The detachment velocity was calculated using the following empirical relation (Xavier *et al.*, 2005b):

$$u_{det} = k_{det} L_F^2 \quad (5.6)$$

where k_{det} (1/m·d) is the detachment coefficient and L_F (m) is the local biofilm thickness. k_{det} resembles reactor shear stress which depend on frequency and intensity of carrier collisions. These are influenced by carrier volume fraction, carrier size, and power input by aerators or mixing devices (Gjaltema *et al.*, 1997). The relation to the square of biofilm thickness fitted well to experimental results and ensured a steady state biofilm (Stewart 1993). In order to adapt this relation for sponge carrier media an exponential term was newly added;

$$u_{det} = k_{det} L_F^2 e^{-c\delta} \quad (5.7)$$

where c (-) is the exponential reduction coefficient and δ (-) is the intracarrier distance normalized with the carrier radius. The exponential relation is related to the force of impact of collisions of sponge carrier media. The reference value of k_{det} (1000 1/m·d) was chosen to obtained appropriate biofilm thicknesses (see the results section) and corresponded to the higher range utilized by Xavier *et al.* (2005b). For simplicity the reference value of c was set at $\ln(5) = 1.61$ so that the middle of the sponge experienced a theoretical shear force scaled by 1/5 to the shear force at the sponge surface. The variation of the detachment speed function with δ , c and biofilm thickness is plotted as a line graph in Figure 5.2 and as a contour plot in Figure 5.3.

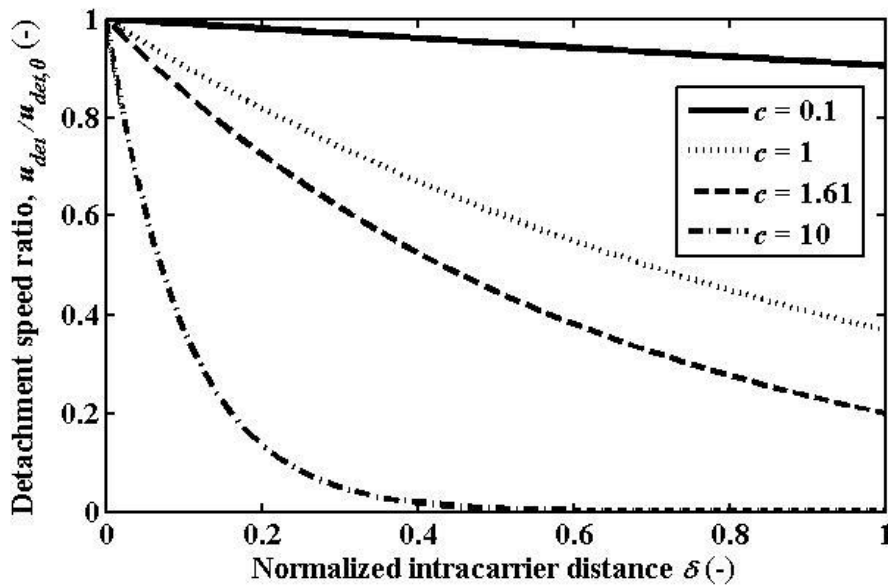


Figure 5.2. The ratio of internal and surface detachment velocity obtained from equation (5.7) plotted with δ for different values of c .

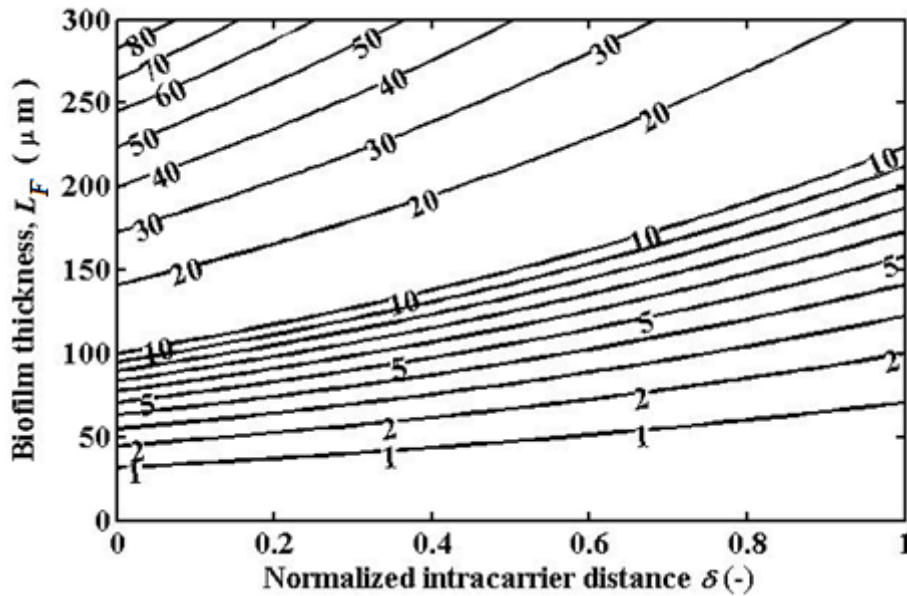


Figure 5.3. Contour lines of the detachment velocity function, u_{det} ($\mu\text{m}/\text{d}$) in equation (5.7) for the reference case, $k_{det} = 1000 \text{ m}^{-1}\text{d}^{-1}$ and $c = 1.6$.

5.3 Results

5.3.1 Distribution of velocity and oxygen in pores

The spatial distribution of biomass, velocity and oxygen inside the pores of the sponge carrier media are shown in Figure 5.4 for the reference case ($S_{O_2, bulk} = 2$

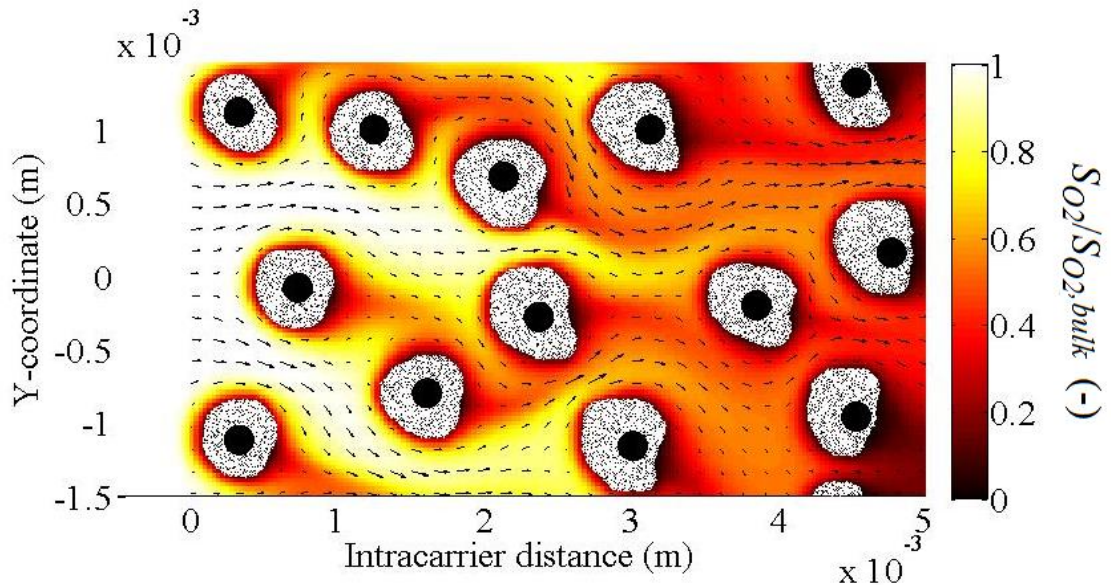


Figure 5.4. Results of oxygen (colour map), biomass distribution (white regions) and velocity distribution (arrows)($g/m^2 \cdot d$) at day 10 for $S_{O_2, bulk} = 2 g/m^3$ and $k_{det} = 1000 m^{-1}d^{-1}$.

g/m^3 and $k_{det} = 1000$) at day 10. In these conditions, biofilm grow homogeneously inside the sponge carrier media. In this case, clogging is limited which can be seen by the well distributed velocity arrows. This allows oxygen to easily penetrate the pores of the sponge carrier media

5.3.2 Change of bio-clogging with time progression

Figure 5.5 compares the formation of biofilm at day 1 with formation at day 10 for $S_{O_2, bulk} = 2 g/m^3$ and $k_{det} = 500 1/m \cdot d$. Homogeneous growth was seen at day 1 and discontinuous biofilm with finger formation blocking the pore throats was seen at day 10. The finger formations are the result of higher local biofilm growth at the pore throats due to higher oxygen concentrations. This biofilm formation has a large impact on permeability because it blocks the narrowest sections for fluid flow.

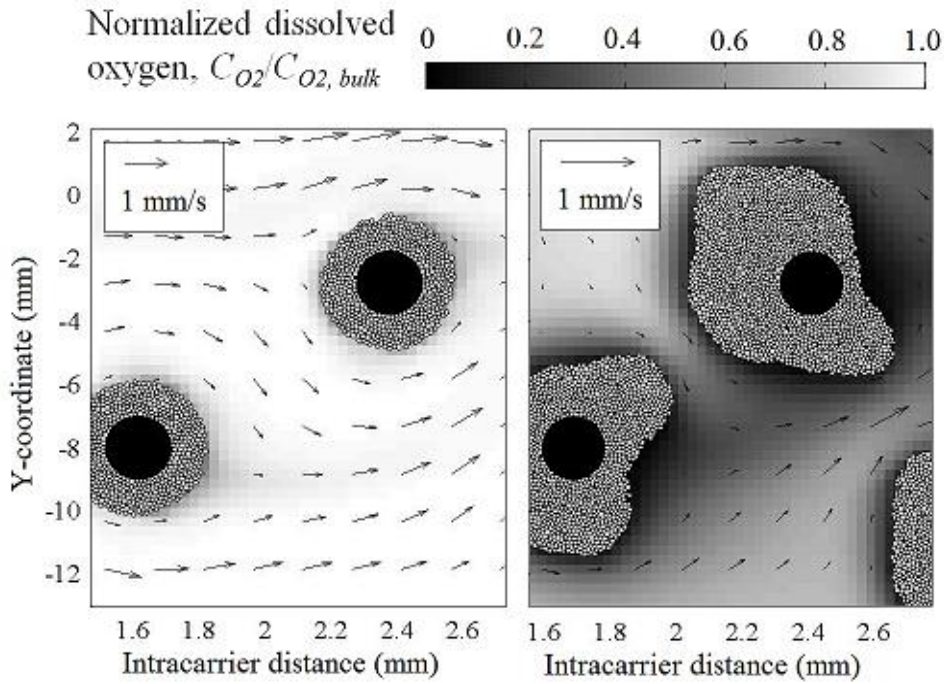


Figure 5.5. Biofilm formation at day 1 (left) and day 10 (right) for $S_{O_2,bulk} = 2 \text{ g/m}^3$ and $k_{det.} = 500 \text{ 1/m}\cdot\text{d}$.

5.3.3 Sensitivity analysis

Figure 5.6 (a) shows the oxygen flux J_{O_2} , plotted with time for different detachment coefficients, $k_{det.}$ All curves displayed similar behaviours with initial rapid increase until day 1 followed by a slow reduction. The sensitivity analysis of the stable state oxygen flux is shown in Figure 5.6 (b). The highest sensitivity was attributed to the yield of EPS production (Y_E), the density of EPS, ρ_E , and the detachment coefficient $k_{det.}$ The sensitivity of $k_{det.}$ showed highly non-linear response with a dip at $250 \text{ 1/m}\cdot\text{d}$. The sensitivity of detachment reduction coefficients, c , was moderate.

Time series of permeability (m^2) is shown in Figure 5.7 (a). An almost exponential reduction with time was developed. Higher $k_{det.}$ resulted in higher permeability. The sensitivity analysis of the stable state permeability is shown in Figure 5.7 (b). As with J_{O_2} , the highest sensitivity was attributed to the yield of EPS production (Y_E), the density of EPS, ρ_E , and the detachment coefficient $k_{det.}$ In comparison to J_{O_2} permeability was more sensitive to changes in $k_{det.}$

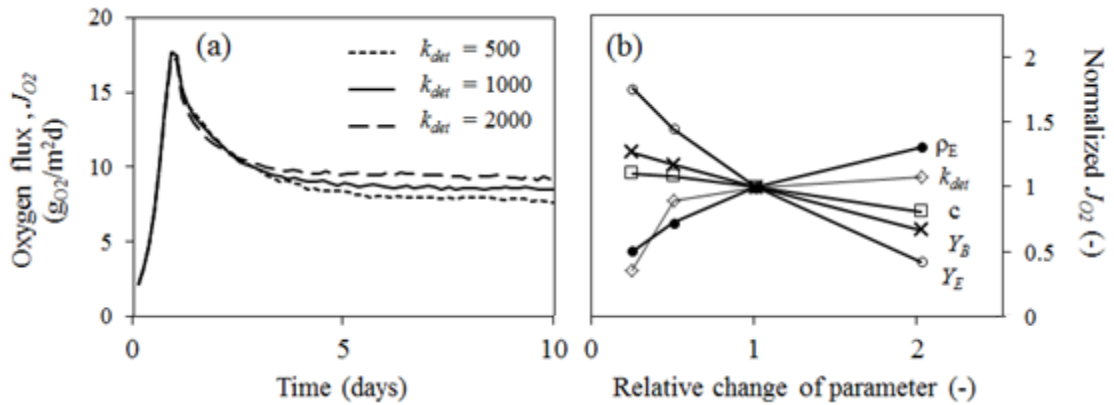


Figure 5.6. Time series of oxygen flux with the reference case and different k_{det} . The corresponding parameter sensitivity analyses at day 10 for the reference parameter sets are shown in (b).

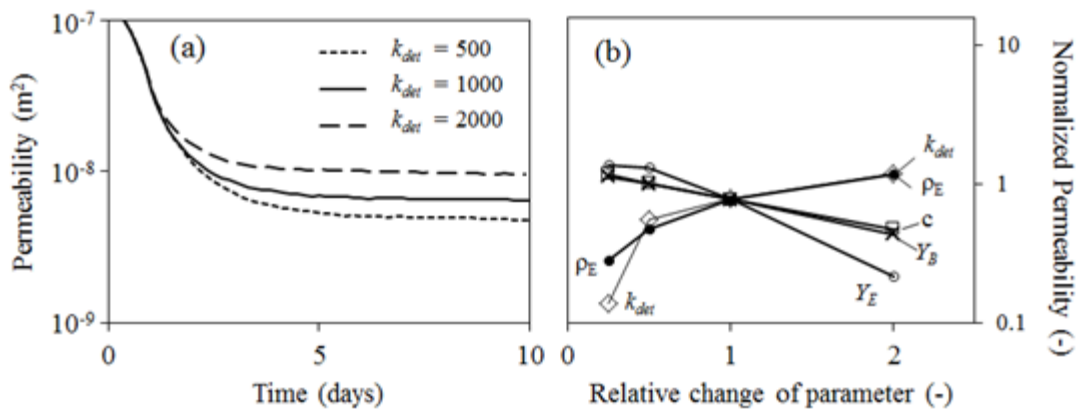


Figure 5.7. Time series of permeability with the reference case and different k_{det} . The corresponding parameter sensitivity analyses at day 10 for the reference parameter sets are shown in (b).

5.3.4 Effect of operational conditions on bio-clogging in sponge carrier media

The effect of operational conditions on the biofilm oxygen flux is plotted in Figure 5.8. As expected oxygen flux increases with bulk oxygen concentrations except for the case of $k_{det} = 500$ and $S_{O_2, bulk} = 4$ g/m³. The explanation can be seen in Figure 5.9 where the results of the distribution of oxygen and biomass at different $S_{O_2, bulk}$ and k_{det} are displayed. Higher $S_{O_2, bulk}$ and lower k_{det} resulted in a higher DO stratification and a biomass that occupied the near surface region. The reverse was developed for lower $S_{O_2, bulk}$ and higher k_{det} were stratification of DO was low and

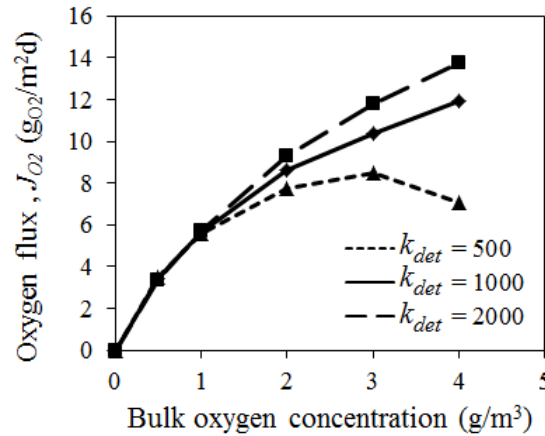


Figure 5.8. Steady state oxygen flux, depending on bulk oxygen concentration and detachment coefficient k_{det} .

biomass developed at the inner regions of the sponge. For the case of $S_{O_2, bulk} = 4$ and $k_{det} = 500$, thick biofilm clusters blocking the pore throats was seen. This biofilm formation had a large impact on permeability because it blocked the narrowest sections for fluid flow. The range of biofilm thickness in the simulations (50-250 μm) were in good agreement with experimental results of Chae *et al.* (2008)

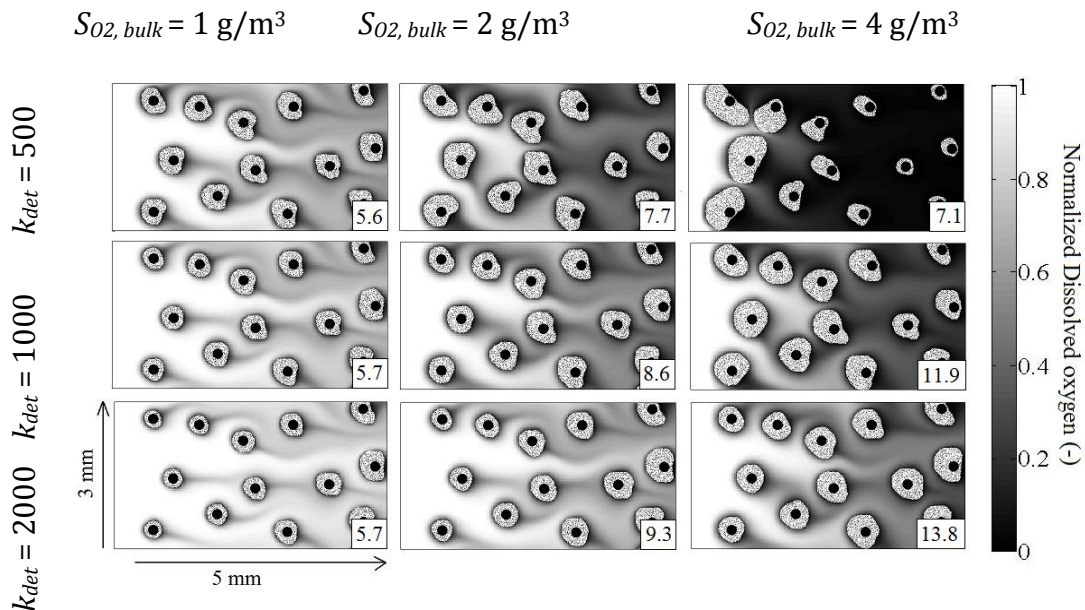


Figure 5.9. Results of oxygen (grayscale), biomass distribution (white regions) and oxygen flux (numbers)(g/m²-d) at different bulk oxygen concentrations and detachment coefficients.

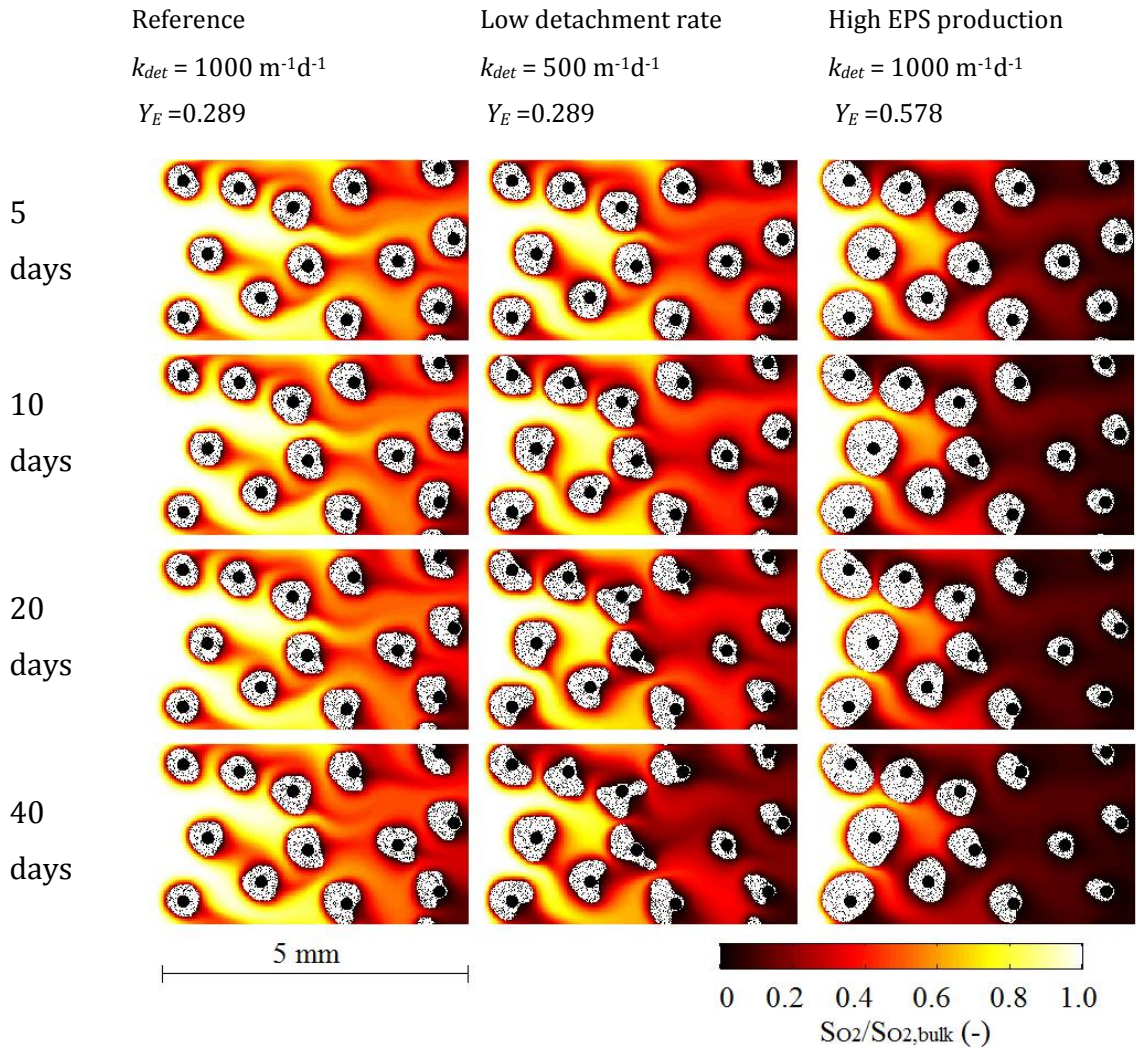


Figure 5.10. Long term biofilm formation for the reference case, low detachment case and a case with high EPS production.

5.3.5 Long term simulation with varying rate of detachment and EPS production

Long term simulations were conducted with different k_{det} and Y_E to investigate the mechanisms behind the high sensitivity of these parameters on the oxygen flux and permeability observed in Figure 5.6 and Figure 5.7. The long term simulations with the reference case, low detachment case and the case of high EPS production are shown in Figure 5.10. For the reference case, biomass is homogeneously distributed on the skeletal surface of the sponge carrier media and has reached a steady state at around day 20. For the low detachment case, fingering of the biofilm started at day 10 and was gradually increased with time. As mentioned earlier on

chapter 5.3.2, fingering causes additional clogging as these grow in the throats of the pores and chokes the flow. This is demonstrated in more detail in Figure 5.11 which is a close up of the simulation at day 40. Detachment did not seem to have large impact on the presence of EPS inside the sponge carrier media. Higher production of EPS also caused augmented clogging but with different mechanisms in comparison to low detachment. Higher EPS production increased the volume expansion rate of the biofilm significantly. This caused the steady state biofilm thickness to be thicker. As shown in Figure 5.11, it causes formation of a biofilm with a very high volume occupancy of EPS. In comparison to the low detachment case, clogging occurred closer to the surface of the sponge carrier media. Even though the volume of the biofilm increased significantly biofilm fingering was limited.

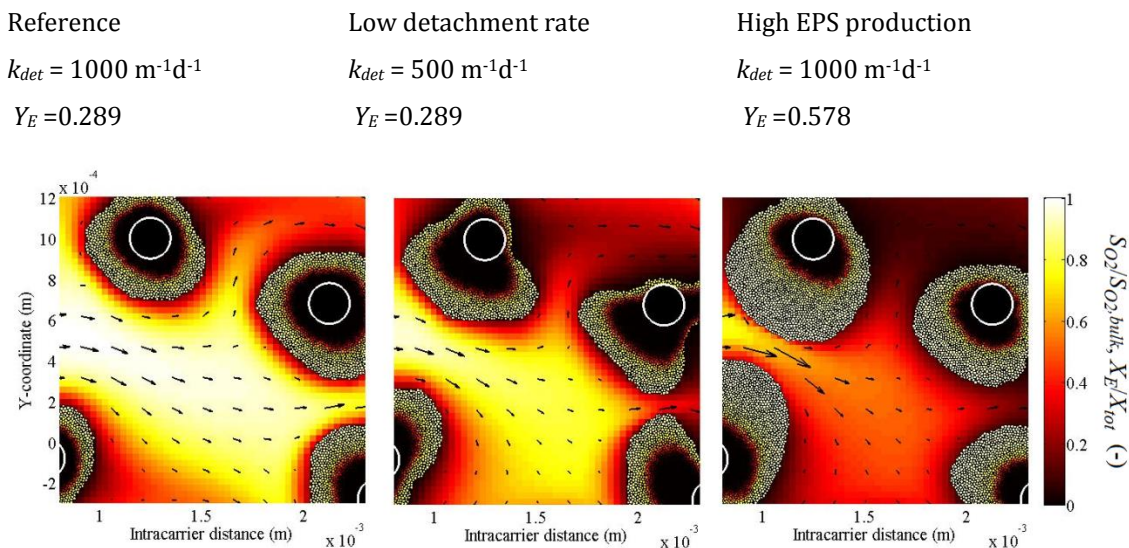


Figure 5.11. Close up of the simulation at day 40 for the reference case, low detachment case and a case with high EPS production.

5.4 Discussion

The results could explain various observations in found in previous experimental results: (I) permeability reduction by biofilm growth, (II) dependency of internal flow on reaction and (III) increase of reaction by increased shear stress. The effect of presence of biofilm on permeability can be seen with the reduction of permeability with time as the biofilm grow. The flow rate inside the sponge carrier

media was rate limiting on reaction which was observed by the simultaneous reduction of oxygen flux and permeability. This explains the peak of J_{O_2} followed by a reduction due to permeability loss. Increase of oxygen flux with increased reactor shear stress was shown by comparisons of curves (Figure 5.2a) and pictures (Figure 5.3) of with different k_{det} . Clearly, the detachment rate showed high sensitivity on the oxygen flux if the sponge were about to clog, whereas otherwise the sensitivity on k_{det} was moderate. It is theoretical possible that if k_{det} is high enough, beyond the range studied, or if the growth rate is slower, reaction might decrease with detachment rate due to bacterial washout.

Although only single species model of microorganisms was used, the sensitivity of Y_E and Y_B on reaction and clogging could explain why different biofilm formation occurs for nitrifying or IFAS processes (Morper and Linde 2005). This can be reproduced by incorporating a multispecies biofilm model into the framework. The sensitivity of EPS density on oxygen flux indicates that not only detachment but also compaction of biofilm, caused by carrier collisions, may affect the mass transfer. To obtain a set of reasonable coefficients, calibrations to experimental results are desirable. If utilization of nitrate is included, it is possible to calibrate the model by comparing denitrification of fluidized sponge and stagnant sponge as in the experiment of Deguchi and Kashiwaya (1994). To extend the model to give advice to operators, experimental work needs to be conducted to correlate the detachment coefficient k_{det} to microbial state variables (X_B , X_I and X_E) and actual operational data of aeration intensities and carrier volume fractions.

5.5 Conclusions

A novel model framework to simulate biofilm formation in sponge carrier media was developed. To account for the internal flow of water inside the sponge and the clogging effect of the biofilm a coupling between a Lattice Boltzmann hydrodynamics model and Individual based Modelling of biofilm was performed of a biofilm with oxygen as a limited substrate. Detachment caused by abrasion was modelled to decline exponentially with intracarrier distance due to damping effects of the sponge material. From the constructed model, the following typical responses were modelled:

- Growth of biofilm on the skeletal surface was limited on both diffusion and pore advection of the limited substrate.
- Presence of biofilm reduced the permeability of liquid flow which eventually reduced the reaction rate by clogging
- The degree of clogging varied with operational conditions simulated with varying degree of detachment coefficient and bulk oxygen concentrations. High simulated reactor shear resulted in a higher oxygen flux into the sponge and enabled biofilm to grow further inside.
- The degree of clogging was found to vary greatly with the properties of the biofilm with a large degree of sensitivity of the production and density of produced EPS.

6 MODELLING BIO-CLOGGING OF MULTISPECIES BIOFILMS IN SPONGE CARRIER MEDIA

6.1 Introduction

Sponge carrier media can upgrade existing Activated Sludge processes to create Integrated Fixed-film Activated Sludge (IFAS) processes (Morper, 1999). Upon such upgrade a 2-3 fold increase in biomass and a 1.6 fold increase in nitrification and denitrification rates can be obtained (Deguchi and Kashiwaya, 1994). The additional biomass is grown inside the sponge as a biofilm in the internal pores (Chae *et al.*, 2008), which is a layer of microorganisms adhered to a surface (substratum). In this biomass configuration, organisms are retained where substrates are abundant but reaction rates are lower than for the organisms in suspension due to diffusion resistance of the substrates (Wanner and Gujer, 1986).

Because of the porosities of the sponge carrier media, the biofilms behave differently from ordinary moving bed carrier media. Kinetic test have revealed that the biofilm reaction of a fluidized sponge is affected by the internal porous media flow inside (Matsui and Deguchi, 2002). Biofilm in porous media tends to grow in pore throats where substrates are more abundant which may result in clogging of the flow and reduced reaction rate (Rittmann, 1993).

Biofilm detachment is considered to be the main mechanism to control growth of biofilms (Rittmann *et al.*, 1992). It determines the steady state accumulation of biofilm thickness, biofilm Solids Retention Time (SRT) and hence also the composition of the microorganisms occupying the biofilm (Morgenroth and Wilderer, 2000). For the application of the sponge carrier media, increased biofilm detachment can reduce clogging by additional use of coarse air diffusers (Morper and Linde, 2005).

Several studies have shown that nitrification in IFAS increases with Hydraulic Retention Time (*HRT*) (Roshvanlo *et al.*, 2014, Sabzali *et al.*, 2011). This is because with *HRT*, *SRT* of Mixed Liquor Suspended Solids, SRT_{MLSS} , is affected as follows

$$SRT_{MLSS} = \frac{HRT}{1 - f_{rec}} \quad (6.1)$$

where, f_{rec} is the sludge recycle fraction. By increasing SRT_{MLSS} , the concentration of heterotrophs in the bulk liquid will increase. Unlike heterotrophs in the bulk liquid, heterotrophs inside the sponge experience diffusion limitation so they can be outcompeted by the heterotrophs in the bulk liquid at high SRT_{MLSS} . Nitrifiers benefits from this situation as more space is present for growth. With presence of denitrifying heterotrophs in deeper anoxic regions, Simultaneous Nitrification and Denitrification (SND) may occur (Morper and Linde, 2005). The optimum conditions for SND occurs if the amount of heterotrophs in anoxic parts are just enough to convert nitrate and nitrite without outcompeting nitrifying organisms for oxygen. According to experimental results (Roshvanlo *et al.*, 2014) there is an optimum optimized *HRT* and SRT_{MLSS} for this to occur, which maximized SND reaction.

The main reason for coexistence of an oxic an anoxic zone is the mass transfer of oxygen from the bulk liquid into the sponge. This means that in order to accurately solve for the SND inside the sponge, the mass transfer and the distribution of oxygen needs to be accurately modelled inside the sponge as well as inside the biofilm.

Lin (2010) modelled biofilm in sponge carrier media for COD removal with a 1-dimensional, single species biofilm model. Although the model could reproduce experimental results of COD removal to a satisfactory degree, some vital model

assumptions for mass transfer were missing. First of all, there was no implementation in the model that accounted for the effect of biofilm thickness on the degree of clogging and how it affected the mass transfer in the pores. Secondly, it didn't take into account the distribution of biofilm thicknesses with the depth into the sponge carrier media that has been observed in experimental results (Chae *et al.*, 2012).

So *et al.* (2014) constructed a 2-dimensional hydraulic model of sponge pore matrix and combined it with growth of biofilm. It was found that biofilm preferred to grow near pore throats where it blocked the flow and cause bio-clogging. With these types of models it was possible to detect the mechanisms of bio-clogging at the micro scale, however the required level of complexity makes it difficult to obtain quick insights and they have a high computational load in comparison to simpler 1-dimensional models of biofilm.

At present there is no simple model structure to accurately model mass transfer in sponge and SND reaction. Therefore, a new simple model was constructed that allowed a simple handling of biofilm computations and was able to perform the following

- Dynamically solve the effect of pore mass transfer on biofilm reaction and the stratification of biomass inside the sponge carrier media
- Implement a bio-clogging model that describe the reduction of advection inside the pores caused by biofilm blocking the flow

These points were met by the construction of a multi-compartment model where bio-clogging was triggered by a critical porosity. A monospecies model of heterotrophs was used to calibrate the critical porosity with experimental results. In order to extend the model to simulate SND inside the sponge carrier media, additional simulations were performed with a multispecies model including aerobic and denitrifying heterotrophs, Ammonia Oxidizing Organisms (AOO) and Nitrite Oxidizing Organisms (NOO). By varying f_{rec} the effect of sludge recycle on the competition between heterotrophs in bulk liquid and heterotrophs in sponge and the resulting effect on SND can be investigated.

6.2 Methods

6.2.1 Model compartments

The model system shown in Figure 6.1 consisted of a mixed reactor compartment, C_0 and $N = 4$ Biofilm Reactor Compartments, C_k , which resembled the subdivisions of equal volumes of the sponge carrier media and k was the compartment index towards depth into the sponge ($k=1, \dots, N$). The model simulated mass transport of soluble component S_i (g m^{-3}) and particulate components X_i (g m^{-3}) from C_0 through C_1 - C_N , where i was the component index. Boundaries with sponge compartments were modelled with a specific area A_k (m^{-1}) and flux $J_{i,k}$ ($\text{g m}^{-2} \text{d}^{-1}$). Reactions in the clarifier was neglected where a fraction (f_{rec}) of X_i were recycled back to mixed reactor and made it possible to switch from Moving Bed Biofilm Reactor (MBBR) mode (no sludge recycle) to IFAS (sludge recycle) configuration. AQUASIM 2.0 (Reichert, 1994) was chosen as a platform to build the model.

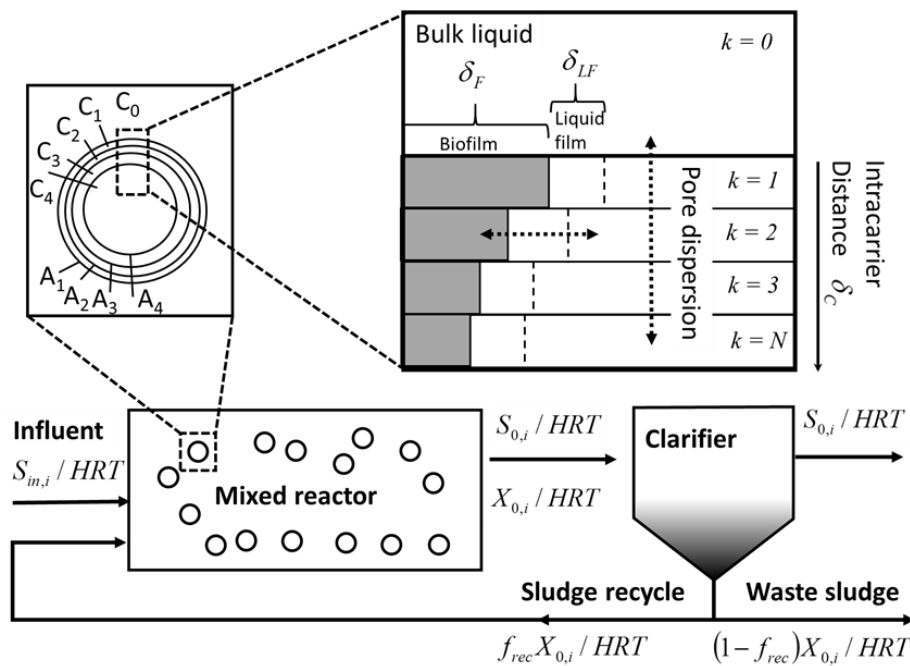


Figure 6.1. The modelled system consisting of a mixed reactor (C_0) connected with biofilm compartments of the sponge (C_1 - C_4) by diffusive boundaries.

6.2.2 Kinetic models

The reaction map, based on ASM1 (Henze *et al.*, 2000) with modified two-step nitrification and denitrification processes (Kaelin *et al.*, 2009) is shown as a Petersen matrix in Appendix 4. It included 10 state variables (i) and 9 processes (j) with standardized notations (Corominas *et al.*, 2010). The soluble components were: soluble substrate (S_B), dissolved oxygen (S_{O_2}), ammonium plus ammonia nitrogen (S_{NHX}), nitrate nitrogen (S_{NO_3}) and nitrite nitrogen (S_{NO_2}). The particulate components consisted of ordinary heterotrophic organisms (X_{OHO}), AOO (X_{AOO}), NOO (X_{NOO}), slowly biodegradable substrates (X_{CB}) and particulate undegradable organics (X_U). X_{OHO} were fast-growers and were dependent of presence of S_B for growth and had the ability to switch electron acceptors from S_{O_2} in oxic conditions to S_{NO_2} and S_{NO_3} in anoxic conditions. The latter processes are called two-step denitrification where S_{NO_3} was converted to dinitrogen gas via S_{NO_2} . X_{AOO} were slow-growers that converted S_{NHX} to S_{NO_2} which was the initial step in nitrification. Nitrification was completed by X_{NOO} that converted S_{NO_2} to S_{NO_3} . The parameters used in the simulations are shown in Table A.4 in Appendix 4. The reaction rates, r_i (g d⁻¹) was obtained by summation of the products of stoichiometric coefficients v_{ij} (-) and the process rates ρ_j (g d⁻¹).

6.2.3 Modelling pore dispersion in a clogging sponge

The pore water flux within pores, $J_{i,k}$ depend on both pore diffusion and pore advection and was modelled as an apparent diffusive flux as follows

$$J_{i,k} = A_k D_{app} (S_{i,k-1} - S_{i,k}), \quad 1 \leq k \leq N \quad (6.2)$$

where A_k is the specific interfacial area between compartments, D_{app} (m² d⁻¹) was the apparent diffusion coefficient resulted from the combined effect of advection and molecular diffusion.

The use of D_{app} has been applied in the past for the calculation of reaction in porous catalytic pellets (Rodrigues *et al.*, 1982). Similar to Rodrigues *et al.* (1982) an augmentation factor $f(-)$ was applied but with an upper limit, $f_0 (-)$ as follows

$$D_{app} = (1 + f) \cdot D, \quad 0 \leq f \leq f_0 \quad (6.3)$$

where D ($\text{m}^2 \text{d}^{-1}$) was the overall molecular diffusion coefficient. In this work, f_0 (-) was the initial augmentation of diffusion in case of no biofilm and was defined from the interstitial velocity of an empty sponge U_{ini} as follows

$$f_0 = \frac{U_{ini}}{A_k D} \quad (6.4)$$

Details on how to calculate U_{ini} can be found in Appendix 4.

A new model of f is presented here which models bio-clogging as switching between diffusion and advection as follows

$$f = f_0 \left(\frac{\varepsilon_h - \varepsilon_{crit}}{\varepsilon_{ini} - \varepsilon_{crit}} \right)^3 \quad (6.5)$$

where ε_h (-) was the hydraulic porosity of the pore water, excluding porosities within the biofilm and ε_{ini} (-) was the empty sponge porosity. ε_{crit} (-) was the critical value of ε_h for which biofilm clog the throats of the pores and mass transfer proceeds by diffusion. The power factor of 3 was derived from Kozeny–Carman equation (Bear, 1988) as shown in equations (A.4-A.6) in Appendix 4. Because, clogging of flow depends mostly on the “choking point” where the intersection of flow was the thinnest, ε_h was calculated from the compartment with maximum biofilm thickness, δ_F , as follows

$$\varepsilon_h = \varepsilon_{ini} - a_b \cdot \max(\delta_{F,k}) \quad (6.6)$$

where a_b (m^{-1}) was the specific surface area of biofilm per carrier volume.

In AQUASIM, the pore mass transfer was implemented by connecting the different compartments with links with an exchange coefficient, q_{ex} ($\text{m}^3 \text{d}^{-1}$) given by

$$q_{ex} = D_{app} A_k^2 V_k \quad (6.7)$$

where V_k (m^3) is the compartment volume.

6.2.4 Modelling biofilm growth and biofilm thickness

The mass balance of particulate components X_i inside the biofilm (b superscript) were modelled as a balance between reaction (including growth and decay) and internal advection as follows

$$\frac{dX_{i,F}}{dt} = r_{i,F} - u_{X,F} \frac{dX_{i,F}}{dz} \quad (6.8)$$

where subscript F refers to inner biofilm and $u_{X,F}$ was the local advection velocity of particulate components in the biofilm normal to the substratum. Biofilm thickness was solved dynamically by a balance of the surface growth velocity $u_{X,LF}$ and the detachment erosion velocity u_{det} as follows

$$\frac{d\delta_{BF}}{dt} = u_{X,LF} - u_{det} \quad (6.9)$$

$$u_{det} = k_{det} \delta_F^2 e^{-c\delta_c/r} \quad (6.10)$$

where subscript LF was liquid-biofilm interface, k_{det} was a proportionality constant, c (-) the exponential reduction coefficient, δ_c was the intracarrier distance and r was the sponge radius. The exponential term was added to the expression of Stewart (1993) to add the effect of damping of forces caused by of carrier collisions (So *et al.*, 2014).

6.2.5 Modelling components in bulk liquid and clarifier

The mass balance of the soluble components in the bulk liquid was given as follows

$$\frac{dS_{i,0}}{dt} = r_{i,0} - \Phi_S A_S J_{i,1} + \frac{S_{i,in} - S_{i,0}}{HRT} \quad (6.11)$$

where Φ_S (-) was the volumetric fraction of sponges in the reactor and $S_{i,in}$ (g m^{-3}) was the influent concentration. S_{O_2} in C_0 was kept fixed at 2 g m^{-3} . Particulate components in the bulk liquid included reaction, recycle from clarifier and detachment as follows

$$\frac{dX_{i,0}}{dt} = r_{i,0} - (1 - f_{rec}) \frac{X_{i,0}}{HRT} + \frac{\Phi_S a_b}{N} \sum_{k=1}^N X_{i,k,LF} u_{det,k} \quad (6.12)$$

where f_{rec} was the recycle fraction from the clarifier. The last term was the total rate of biofilm detachment from the biofilm compartments.

6.2.6 Simulation plan

The simulations were performed in two steps: (i) monospecies denitrification model for calibration and (ii) extension to multispecies biofilm to model simultaneous nitrification and denitrification in MBBR and IFAS configuration.

In the monospecies denitrification model, only processes 2,3,4 and 9 in Table A.3 were active in order to calibrate the sponge surface nitrate flux, J_{1,NO_3} to experimental results of Matsui and Deguchi (2002) performed on denitrifying sponges with nitrate as a limiting substrate with surface loading rate of $3.5 \text{ g N m}^{-3} \text{ d}^{-1}$ and volumetric loading rate of $163 \text{ g m}^{-3} \text{ d}^{-1}$. The parameters k_{det} in equation (6.10) and ϵ_{crit} in equation (6.5) were used to fit an experimental curve of nitrate flux. A sensitivity analysis was performed to estimate the sensitivity of parameters on the effluent nitrate concentrations.

In the multispecies biofilm simulation, the entire reaction map in Table A.3 was used. S_{O_2} in bulk was controlled as a constant value of 2 g m^{-3} . Influent consisted of ammonia and substrate with CN-ratio of 10, surface loading rate $0.86 \text{ g N m}^{-3} \text{ d}^{-1}$ and volumetric loading rate of $80 \text{ g m}^{-3} \text{ d}^{-1}$. Different recycle ratio of biomass was used to control the biomass in bulk liquid as in equation (6.12). This was carried out in order to investigate the competition of X_{OHO} in bulk with X_{OHO} inside sponge and how it affects the degree of simultaneous nitrification and denitrification.

6.3 Results

6.3.1 Model calibration and sensitivity analysis of the monospecies model

Figure 6.2 shows the results of the calibration with the dataset from Matsui and Deguchi (2002). $k_{det} = 1000 \text{ m}^{-1} \text{ d}^{-1}$ was calibrated to fit the nitrate flux in the limit of very high nitrate concentrations. $\epsilon_{crit} = 0.28$ was calibrated in the low to intermediate ranges of nitrate concentrations. Results of the linear regression coefficients obtained from the sensitivity analysis for the monospecies model are shown in Figure 6.3. These were obtained by a routine in AQUASIM that measures the relative change of an output variable (S_{NO_3}) versus the relative change of input parameter (Reichert, 1994). Apart from the high sensitivity of the calibrated parameters ϵ_{crit} and k_{det} , a high sensitivity of $Y_{OHO,NOX}$ and $X_{F,tot}$ was present. Because

the analysis was focused solely on the derivate change of output variable in respect to input variables, it didn't take into account that some input parameter has smaller or larger ranges of values. The ranges of values of $Y_{OHO,NOX}$ is not very large whereas values of k_{det} may differ up to 2 orders of magnitude in different shear conditions (Xavier *et al.*, 2005b). For $X_{F,tot}$ however, there was both a large sensitivity and a wide range of possible values.

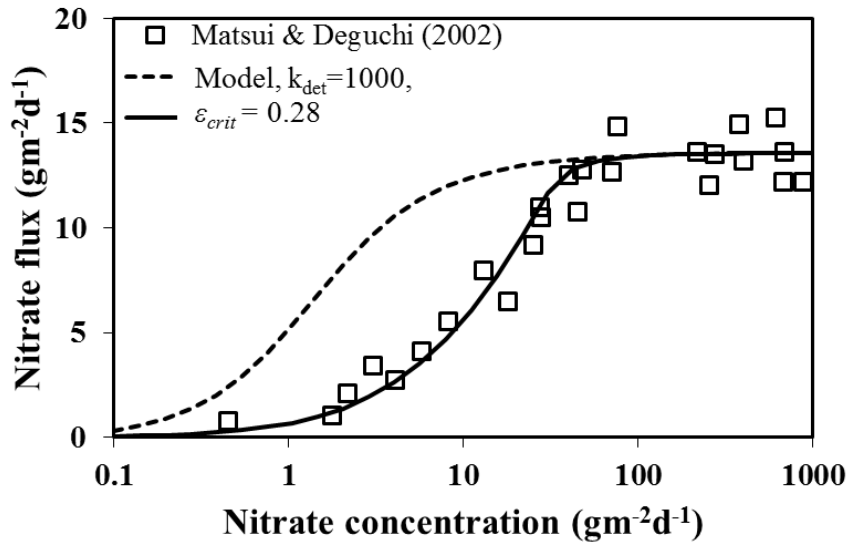


Figure 6.2. Calibration of the mass transfer parameters k_{det} and ϵ_{crit} to experimental results of Matsui and Deguchi (2002).

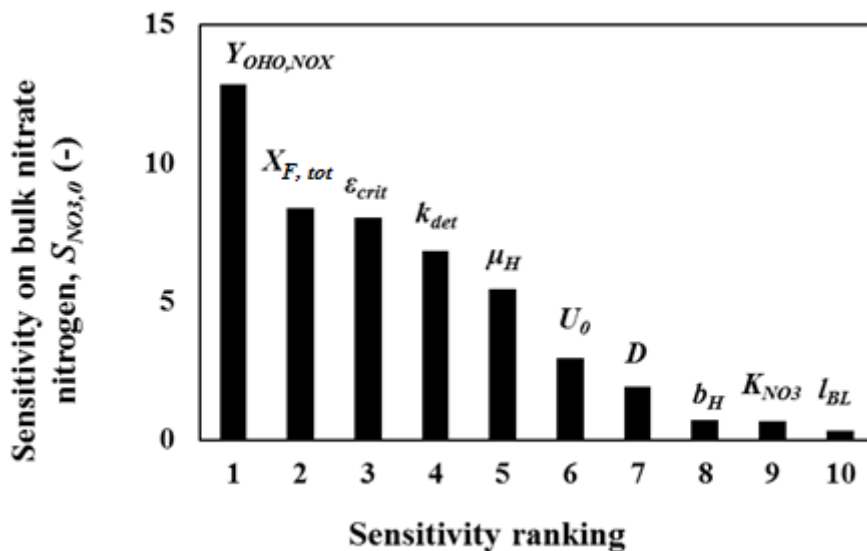


Figure 6.3. Linear regression coefficients from sensitivity analysis of the parameters in the monospecies denitrification model.

6.3.2 Extension to multispecies model in IFAS configuration

6.3.2.1 Soluble components

The bulk concentrations of soluble components from the multispecies model are plotted with f_{rec} in Figure 6.4. A decline with f_{rec} for influent substrates $S_{B,0}$ and $S_{NHX,0}$ could be seen which indicate an increase of overall activity of X_{OHO} and X_{A00} with f_{rec} . The trends for other substrates $S_{NO2,0}$ and $S_{NO3,0}$ were more complex. $S_{NO2,0}$ started to appear at $f_{rec} = 0.4$ and increased with f_{rec} until a peak value at $f_{rec} = 0.7$, followed by a decrease. $S_{NO3,0}$ started to appear at $f_{rec} = 0.65$, followed by an increase with f_{rec} . According to the model results, there exist an optimum $f_{rec} = 0.6$ for maximized SND, which resulted in minimum effluent of total nitrogen ($S_{NHX,0}+S_{NO3,0}+S_{NO2,0}$) in bulk liquid of 4.7 gN/m³. This is in agreement with Roshvanlo *et al.* (2014) of an optimum SRT_{MLSS} for SND.

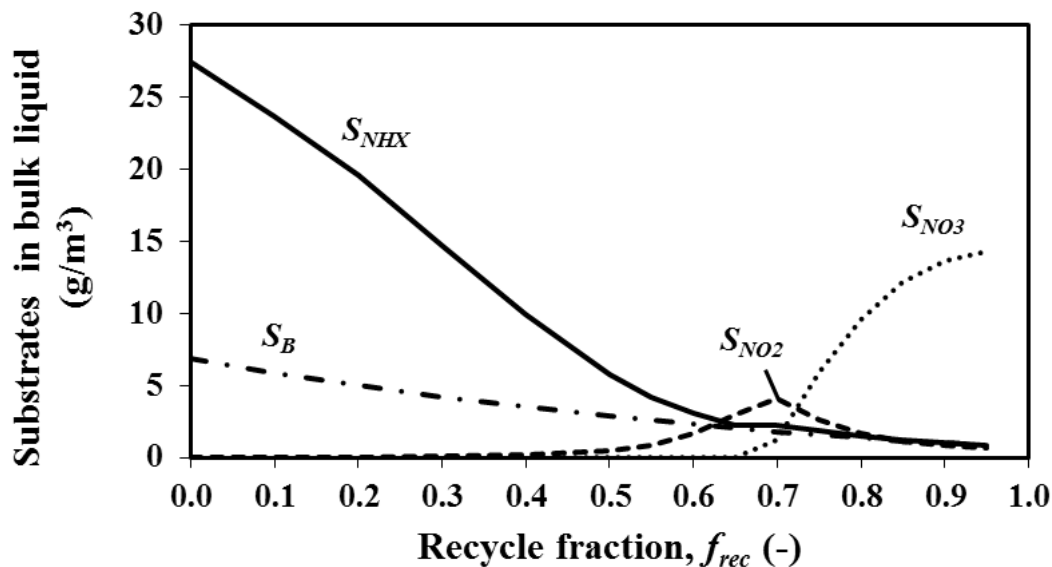


Figure 6.4. Soluble components in bulk liquid plotted with f_{rec} .

Distribution of dissolved oxygen inside the sponge at $f_{rec} = 0$ is shown in Figure 6.5. The levels of dissolved oxygen are low (0.07-0.028) and increase with the distance from the substratum. The dashed line indicates the biofilm thickness which was highest in the sponge surface compartment C_1 and lowest in the internal compartment C_4 . Figure 6.6 show the variation of oxygen distribution with f_{rec} . At low values of f_{rec} the dissolved oxygen levels inside the sponge was low. With higher f_{rec} the oxygen levels inside the sponge increases which is related to the increase of mass transfer that will be explained in Discussion.

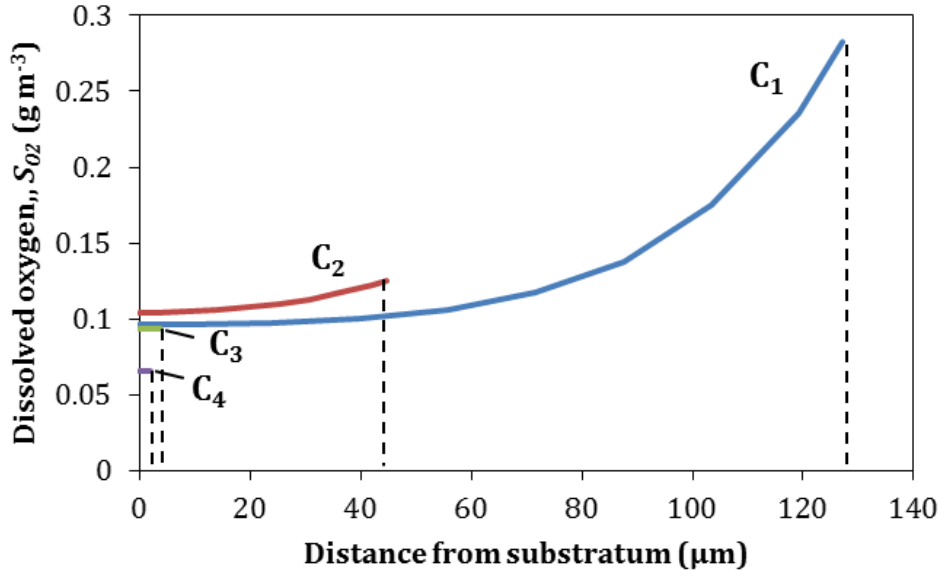


Figure 6.5. Oxygen distribution in biofilm for the different compartments.

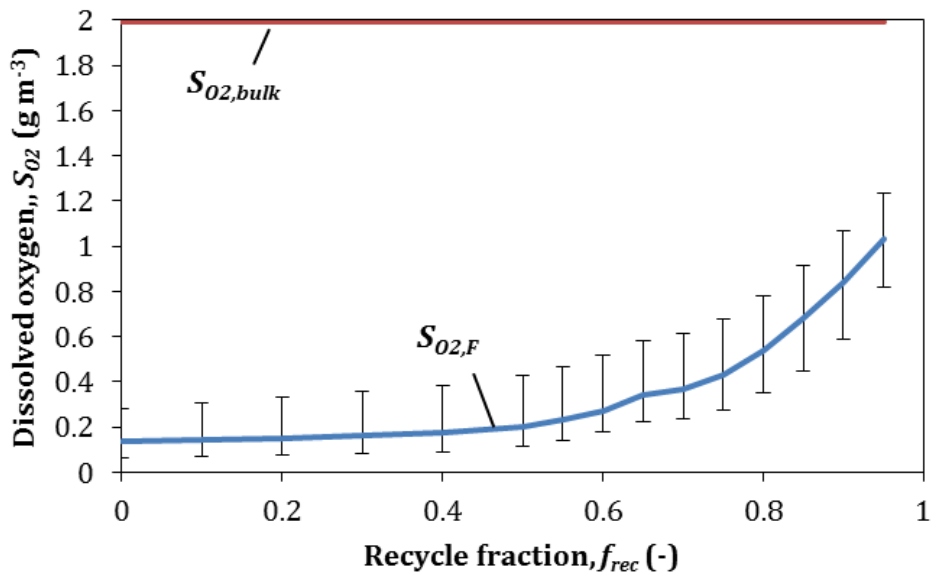


Figure 6.6. Variation of dissolved oxygen concentrations with f_{rec} .

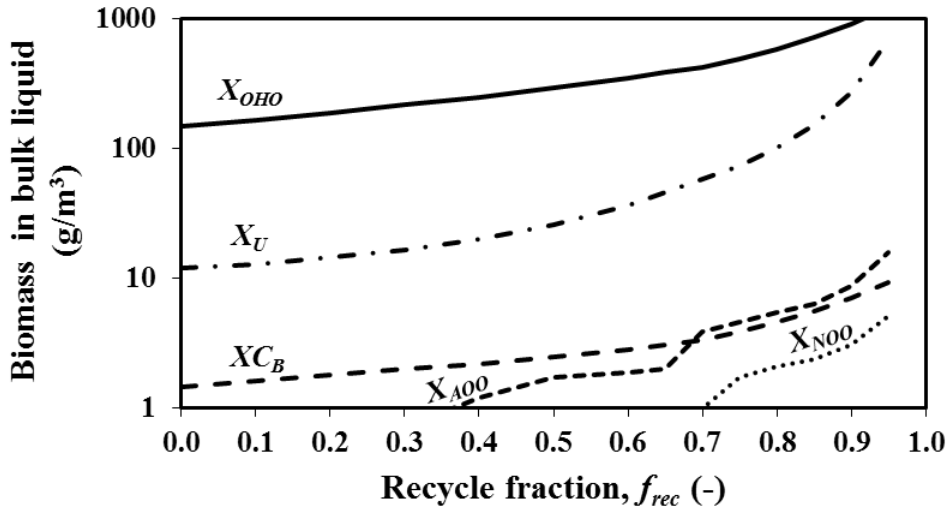


Figure 6.7. Particulate components in bulk liquid plotted with f_{rec} .

6.3.2.2 Particulate components

Curves of bulk liquid particular components are shown in Figure 6.5. The active biomass in bulk liquid was dominated by $X_{OHO,0}$ having concentrations of two orders of magnitude larger than other active biomass components (X_{AOO} and X_{NOO}). This is in agreement with experiments of Omnis-Hayden *et al.* (2007) that operated an IFAS reactor with SRT_{MLSS} of 4 days. As expected, all particular components in bulk liquid increased with f_{rec} .

The distribution of biomass within the sponge carrier media for different values of f_{rec} is shown in Figure 6.6. Distribution within the biofilm in each compartment C_k is plotted as an area graph of particulate components $X_{i,F}$ with the distance from the substratum z . For all values of f_{rec} the biomass thickness decreased from the surface compartment C_1 to the inner compartments C_2 - C_4 . The biofilm thicknesses and the reduction with depth are in agreement with experimental results of (Chae *et al.*, 2008, 2012, Morper and Linde, 2005). Another general trend was that the fraction of particulate undegradable organics in biofilm $X_{U,F}$ increased towards the substratum and towards C_4 .

There were large differences in the distribution of active biomass ($X_{OHO,F}$, $X_{AOO,F}$ and $X_{NOO,F}$) for different f_{rec} . As opposed to $X_{OHO,0}$ in bulk liquid, the amount of X_{OHO} inside the sponge decreased with f_{rec} which will be explained in Discussion.

At $f_{rec} = 0.6$, AOO biomass appears as one of the major species in C₁ and C₂. With only presence of X_{OHO} and X_{AOO} , SND reaction proceeded as a short cut SND via S_{NO2} , where X_{AOO} converted S_{NHX} to S_{NO2} and X_{OHO} converted S_{NO2} to dinitrogen gas.

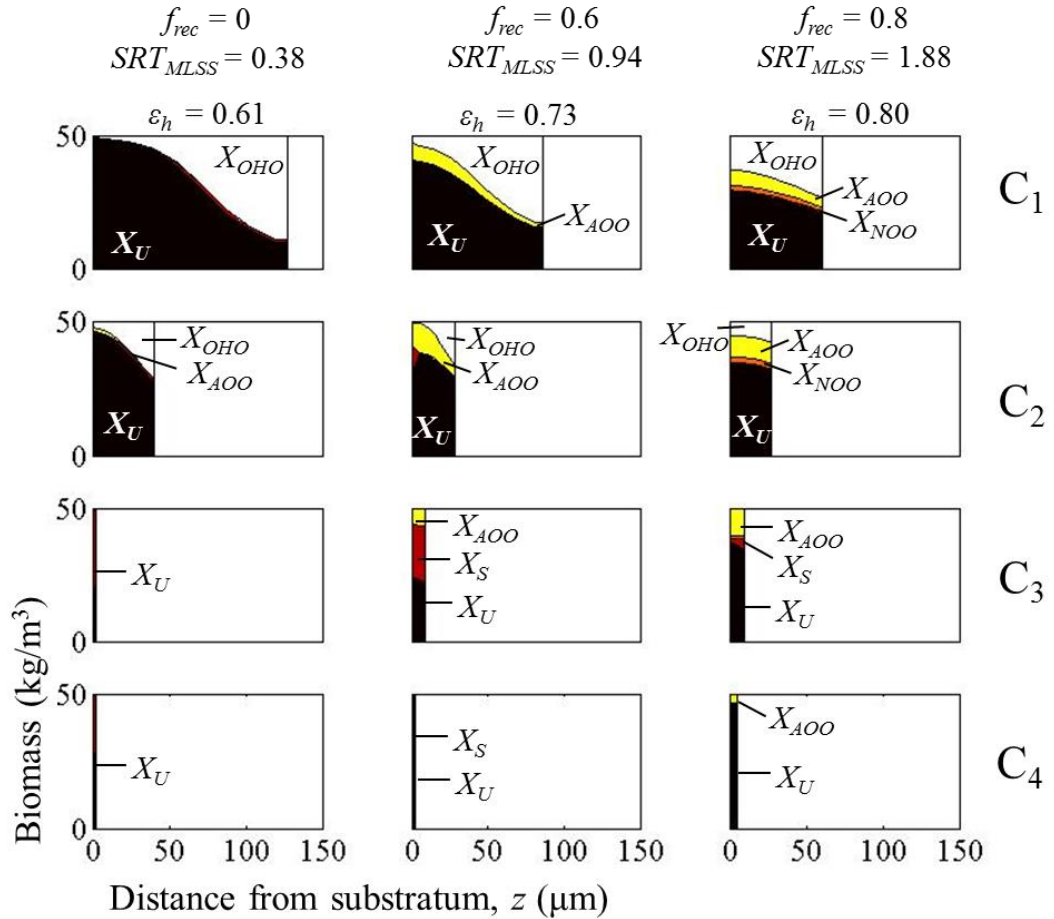


Figure 6.8. Variation of particulate components with f_{rec} and within the biofilm grown in different compartments (C₁-C₄) in the sponge carrier media.

At $f_{rec} = 0.8$, the levels of S_{O2} inside sponge carrier media became high enough to enable NOO to survive inside the sponge carrier media. Growth of NOO is limited near the surface of the sponge which is in agreement with experiments of Omnis-Hayden *et al.* (2007). With presence of NOO, a different sort of SND occurred where X_{NOO} converted S_{NO2} to S_{NO3} and X_{OHO} converted S_{NO3} to dinitrogen gas via S_{NO2} . However, because less X_{OHO} existed in the anoxic regions inside the sponge, denitrification became limited which explained the accumulation of S_{NO3} at higher f_{rec} observed in Figure 6.5.

6.4 Discussion

The trends for X_{OHO} in bulk liquid were completely different with those inside the sponge. The amount of X_{OHO} in bulk liquid increased with f_{rec} because of the increase of the SRT_{MLSS} which enable more X_{OHO} to grow before being washed out. On the other hand, X_{OHO} inside the sponge decrease with f_{rec} . This was because, unlike X_{OHO} in bulk liquid, X_{OHO} inside the sponge experience diffusion limitation on oxygen and substrates which gave competitive advantage for X_{OHO} to grow in bulk when the sludge retention time in the bulk liquid becomes sufficiently high. At $f_{rec} = 0$ the active biomass inside the sponge was dominated by X_{OHO} with only limited growth of X_{AOO} . Because of the dominance of X_{OHO} inside the sponge carrier media, it was not possible for slow growing X_{AOO} and X_{NOO} to survive due to the short sludge retention time. Moreover, $\varepsilon_h = 0.61$ was small which limited the advection of oxygen to be utilized by X_{AOO} and X_{NOO} .

Higher f_{rec} resulted in less X_{OHO} inside the sponge which gave three distinct advantages to the slow growing nitrifiers: (i) more oxygen available due to reduced aerobic growth of X_{OHO} (ii) higher mass transfer of oxygen due to less clogging (larger ε_h) and (iii) lower local SRT within the biofilm.

The model developed were able to simulate bio-clogging effects in sponge carrier media that was previously only possible in the multidimensional models (So *et al.*, 2014). This was performed by the assumption of a critical porosity for which clogging occur. The mass transfer model could be calibrated with experimental results of denitrifying sponges. With multispecies extension the model framework could simulate SND inside the sponge carrier media. The trends of biomass species inside the sponge as well as in bulk liquid was in good agreement with previous experimental results. The results identified f_{rec} as a possible control variable to maximize SND reaction of sponge carrier media which was theoretically explained by the competition of heterotrophs in the bulk with the heterotrophs inside the sponge carrier media.

6.5 Conclusions

This paper describes a novel and simple approach to simulate multispecies biofilm and bio-clogging inside sponge carrier media. By utilizing multiple biofilm reactor

compartments connected by diffusive boundaries, the dual mass transfer processes inside the pore matrix as well as inside the biofilm of the sponge could be simulated.

Bio-clogging inside the sponge carrier media could be modelled by a novel model approach of the pore diffusivity. It was based on the assumption that there exists a critical porosity below which no internal flow of water was possible and the mass transfer proceeds by diffusion. A good agreement with experimental results could be obtained with calibration of this parameter. In the future work, further validation of the model was necessary to simulate the effect of clogging under a wider range of operational conditions and with addition of EPS.

The potential of this model structure was demonstrated by application into multispecies model of heterotrophs, AOO and NOO. At low sludge recycle rate from the clarifier, the heterotrophs were abundant inside the sponge were they outcompete the slower growing AOO and NOO. At higher recycle rates, the concentrations of heterotrophs in the bulk increased drastically which outcompeted heterotrophs inside the sponge that were under pressure of substrate mass transfer limitation. This enabled the growth of AOO and NOO inside the sponge carrier media and subsequent SND reaction could proceed.

7 CONCLUSIONS

This dissertation demonstrates multiscale frameworks for biofilm in sponge carrier media. Multiscale modelling provides a valuable insight of the mass transfer mechanisms inside the sponge carrier media and novel frameworks for analysis and modelling of the sponge carrier media.

7.1 Principal findings

Chapter 3 investigated the reactor-sponge interface and studied how outside flow conditions affected internal reaction rate by intraparticle forced convection. This study was performed by a simulation of CFD-DEM where air bubbles and sponges were simulated as particles inside a reactor with wastewater. To the authors best knowledge this is the first CFD-DEM simulation of MBBR or IFAS systems to be performed. The intraparticle forced convection and reaction inside the sponge carrier media was governed by the sponge size and aeration intensity with only minimal effect of aeration configuration. Intraparticle forced convection affected reaction rate only when the flow region changed. Under conventional operation condition, the aeration intensity only marginally affected the reaction rate. For the determination of intraparticle forced convection a balance between buoyancy and drag forces can be assumed.

Chapter 4 handled the organism-biofilm interface and focused on generation of morphology of microorganisms, and how biofilm morphology is related to biofilm detachment. Biofilm growth was simulated by individual based modelling where

individual cells were simulated as particles undergoing dynamic growth, division and decay. Local biofilm detachment varied along the surface as the peak of the biofilm surface received higher shear stress than biofilm at depressions. Higher bulk shear stress caused smoother biofilms and a variable shear stress caused the biofilm to be more susceptible to detachment.

Chapter 5 studied how biofilm clog sponge carrier media. A novel framework that coupled IbM with LB hydrodynamic and mass transfer model was constructed. Simplifications of intraparticle forced convection and detachment was implemented from generalizations in Chapter 3 and 4. From the results, initially biofilm grew homogeneously at the sponge surface after which a discontinuous growth of biofilm occurred. Shear stress caused higher biofilm detachment near the surface which suppressed bio-clogging inside the sponge. Clogging was more severe during elevated oxygen concentrations in bulk liquid.

Chapter 6 studied how sludge recycle effect simultaneous nitrification and denitrification inside the sponge carrier media. Higher sludge recycle had a positive effect on autotrophic growth and nitrification. Higher sludge recycle caused more heterotrophs in bulk liquid which outcompeted the heterotrophs inside the sponge carrier media. This enabled the autotrophs to grow in a lower competitive environment inside the sponge. A sludge recycle of 0.6 gave the best conditions for SND reaction for which a short-cut SND progressed without activation of NOO.

7.2 The dual characteristics of sponge as a moving bed and porous media

Even though sponge carrier media is composed of porous media, previous modelling studies only considered the carrier media aspect. When porous media models are integrated for the simulation of biofilm growth, a more realistic biofilm development is simulated. The modelling results presented in the studies showed good agreement with experimental results and similarities could be observed with biofilms in other porous media systems:

- Modelling work in chapter 5-6 found that the biofilm in sponge carrier media has a large impact on permeability and the resulting mass transfer.

This is similar to biofilms in other porous media systems (Cunningham *et al.*, 1991).

- The modelling study in chapter 5 strengthened the view of Morper and Linde (2005) that biofilm clog the internal pore of the sponge in the absence of sufficient shear stress. This is similar to what occurs for biofilms in soils (Rittmann, 1993).
- When the simulated shear stress was low, the results of chapter 5-6 show a decline of biofilm thickness with depth. This is similar to experimental results of sponge (Chae *et al.*, 2012) and experimental results of sand columns (Vayenas *et al.*, 2002).
- The modelling in Chapter 5 show the distinct stages of development of biofilm of initial homogeneous biofilm followed by a heterogeneous structure that eventually clog the internal flow. Similar development with time has been observed in sand column experiments (Paulsen *et al.*, 1997)

The main difference between biofilm in sponge carrier media and biofilm in soils is the mechanism of biofilm detachment which in sponge carrier media is governed by abrasion, i.e. collisions of sponge carrier media in the reactor. This was studied in Chapter 5 where the empirical detachment velocity was modelled to decline exponentially with intracarrier distance. If the shear stress was high on the surface region, a thinner biofilm could be developed near the surface region.

7.3 Future work

The modelling framework involved simulations of mechanisms enough for the understanding of the mechanisms of bio-clogging in sponge carrier media. Some minor modification of the model structure can be done to expand the modelling by adding more components into the simulation.

One possibility would be to implement biofilm permeability. This is possible by adjusting an apparent viscosity in the lattice Boltzmann equation that was done by works of Kapellos *et al.* (2007b). In this way, flow inside the biofilm can be simulated which may affect mass transfer and bio-clogging.

Another possible implementation is to construct a function that describes biofilm cohesion as a function of the availability of EPS. With a mechanistic model of

detachment, the effect of production and availability of EPS on resulting biofilm formation can be studied. For example organisms which produce a lot of EPS may form a strong biofilm that is resistant to shear and will remain even under high shear conditions. Another characteristic of EPS is the large volume it occupies in relation to its COD contents which will lead to more severe clogging with higher production and occupancy of Extracellular Polymeric Substances (EPS).

8 REFERENCES

- Ahimou, F.; Semmens, M. J.; Haugstad, G.; Novak, P. J. (2007) Effect of Protein, Polysaccharide, and Oxygen Concentration Profiles on Biofilm Cohesiveness. *Appl. Environ. Microbiol.*, **73** (9), 2905–2910.
- Allison, D. G.; Ruiz, B.; Sanjose, C.; Jaspe, A.; Gilbert, P. (1998) Extracellular products as mediators of the formation and detachment of *Pseudomonas fluorescens* biofilms. *FEMS Microbiol. Lett.*, **167** (2), 179–184.
- Alpkvist, E.; Klapper, I. (2007) Description of mechanical response including detachment using a novel particle model of biofilm/flow interaction. *Water Sci. Technol.*, **55** (8-9), 265–273.
- Alpkvist, E.; Picioreanu, C.; Loosdrecht, M. van; Heyden, A. (2006) Three-dimensional biofilm model with individual cells and continuum EPS matrix. *Biotechnol. Bioeng.*, **94** (5), 961–979.
- Anderson, J. (1995) *Computational Fluid Dynamics*, 1 edition.; New York: McGraw-Hill Science/Engineering/Math.

- Ardern, E.; Lockett, W. T. (1914) Experiments on the oxidation of sewage without the aid of filters. *J. Soc. Chem. Ind.*, **33** (10), 523–539.
- Bae, H.; Yang, H.; Chung, Y.-C.; Yoo, Y. J.; Lee, S. (2014) High-rate partial nitrification using porous poly(vinyl alcohol) sponge. *Bioprocess Biosyst. Eng.*, **37** (6), 1115–1125.
- Bakke, R. (1986) *Biofilm detachment*; Montana State University.
- Bakke, R.; Trulear, M. G.; Robinson, J. A.; Characklis, W. G. (1984) Activity of *Pseudomonas aeruginosa* in biofilms: Steady state. *Biotechnol. Bioeng.*, **26** (12), 1418–1424.
- Banin, E.; Vasil, M. L.; Greenberg, E. P. (2005) Iron and *Pseudomonas aeruginosa* biofilm formation. *Proc. Natl. Acad. Sci. U. S. A.*, **102** (31), 11076–11081.
- Bardy, S. L.; Ng, S. Y. M.; Jarrell, K. F. (2003) Prokaryotic motility structures. *Microbiology*, **149** (2), 295–304.
- Bear, J. (1988) *Dynamics of Fluids in Porous Media*, Trade Paperback Edition edition.; New York: Dover Publications.
- Benidickson, J. (2011) *The culture of flushing: a social and legal history of sewage*; UBC Press.
- Bishop, P. L.; Rittmann, B. B. (1995) Modelling heterogeneity in biofilms: Report of the discussion session. *Water Sci. Technol.*, **32** (8), 263–265.
- Boles, B. R.; Horswill, A. R. (2008) agr-mediated dispersal of *Staphylococcus aureus* biofilms. *PLoS Pathog.*, **4** (4).

- Bottero, S.; Storck, T.; Heimovaara, T. J.; Loosdrecht, M. C. M. van; Enzien, M. V.; Piciooreanu, C. (2013) Biofilm development and the dynamics of preferential flow paths in porous media. *Biofouling*, **29** (9), 1069–1086.
- Boyd, A.; Chakrabarty, A. M. (1995) *Pseudomonas aeruginosa* biofilms: Role of the alginate exopolysaccharide. *J. Ind. Microbiol.*, **15** (3), 162–168.
- Bryers, J. D. (1988) Modeling biofilm accumulation. *Physiol. Models Microbiol.*, **2**, 109–144.
- Chae, K.-J.; Kim, S.-M.; Oh, S.-E.; Ren, X.; Lee, J.; Kim, I. S. (2012) Spatial distribution and viability of nitrifying, denitrifying and ANAMMOX bacteria in biofilms of sponge media retrieved from a full-scale biological nutrient removal plant. *Bioprocess Biosyst. Eng.*, **35** (7), 1157–1165.
- Chae, K.-J.; Rameshwar, T.; Jang, A.; Kim, S. H.; Kim, I. S. (2008) Analysis of the nitrifying bacterial community in BioCube sponge media using fluorescent in situ hybridization (FISH) and microelectrodes. *J. Environ. Manage.*, **88** (4), 1426–1435.
- Characklis, W. G.; Bouwer, E.; Gujer, W.; Hermanowicz, S.; Wanner, O.; Watanabe, Y.; Wilderer, P. (1989) Modelling of Biofilm Systems. *IAWPRC Task Group Rep.*
- Chen, X.; Stewart, P. S. (2002) Role of electrostatic interactions in cohesion of bacterial biofilms. *Appl. Microbiol. Biotechnol.*, **59** (6), 718–720.
- Choi, Y. C.; Morgenroth, E. (2003) Monitoring biofilm detachment under dynamic changes in shear stress using laser-based particle size analysis and mass

fractionation. *Water Sci. Technol. J. Int. Assoc. Water Pollut. Res.*, **47** (5), 69–76.

Churchill, S. W.; Bernstein, M. (1977) Correlating Equation for Forced Convection from Gases and Liquids to a Circular Cylinder in Crossflow. *J. Heat Transf.*, **99 Ser C** (2), 300–306.

Ciudad, G.; Werner, A.; Bornhardt, C.; Muñoz, C.; Antileo, C. (2006) Differential kinetics of ammonia- and nitrite-oxidizing bacteria: A simple kinetic study based on oxygen affinity and proton release during nitrification. *Process Biochem.*, **41** (8), 1764–1772.

Clarkson, K. L. (1983) Fast algorithms for the all nearest neighbors problem. *2013 IEEE 54th Annu. Symp. Found. Comput. Sci.*, 226–232; IEEE.

Clement, T. P.; Hooker, B. S.; Skeen, R. S. (1996) Macroscopic models for predicting changes in saturated porous media properties caused by microbial growth. *Groundwater*, **34** (5), 934–942.

Conn, H. J. (1932) The Cholodny technic for the microscopic study of the soil microflora. *Zentr Bakt Parasitenk Abt II*, **87**, 233–239.

Corominas, L.; Rieger, L.; Takács, I.; Ekama, G.; Hauduc, H.; Vanrolleghem, P. A.; Oehmen, A.; et al. (2010) New framework for standardized notation in wastewater treatment modelling. *Water Sci. Technol.*, **61** (4), 841–857.

Costerton, J. W.; Geesey, G. G.; Cheng, K. J. (1978) How bacteria stick. *Sci. Am.*, **238** (1), 86–95.

- Coufort, C.; Derlon, N.; Ochoa-Chaves, J.; Liné, A.; Paul, E. (2007) Cohesion and detachment in biofilm systems for different electron acceptor and donors. *Water Sci. Technol.*, **55** (8-9), 421–428.
- Crowe, C. T.; Schwarzkopf, J. D.; Sommerfeld, M.; Tsuji, Y. (1997) *Multiphase Flows with Droplets and Particles*; CRC Press.
- Cunningham, A. B.; Characklis, W. G.; Abedeen, F.; Crawford, D. (1991) Influence of biofilm accumulation on porous media hydrodynamics. *Environ. Sci. Technol.*, **25** (7), 1305–1311.
- Davit, Y.; Iltis, G.; Debenest, G.; Veran-Tissoires, S.; Wildenschild, D.; Gerino, M.; Quintard, M. (2011) Imaging biofilm in porous media using X-ray computed microtomography. *J. Microsc.*, **242** (1), 15–25.
- Deguchi, H.; Kashiwaya, M. (1994) Study on nitrified liquor recycling process operations using polyurethane foam sponge cubes as a biomass support medium. *Water Sci. Technol.*, **30** (6 pt 6), 143–149.
- Domozych, D. S. (2007) Exopolymer Production by the Green Alga *Penium Margaritaceum*: Implications for Biofilm Residency. *Int. J. Plant Sci.*, **168** (6), 763–774.
- Duan, D. L.; Zhang, R. L.; Ding, X. J.; Li, S. (2006) Calculation of specific surface area of foam metals using dodecahedron model. *Mater. Sci. Technol.*, **22** (11), 1364–1368.
- Dunne, J. W. M. (2002) Bacterial adhesion: Seen any good biofilms lately? *Clin. Microbiol. Rev.*, **15** (2), 155–166.
- Ergun, S. (1952) Fluid flow through packed columns. *Chem Eng Prog*, **48**, 89–94.

- Flekkøy, E. G. (1993) Lattice Bhatnagar-Gross-Krook models for miscible fluids. *Phys. Rev. E*, **47** (6), 4247–4257.
- Fujie, K.; Kasakura, T.; Tsuchiya, K.; Tomita, Y. (1997) Effects of air diffuser arrangement on hydrodynamics and oxygen transfer in activated sludge aeration tanks. *Environ. Technol.*, **18** (6), 663–668.
- Geesey, G. G.; Richardson, W. T.; Yeomans, H. G.; Irvin, R. T.; Costerton, J. W. (1977) Microscopic examination of natural sessile bacterial populations from an alpine stream. *Can. J. Microbiol.*, **23** (12), 1733–1736.
- Gidaspow, D. (1994) *Multiphase Flow and Fluidization: Continuum and Kinetic Theory Descriptions*; Academic Press.
- Ginn, T. R.; Wood, B. D.; Nelson, K. E.; Scheibe, T. D.; Murphy, E. M.; Clement, T. P. (2002) Processes in microbial transport in the natural subsurface. *Adv. Water Resour.*, **25** (8-12), 1017–1042.
- Gjaltema, A.; Vinke, J. L.; Loosdrecht, M. C. M. van; Heijnen, J. J. (1997) Biofilm abrasion by particle collisions in airlift reactors. *Water Sci. Technol.*, **36** (1), 221–228.
- Godunov, S. K. (1959) A difference method for numerical calculation of discontinuous solutions of the equations of hydrodynamics. *Mat. Sb.*, **89** (3), 271–306.
- Graaf, A. A. van de; Mulder, A.; Slijkhuis, H.; Robertson, L. A.; Kuenen, J. G. (1990) Anoxic ammonium oxidation. In: *Proceedings of the 5th European Congress on Biotechnology*, 338–391; Copenhagen, Denmark: Munksgaard.

- Guo, W.; Ngo, H.-H.; Dharmawan, F.; Palmer, C. G. (2010) Roles of polyurethane foam in aerobic moving and fixed bed bioreactors. *Bioresour. Technol.*, **101** (5), 1435–1439.
- Harremoes, P. (1978) Biofilm kinetics. *Water Pollut. Microbiol.*, **2**, 71–109.
- Harris, N. P.; Hansford, G. S. (1976) A study of substrate removal in a microbial film reactor. *Water Res.*, **10** (11), 935–943.
- Hentzer, M.; Riedel, K.; Rasmussen, T. B.; Heydorn, A.; Andersen, J. B.; Parsek, M. R.; Rice, S. A.; et al. (2002) Inhibition of quorum sensing in *Pseudomonas aeruginosa* biofilm bacteria by a halogenated furanone compound. *Microbiology*, **148** (1), 87–102.
- Henze, M.; Gujer, W.; Mino, T.; Loosdrecht, M. van. (2000) Activated sludge models ASM1, ASM2, ASM2d and ASM3, IWA task group on mathematical modelling for design and operation of biological wastewater treatment; IWA Scientific and Technical Report.
- Hermanowicz, S. W. (1998) A model of two-dimensional biofilm morphology. *Water Sci. Technol.*, **37** (4-5), 219–222.
- Hiatt, W. C.; Grady, C. P. L. J. (2008) An updated process model for carbon oxidation, nitrification, and denitrification. *Water Environ. Res.*, **80** (11), 2145–2156.
- Hilen, E. J. (1923) Report on a bacteriological study of ocean slime. *Rep. Bur. Constr. Repair U. S. Navy Dep. Wash.*, **251**.
- James, G. A.; Beaudette, L.; Costerton, J. W. (1995) Interspecies bacterial interactions in biofilms. *J. Ind. Microbiol.*, **15** (4), 257–262.

- Jefferson, K. K. (2004) What drives bacteria to produce a biofilm? *FEMS Microbiol. Lett.*, **236** (2), 163–173.
- Kaelin, D.; Manser, R.; Rieger, L.; Eugster, J.; Rottermann, K.; Siegrist, H. (2009) Extension of ASM3 for two-step nitrification and denitrification and its calibration and validation with batch tests and pilot scale data. *Water Res.*, **43** (6), 1680–1692.
- Kapellos, G. E.; Alexiou, T. S.; Payatakes, A. C. (2007) Hierarchical simulator of biofilm growth and dynamics in granular porous materials. *Adv. Water Resour.*, **30** (6), 1648–1667.
- Kapellos, G. E.; Alexiou, T. S.; Payatakes, A. C. (2007) A multiscale theoretical model for diffusive mass transfer in cellular biological media. *Math. Biosci.*, **210** (1), 177–237.
- Kissel, J. C.; McCarthy, P. L.; Street, R. L. (1984) Numerical simulation of mixed-culture biofilm. *J. Environ. Eng.*, **110** (2), 393–411.
- Kobayashi, T.; Ohmiya, K.; Shimizu, S. (1976) Approximate expression of effectiveness factor for immobilized enzymes with Michaelis-Menten kinetics. *J. Ferment. Technol.*
- Kreft, J. U.; Booth, G.; Wimpenny, J. W. (1998) BacSim, a simulator for individual-based modelling of bacterial colony growth. *Microbiology*, **144** (12), 3275–3287.
- Kreft, J. U.; Picioreanu, C.; Wimpenny, J. W.; Loosdrecht, M. C. van. (2001) Individual-based modelling of biofilms. *Microbiology*, **147** (11), 2897–2912.

- Kreft, J. U.; Wimpenny, J. W. (2001) Effect of EPS on biofilm structure and function as revealed by an individual-based model of biofilm growth. *Water Sci. Technol.*, **43** (6), 135–142.
- Kreth, J.; Vu, H.; Zhang, Y.; Herzberg, M. C. (2009) Characterization of hydrogen peroxide-induced DNA release by *Streptococcus sanguinis* and *Streptococcus gordonii*. *J. Bacteriol.*, **191** (20), 6281–6291.
- Lazarova, V.; Manem, J. (2000) Innovative biofilm treatment technologies for water and wastewater treatment. In: *Biofilms II: process analysis and applications*, 159–206; Wiley-Liss.
- Leeuwenhoek, A. van; Dobell, C. (1932) *Antony Van Leeuwenhoek and His "Little Animals"*; Staples Press.
- Levenspiel, O. (1962) *Chemical reaction engineering: an introduction to the design of chemical reactors*; Wiley.
- Lin, Y.-H. (2010) Modeling the performance of biodegradation of textile wastewater using polyurethane foam sponge cube as a supporting medium. *Water Sci. Technol.*, **62** (12), 2801–2810.
- Matsui, Y.; Deguchi, H. (2002) The effect of flow pattern on kinetic characteristic of the biomass fixed inside porous medium. *Water Sci. Technol.*, **46** (1-2), 419–422.
- McCarty, P. L.; Reinhard, M. (1981) Trace organics in groundwater. *Environ. Sci. Technol.*, **15** (1), 40–51.
- Mises, R. von. (1913) Mechanik der festen Körper im plastisch- deformablen Zustand. *Nachrichten Von Ges. Wiss. Zu Gött. Math.-Phys. Kl.*, 582–592.

- Morgenroth, E.; Wilderer, P. A. (2000) Influence of detachment mechanisms on competition in biofilms. *Water Res.*, **34** (2), 417–426.
- Morper, M. (1999) Upgrading of Wastewater Treatment Plants with Integration of Existing Facilities. *GWF Wasser - Abwasser*, **140** (14), 22–25.
- Morper, M.; Linde, A. G. (2005) Process Modeling IFAS and MBBR Systems Using LinPor™, Vol. 17; Presented at the Operations and Management, Albuquerque, NM, USA: Rocky Mountain Water Environment Association.
- Nabovati, A.; Llewellyn, E. W.; Sousa, A. (2009) A general model for the permeability of fibrous porous media based on fluid flow simulations using the lattice Boltzmann method. *Compos. Part Appl. Sci. Manuf.*, **40** (6), 860–869.
- National Research council. (1946) Trickling filters in sewage treatment at military installations. *Sew. Works J.*, **18** (5), 787.
- Nguyen, T. T.; Ngo, H. H.; Guo, W.; Johnston, A.; Listowski, A. (2010) Effects of sponge size and type on the performance of an up-flow sponge bioreactor in primary treated sewage effluent treatment. *Bioresour. Technol.*, **101** (5), 1416–1420.
- Niavarani, A.; Priezjev, N. V. (2009) The effective slip length and vortex formation in laminar flow over a rough surface. *Phys. Fluids 1994-Present*, **21** (5), 052105.
- Nielsen, P. H.; Frølund, B.; Keiding, K. (1996) Changes in the composition of extracellular polymeric substances in activated sludge during anaerobic storage. *Appl. Microbiol. Biotechnol.*, **44** (6), 823–830.

- Núñez, M. E.; Martin, M. O.; Chan, P. H.; Spain, E. M. (2005) Predation, death, and survival in a biofilm: *Bdellovibrio* investigated by atomic force microscopy. *Colloids Surf. B Biointerfaces*, **42** (3-4), 263–271.
- Odegaard, H.; Rusten, B.; Badin, H. (1993) Small wastewater treatment plants based on moving bed biofilm reactors. *Water Sci. Technol.*, **28** (10), 351–359.
- Ohashi, A.; Harada, H. (1994) Adhesion strength of biofilm developed in an attached-growth reactor. *Water Sci. Technol.*, **29** (10-11), 281–288.
- Okubo, T.; Matsumoto, J. (1983) Biological clogging of sand and changes of organic constituents during artificial recharge. *Water Res.*, **17** (7), 813–821.
- Onnis-Hayden, A.; Dair, D.; Johnson, C.; Schramm, A.; Gu, A. Z. (2007) Kinetics and Nitrifying Populations in Nitrogen Removal Processes at a Full-Scale Integrated Fixed-Film Activated Sludge (IFAS) Plant. *Proc. Water Environ. Fed.*, **2007** (15), 3099–3119.
- Paul, E.; Ochoa, J. C.; Pechaud, Y.; Liu, Y.; Liné, A. (2012) Effect of shear stress and growth conditions on detachment and physical properties of biofilms. *Water Res.*, **46** (17), 5499–5508.
- Paulsen, J. E.; Oppen, E.; Bakke, R. (1997) Biofilm morphology in porous media, a study with microscopic and image techniques. *Water Sci. Technol.*, **36** (1), 1–9.
- Pérez, J.; Picioreanu, C.; Loosdrecht, M. Van. (2005) Modeling biofilm and floc diffusion processes based on analytical solution of reaction-diffusion equations. *Water Res.*, **39** (7), 1311–1323.

- Peyton, B. M.; Characklis, W. G. (1993) A statistical analysis of the effect of substrate utilization and shear stress on the kinetics of biofilm detachment. *Biotechnol. Bioeng.*, **41** (7), 728–735.
- Phillips, H. M.; Shaw, A.; Sabherwal, B.; Harward, M.; Lauro, T.; Rutt, K. (2007) Modeling Fixed Film Processes: Practical Considerations and Current Limitations from a Consulting Viewpoint. *Proc. Water Environ. Fed.*, **2007** (17), 1571–1583.
- Piciooreanu, C. (1996) Modelling biofilms with cellular automata. Final report to European Environmental Research Organisation; Wageningen, The Netherlands.
- Piciooreanu, C.; Loosdrecht, M. C. M. van; Heijnen, J. J. (1998) Mathematical modeling of biofilm structure with a hybrid differential- discrete cellular automaton approach. *Biotechnol. Bioeng.*, **58** (1), 101–116.
- Piciooreanu, C.; Loosdrecht, M. C. M. van; Heijnen, J. J. (2000) Effect of diffusive and convective substrate transport on biofilm structure formation: A two-dimensional modeling study. *Biotechnol. Bioeng.*, **69** (5), 504–515.
- Piciooreanu, C.; Loosdrecht, M. C. van; Heijnen, J. J. (2001) Two-dimensional model of biofilm detachment caused by internal stress from liquid flow. *Biotechnol. Bioeng.*, **72** (2), 205–218.
- Pintelon, T. R. R.; Graf Von Der Schulenburg, D. A.; Johns, M. L. (2009) Towards optimum permeability reduction in porous media using biofilm growth simulations. *Biotechnol. Bioeng.*, **103** (4), 767–779.

- Reichert, P. (1994) Aquasim - A tool for simulation and data analysis of aquatic systems. *Water Sci. Technol.*, **30** (2 pt 2), 21–30.
- Rittman, B. E. (1982) The effect of shear stress on biofilm loss rate. *Biotechnol. Bioeng.*, **24** (2), 501–506.
- Rittmann, B. E. (1993) The significance of biofilms in porous media. *Water Resour. Res.*, **29** (7), 2195–2202.
- Rittmann, B. E.; Schwarz, A. O.; Eberl, H. J.; Morgenroth, E.; Perez, J.; Loosdrecht, M. van; Wanner, O. (2004) Results from the multi-species benchmark problem (BM3) using one-dimensional models. *Water Sci. Technol.*, **49** (11-12), 163–168.
- Rittmann, B. E.; Trinet, F.; Amar, D.; Chang, H. T. (1992) Measurement of the activity of a biofilm: Effects of surface loading and detachment on a three-phase, liquid-fluidized-bed reactor. *Water Sci. Technol.*, **26** (3-4), 585–594.
- Rodrigues, A. E.; Ahn, B. J.; Zoulalian, A. (1982) Intraparticle-Forced Convection Effect in Catalyst Diffusivity Measurements and Reactor Design. *AIChE J.*, **28** (4), 541–546.
- Roshvanlo, R. B.; Rezaee, A.; Hossini, H.; Shiri, M. (2014) Ammonium removal by nitrification and denitrification in an integrated fixed film activated sludge (IFAS) process. *Health Scope*, **3** (2).
- Sabzali, A.; Nikaeen, M.; Bina, B. (2011) Evaluation of Cigarette Filters Rods as a Biofilm Carrier in Integrated Fixed Film Activated Sludge Process. *World Acad. Sci. Eng. Technol.*, **5**, 82–87.

- Sekizawa, T.; Fujie, K.; Kubota, H.; Kasakura, T.; Mizuno, A. (1985) Air diffuser performance in activated sludge aeration tanks. *J. Water Pollut. Control Fed.*, 53–59.
- Sethian, J. A. (1996) A fast marching level set method for monotonically advancing fronts. *Proc. Natl. Acad. Sci. U. S. A.*, **93** (4), 1591–1595.
- Shapiro, J. A. (1998) Thinking About Bacterial Populations as Multicellular Organisms. *Annu. Rev. Microbiol.*, **52** (1), 81.
- So, M.; Naka, D.; Goel, R.; Terashima, M.; Yasui, H. (2014) Modelling clogging and biofilm detachment in sponge carrier media. *Water Sci. Technol.*, **69** (6), 1298–1303.
- So, M.; Naka, D.; Goel, R.; Yasui, H. (2012) Model Development of a Sponge Carrier Process Using CFD-DEM with Permeable Particles. *J. Water Environ. Technol.*, **10** (2), 193–204.
- Stewart, P. S. (1993) A model of biofilm detachment. *Biotechnol. Bioeng.*, **41** (1), 111–117.
- Stoodley, P.; Lewandowski, Z.; others. (1994) Liquid flow in biofilm systems. *Appl. Environ. Microbiol.*, **60** (8), 2711–2716.
- Succi, S. (2013) *The Lattice Boltzmann Equation: For Fluid Dynamics and Beyond*, Reprint edition.; Oxford: Oxford University Press.
- Tanner, R. S.; Udegbumam, E. O.; McInerney, M. J.; Knapp, R. M. (1991) Microbially enhanced oil recovery from carbonate reservoirs. *Geomicrobiol. J.*, **9** (4), 169–195.

- Thullner, M.; Zeyer, J.; Kinzelbach, W. (2002) Influence of microbial growth on hydraulic properties of pore networks. *Transp. Porous Media*, **49** (1), 99–122.
- Tijhuis, L.; Hijman, B.; Loosdrecht, M. C. M. Van; Heijnen, J. J. (1996) Influence of detachment, substrate loading and reactor scale on the formation of biofilms in airlift reactors. *Appl. Microbiol. Biotechnol.*, **45** (1-2), 7–17.
- Trulear, M. G.; Characklis, W. G. (1982) Dynamics of biofilm processes. *J. Water Pollut. Control Fed.*, **54** (9), 1288–1301.
- Tsuji, Y.; Kawaguchi, T.; Tanaka, T. (1993) Discrete particle simulation of two-dimensional fluidized bed. *Powder Technol.*, **77** (1), 79–87.
- Vandevivere, P. (1995) Bacterial clogging of porous media: A new modelling approach. *Biofouling*, **8** (4), 281–291.
- Vayenas, D. V.; Michalopoulou, E.; Constantinides, G. N.; Pavlou, S.; Payatakes, A. C. (2002) Visualization experiments of biodegradation in porous media and calculation of the biodegradation rate. *Adv. Water Resour.*, **25** (2), 203–219.
- Wanner, O.; Eberl, H.; Morgenroth, E.; Noguera, D.; Picioreanu, C.; Rittman, B. E.; Loosdrecht, M. van. (2006) *Mathematical Modeling of Biofilms*, 1 edition.; London: IWA Publishing.
- Wanner, O.; Gujer, W. (1985) Competition in biofilms. *Water Sci. Technol.*, **17** (2), 27–44.
- Wanner, O.; Gujer, W. (1986) A multispecies biofilm model. *Biotechnol. Bioeng.*, **28** (3), 314–328.

- Wen, C.; Yu, Y. H. (1966) Mechanics of fluidization. *Chem Eng Prog Symp Ser*, Vol. 62, 100.
- Wiesmann, U.; Choi, I. S.; Dombrowski, E.-M. (2007) Historical development of wastewater collection and treatment. *Fundam. Biol. Wastewater Treat.*, 1–23.
- Wilderer, P. A.; Characklis, W. G. (1989) Structure and function of biofilms. *Struct. Funct. Biofilms*, 5–17.
- Wimpenny, J. W. T.; Colasanti, R. (1997) A unifying hypothesis for the structure of microbial biofilms based on cellular automaton models. *FEMS Microbiol. Ecol.*, **22** (1), 1–16.
- Wingender, J.; Neu, T. R.; Flemming, H.-C. (1999) What are Bacterial Extracellular Polymeric Substances? In: *Microbial Extracellular Polymeric Substances* (D. J. Wingender, D. T. R. Neu & P. D. H.-C. Flemming, eds.), 1–19; Springer Berlin Heidelberg.
- Xavier, J. B.; Picioreanu, C.; Loosdrecht, M. C. M. van. (2005) A framework for multidimensional modelling of activity and structure of multispecies biofilms. *Environ. Microbiol.*, **7** (8), 1085–1103.
- Xavier, J. B.; Picioreanu, C.; Loosdrecht, M. C. M. van. (2005) A general description of detachment for multidimensional modelling of biofilms. *Biotechnol. Bioeng.*, **91** (6), 651–669.

9 APPENDICES

APPENDIX 1. RFLOW PRE-PROCESSOR

Constructing the mesh in R-flow Pre-processor

The mesh of the CFD-DEM simulations in R-flow is shown in Figure A.1. The dimensions are 6.85 x 5 x 2 m.

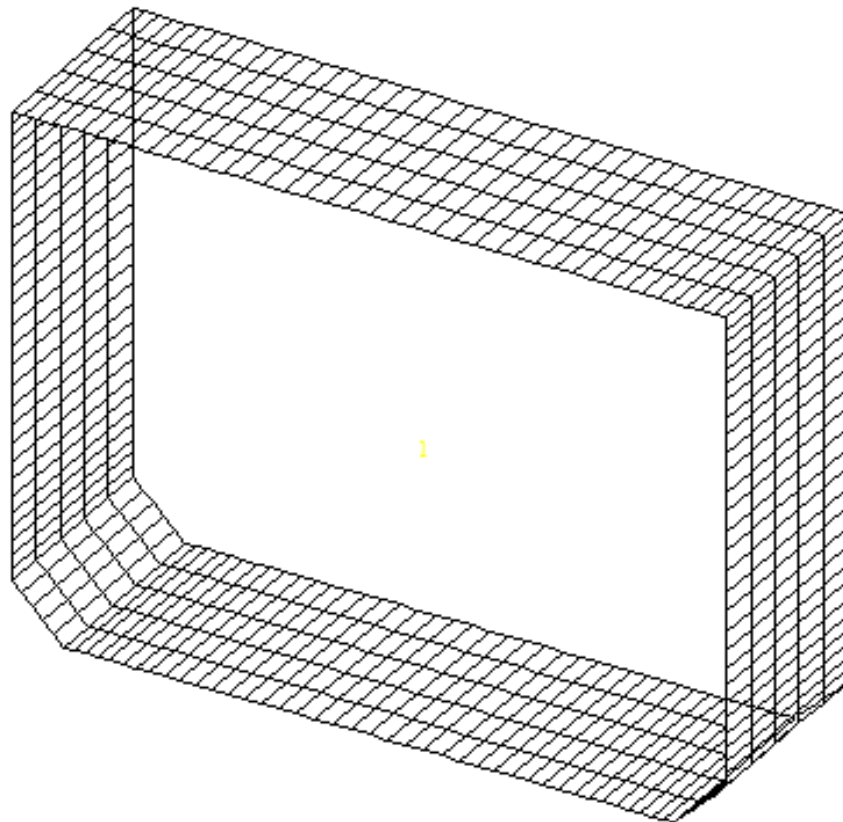


Figure A.1. Mesh generated in the R-flow Pre-processor

Parameters settings of the CFD-DEM simulation in R-flow for the reference simulation

The list of parameters that is given below are the values of the parameters in the CFD-DEM simulation that deviates from the default settings in the pre-processor. The parameters are ordered according to the menu list *Parameter* in RFLOW pre-processor. The parameters are for the reference case, that is an aeration intensity of 4 m/h and sponge diameters of 10 mm.

Control

istead	0	Flag for steady (1) and unsteady (0) flow analysis
iturb	1	Flag for the turbulent model
tmax	1200	Maximum time of the computation (s)
iveloc	1	Flag for fluid velocity analysis

Property

rhomat	1000	fluid density (kg/m ³)
--------	------	------------------------------------

Acceleration

g(z)	-9.8	z component of gravitational acceleration (m/s ²)
------	------	---------------------------------------------------------------

Viscosity

fmu	0.001	viscosity (Pa·s)
-----	-------	------------------

I/O

tintpo	4	Increment of time for post file output (s).
--------	---	---------------------------------------------

Multi-phase flow

nphase	2	Number of dispersed phases (apart from the fluid phase)
--------	---	---------------------------------------------------------

**Parameters for Gas/Solid
/Liquid Particle**

This menu appears when clicking “OK” in “Multi-phase flow” menu

<i>Phase 1</i>		Parameters for air
Diameter	0.03	Diameter of air bubbles in DEM solver (larger than real size)
Density	-1.4	Density of air bubbles (minus sign indicate that bubbles will escape surface)
<i>Phase 2</i>		Parameters for Sponges
Diameter	0.1	Diameter of sponges in DEM solver
Density	1003	Density of sponges

DEM

Basic Settlings

idem	1	Flag for DEM simulation
idemiof	1	Flag for particle flow in/out boundary condition
sprcn	100	Spring constant (normal)
sprct	100	Spring constant (tangential)
rescn	0.7	Restitution coefficient (normal)
rescn	0.7	Restitution coefficient (tangential)
fricc	0.5	Friction coefficient (particles)
fricc	0.5	Friction coefficient (particle-wall)
rsrohnrp	0.4	Ratio of surface roughness to particle radius (for lubrication force)
ndtfdem	10	Ratio of time step of fluid by the time step of DEM
rdpdem	10	Ratio of diameters (computation

Particle

Generate

kmark	1	Phase number to be generated (1 is air)
Start point	0.5, 0.25, 0	$x_{start}, y_{start}, z_{start}$
End point	1.5, 1.75, 0	$x_{end}, y_{end}, z_{end}$
Number of Particles	20, 4, 1	Generates $20 \cdot 4 \cdot 1 = 80$ particles each generation step

Control Parameter

tintpg	0.0750225	Interval of particle generation (using real time)
iturbp	1	Flag for the simulation of particles in a turbulent flow regime
nptclmax	100000	Maximum number of particles
nptgmax	100000	Maximum number of particles for generation

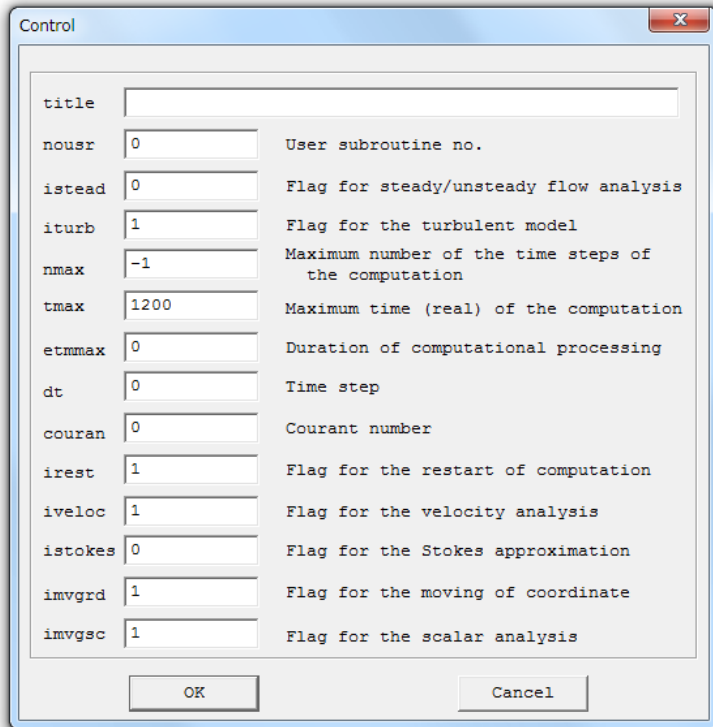


Figure A.2. Menu from the RFLOW presolver to set the control parameters of the simulations

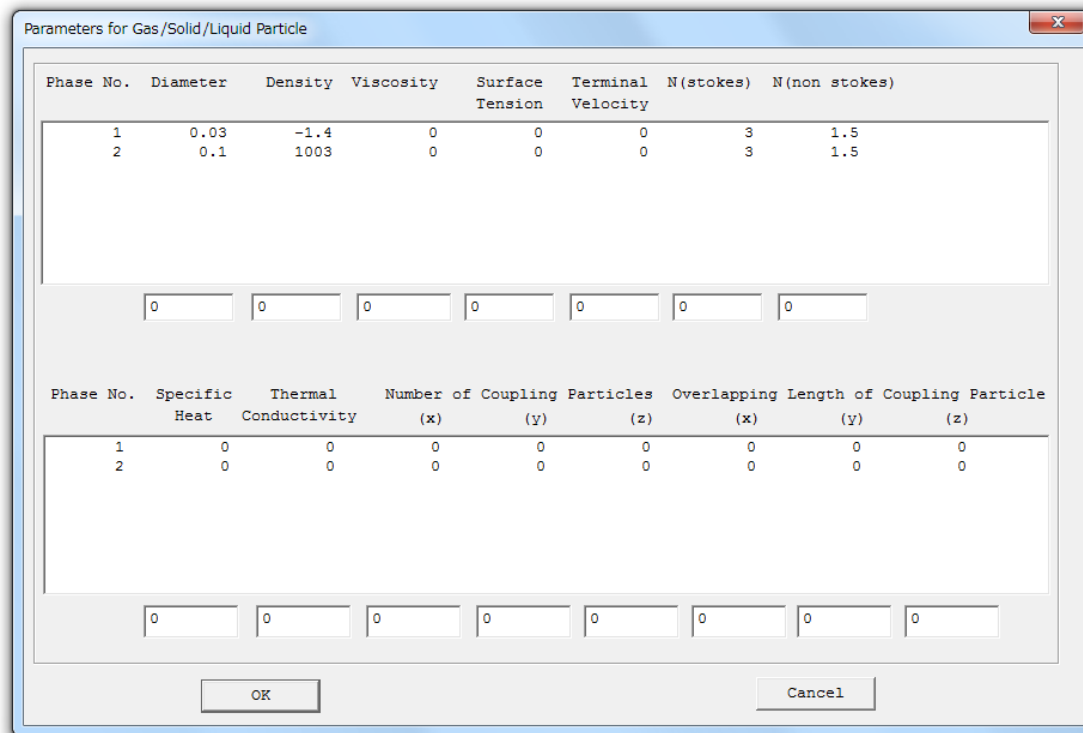


Figure A.3. Menu from the RFLOW pre-processor to set the parameters for particles such as the diameter and the density

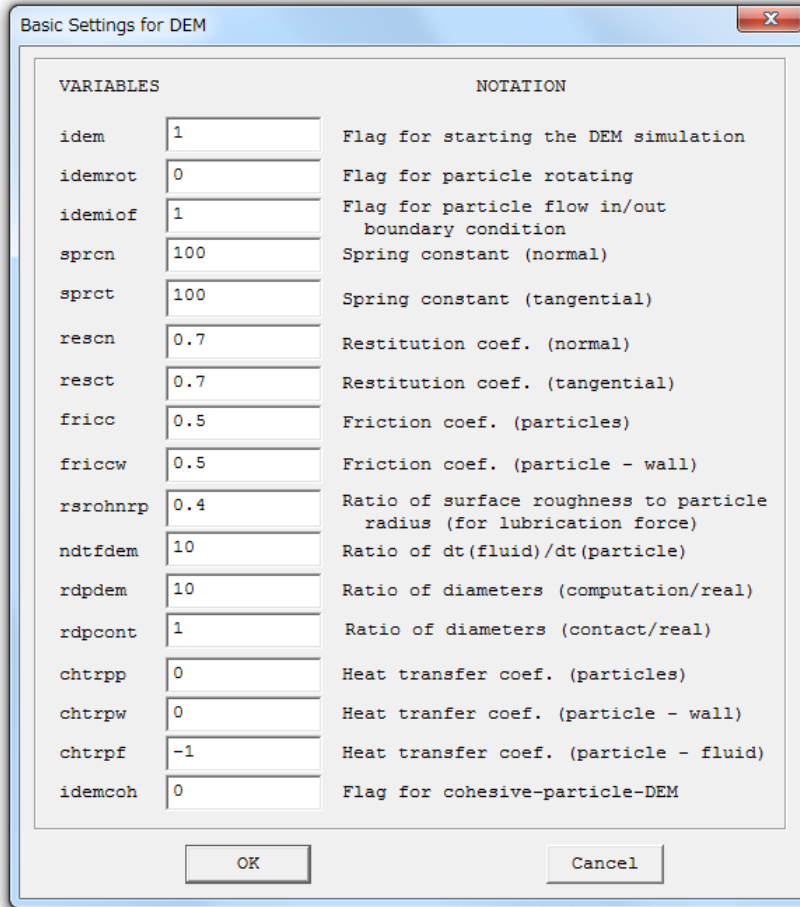


Figure A.4. Menu from the RFLOW pre-processor to set the parameters for the DEM simulation

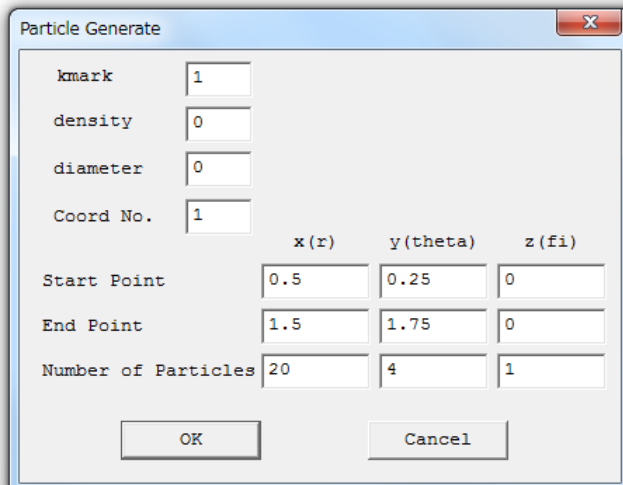


Figure A.5. Menu from the RFLOW pre-processor to set the parameters for particle generation

Parameters settings for different sponge sizes

In the case of a sponge size of 10 mm and bubble size of 3 mm, the ratio of DEM diameter to the real diameter is the same for both air and sponge because the diameters were set to 100 mm and 30 mm respectively in the DEM solver. This made it possible to simulate the real drag force response by adjusting the parameter `Parameter/Control /rdpdem` to a value of 10. In the case of modelling a different sponge size there are two approaches: (i) change the DEM diameter or (ii) change the `rdpdem` for phase 2 (sponge). The first alternative is not very attractive because reducing the DEM diameter by half for 5 mm sponges would require increasing the number of particles by a factor of $2^3 = 8$ which would substantially increase the computation time. Also increasing the DEM diameter for 20 mm sponges might substantially reduce accuracy because of less number of representative particles. Changing `rdpdem` for one phase only needs some special treatment and cannot be done in the pre-processor. Instead the pre text file needs to be edited in the line code where the value of `rdpdem` can be found as indicate in Table A.1.

Table A.1. Change of line code of pre text file for different sponge diameters

	Sponge diameter		
	5 mm	10 mm	20 mm
Line code for <code>rdpdem</code>	<code>rdpdem 10</code> <code>rdpdem(phase) 10 20</code>	<code>rdpdem 10</code>	<code>rdpdem 10</code> <code>rdpdem(phase) 10 5</code>

Parameters settings for different aeration intensities

The aeration intensity was adjusted by changing the time step for particle generation as indicated in Table A.2 by adjusting Parameter/Particle/Control /tintpg.

Table A.2. Adjusting of parameters for different aeration intensities

Aeration intensity (m/h)	Particles generated each time (number)	Time step of particle generation (s)	Rate of particle generation (number/s)
0.25	80	1.20036	67
0.5	80	0.60018	133
1	80	0.30009	267
2	80	0.150045	533
4	80	0.0750225	1066
8	80	0.0325112	2461

APPENDIX 2. NOMENCLATURE IN CHAPTER 3

Table A.3. Nomenclature of variables

Symbol	Value	Expression	Unit	Remark/source
a_b	4200	Biofilm specific area	m^2/m^3	Duan <i>et al.</i> (2006)
d	$5 \cdot 20 \cdot 10^{-3}$	Sponge diameters	m	Assumed
Da	-	Damköhler number	-	Equation 3.9
D_{app}	-	Apparent diffusivity	m^2/s	Equation 3.3
D_{O_2}	$2 \cdot 10^{-9}$	Oxygen diffusion coefficient	m^2/s	Nordling and Österman (1980)
E	-	Effectiveness factor	-	Equation 3.6
g	9.81	Gravitation constant	m/s^2	Nordling and Österman (1980)
H	5	Height of reactor	m	Sekizawa <i>et al.</i> (1985)
J_b	-	Biofilm oxygen flux	g_{O_2}/m^2s	Equation 3.2
$J_{b,bulk}$	-	Biofilm oxygen flux without pore diffusion	g_{O_2}/m^2s	
k	$7 \cdot 10^{-9}$	Permeability of sponges with biofilm	m^2	Nabovati (2009)
K_D	6.8	Empirical constant	-	Curve fit, Figure 3.8
K_{O_2}	0.4	Affinity coefficient	g_{O_2}/m^3	Henze <i>et al.</i> (2000)
$K_{O_2,app}$	1.4	Apparent affinity coefficient on biofilm	g_{O_2}/m^3	Curve fit, Figure 3.3
l_b	10^{-4}	Biofilm thickness	m	Assumed
n	0.5	Empirical coefficient	-	Curve fit, Figure 3.8
p	-	Pressure	Pa	Variable

Multi-scale Modelling of Biofilm in Sponge Carrier Media
Magnus So, September 2014

Q_A	0.25-8	Aeration intensity	m^3/m^2h	Variable
q_{max}	$1.67 \cdot 10^{-4}$	Max. specific OUR	$g_{O_2}/(g_{COD} \cdot s)$	Henze <i>et al.</i> (2000)
r	-	radial position	m	Variable
S_{O_2}	-	Local DO	g_{O_2}/m^3	Variable
$S_{O_2,bulk}$	-	Bulk DO	g_{O_2}/m^3	Variable
u_i	-	Internal velocity	m/s	Equation 7
U_s	-	Sponge slip velocity	m/s	Variable
W	6.85	Width of reactor	m	Sekizawa <i>et al.</i> (1985)
x		Lateral position	m	
X_A	10^4	Autotroph concentration in biofilm	g_{COD-XA}/m^3	Assumed
y		Horizontal position	m	-
α_l		Liquid volume fraction		Variable
α_s		Sponge volume fraction		Variable
κ	1	Constrictivity	-	Assumed
μ	10^{-3}	Dynamic viscosity	Pa·s	Variable
ρ_l	1000	Liquid density	kg/m^3	Assumed
ρ_s	1003	Sponge wet density	kg/m^3	Assumed
λ	-	Peclet number	-	Equation 3.4
τ	1	Turtuosity	-	Assumed
Φ	0.6	Effective porosity of sponges with biofilm	-	Duan <i>et al.</i> (2006)

APPENDIX 3. LIST OF PARAMETERS USED IN CHAPTER 4

Table A.4. Parameter list including values and units

Symbol	Value	Expression	Unit	Remark/source
b_B	0.079	Spec. decay rate of X_B	1/d	Alpqvist <i>et al.</i> (2006)
b_E	0.336	Spec. degradation of X_E	1/d	Alpqvist <i>et al.</i> (2006)
c	1.61	Reduction coefficient	-	
$S_{O_2, bulk}$	2	Bulk DO	g/m ³	
d	0.01	Sponge diameter	m	
D	$2 \cdot 10^{-4}$	Diffusion coefficient	m ² /d	Rittman <i>et al.</i> (2004)
g	$7.32 \cdot 10^{10}$	Standard gravity	m/d ²	
k_{det}	1000	Detachment coefficient	1/m·d	
K_{O_2}	0.35	DO Affinity coefficient	g/m ³	Alpqvist <i>et al.</i> (2006)
Δp	$2.16 \cdot 10^{10}$	Pressure drop	g/m·d ²	Equation (4.1)
Y_B	0.206	Yield of microorganisms	-	Alpqvist <i>et al.</i> (2006)
Y_I	0.4	Yield of inert	-	Alpqvist <i>et al.</i> (2006)
Y_E	0.289	Yield of EPS	-	Alpqvist <i>et al.</i> (2006)
α_S	0.2	Sponge volume fraction	-	
μ_B	4.71	Max. spec. growth of X_B	1/d	Alpqvist <i>et al.</i> (2006)
ν	0.086	Water kinematic viscosity	m ² /d	
ρ_{EPS}	$3.3 \cdot 10^4$	Density of EPS	g/m ³	Xavier <i>et al.</i> (2005)
ρ_S	$1.003 \cdot 10^6$	Sponge wet density	g/m ³	

Multi-scale Modelling of Biofilm in Sponge Carrier Media
Magnus So, September 2014

ρ_W	$1.000 \cdot 10^6$	Water density	g/m^3
ρ_X	$2.0 \cdot 10^5$	Density of X_B and X_I	g/m^3

APPENDIX 4. EQUATION DERIVATIONS, STOICHIOMETRIC TABLES AND PARAMETER LISTS FROM CHAPTER 6

Modelling soluble components in pore water and biofilm

The balance of S_i in pore water in C_k (in sponge) was given as a balance of pore water reactions, biofilm fluxes and pore water fluxes as follows

$$\frac{dS_{i,k}}{dt} = r_{i,k} - a_b j_{i,k} + A_k J_{i,k} - A_{k+1} J_{i,k+1}, \quad 1 \leq k \leq N-1 \quad (\text{A.1})$$

$$\frac{dS_{i,k}}{dt} = r_{i,k} - a_b j_{i,k} + A_k J_{i,k}, \quad k = N \quad (\text{A.2})$$

where $j_{i,k}$ was the flux of $S_{i,k}$ into the biofilm given by

$$j_{i,k} = D \frac{(S_{i,k,LF} - S_{i,k,L})}{\delta_{LB}} \quad (\text{A.3})$$

where subscript L was the pore liquid and δ_{LB} (50 μm) was the thickness of the liquid diffusive boundary layer, covering the biofilm. δ_{LB} was calculated from the Churchill-Bernstein equation for a cylindrical sponge fiber at low Reynolds numbers (Churchill and Bernstein, 1977). The distribution of $S_{i,k}$ inside the biofilm was solved by AQUASIM by a set of partial-differential equations of reaction-diffusion processes (Reichert, 1994).

Calculation of initial internal velocity

The initial internal velocity of an empty sponge, U_{ini} , that appeared in equation (6.4), was calculated from Darcy's law (Bear, 1988) as follows

$$U_{ini} = -\frac{K_{ini}}{\eta} \frac{\partial P}{\partial Z} \quad (\text{A.4})$$

where Z was the vertical coordinate in the fluidized bed reactor, K_{ini} (m^2) was the initial permeability of an empty sponge, η (Pa s^{-1}) was the viscosity and P (Pa) was

the pressure. K can be obtained by combining Darcy law with Kozeny-Carman equation (Bear, 1988) and replacing $d = 6(1-\varepsilon_{ini})/a_b$ as follows

$$K_{ini} = \frac{\psi^2 d^2}{180} \frac{\varepsilon_{ini}^3}{(1-\varepsilon_{ini})^2} = \frac{\psi^2 \varepsilon_{ini}^3}{5a_b^2} \quad (\text{A.5})$$

where ψ was the sphericity of the porous media, ε_{ini} was the empty sponge porosity and d was the granular diameter of the porous medium. By inserting $\psi = 0.77$, $\varepsilon = 0.97$, $a_b = 2800 \text{ m}^2/\text{m}^3$ into equation (A.5), $K_{ini} = 1.4 \cdot 10^{-8} \text{ m}^2$ was estimated. The pressure gradient over a swarm of fluidized sponges of density $\rho_s = 1003 \text{ kg}/\text{m}^3$ in a liquid water with density $\rho_w = 1000 \text{ kg}/\text{m}^3$ could be estimated by assuming the pressure gradient to be in balance with the buoyancy forces as follows

$$\frac{\partial P}{\partial z} = (\rho_s - \rho_w)g\Phi_s \quad (\text{A.6})$$

where $g = 9.8 \text{ m}^2 \text{ s}^{-1}$ was the standard gravity and $\Phi_s = 0.2$ was the volume fraction of sponges. Finally from equation (A.4), $U_0 = 8.3 \cdot 10^{-5} \text{ m}/\text{s} = 7.1 \text{ m}/\text{d}$ could be obtained by using the obtained values of K_{ini} and $\partial P/\partial z = 5.9 \text{ Pa m}^{-1}$.

Table A.5. . Petersen matrix of the simulations

j	Components \rightarrow, i	1	2	3	4	5	6	7	8	9	10	Process rate, ρ_i
	Processes \downarrow	S_B	S_{O_2}	S_{NHX}	S_{NO_3}	S_{NO_2}	X_{OHO}	X_{A00}	X_{N00}	XC_B	X_U	
1	Aerobic growth of heterotrophs	$-\frac{1}{Y_{OHO,O_2}}$	$-\frac{(1 - Y_{OHO,O_2})}{Y_{OHO,O_2}}$				1					$\mu_{OHO,max} \left(\frac{S_{O_2}}{K_{O_2,OHO} + S_{O_2}} \right) \left(\frac{S_B}{K_{B,OHO} + S_B} \right) X_{OHO}$
2	Anoxic growth of heterotrophs on nitrate	$-\frac{1}{Y_{OHO,NO_3}}$			$-\frac{(1 - Y_{OHO,NO_3})}{1.14Y_{OHO,NO_3}}$	$\frac{(1 - Y_{OHO,NO_3})}{1.14Y_{OHO,NO_3}}$	1					$\mu_{OHO,max} \eta_{NO_3} \left(\frac{K_{O_2,OHO}}{K_{O_2,OHO} + S_{O_2}} \right) \left(\frac{S_B}{K_B + S_B} \right) \left(\frac{S_{NO_3}}{K_{NO_3,OHO} + S_{NO_3}} \right) X_{OHO}$
3	Anoxic growth of heterotrophs on nitrite	$-\frac{1}{Y_{OHO,NO_2}}$				$-\frac{(1 - Y_{OHO,NO_2})}{1.72Y_{OHO,NO_2}}$	1					$\mu_{OHO,max} \eta_{NO_2} \left(\frac{K_{O_2,OHO}}{K_{O_2,OHO} + S_{O_2}} \right) \left(\frac{S_B}{K_B + S_B} \right) \left(\frac{S_{NO_2}}{K_{NO_2,OHO} + S_{NO_2}} \right) X_{OHO}$
4	Decay of heterotrophs	$1 - f_U$					-1			$1 - f_U$	f_U	$b_{OHO} X_{OHO}$
5	Growth of A00		$-\frac{3.43 - Y_{A00}}{Y_{A00}}$	$-\frac{1}{Y_{A00}}$		$\frac{1}{Y_{A00}}$		1				$\mu_{A00,max} \left(\frac{S_{O_2}}{K_{O_2,A00} + S_{O_2}} \right) \left(\frac{S_{NHX}}{K_{NHX,A00} + S_{NHX}} \right) X_{A00}$
6	Decay of A00	$1 - f_U$						-1		$1 - f_U$	f_U	$b_{A00} X_{A00}$
7	Growth of N00		$-\frac{1.14 - Y_{N00}}{Y_{N00}}$		$\frac{1}{Y_{N00}}$	$-\frac{1}{Y_{N00}}$			1			$\mu_{N00,max} \left(\frac{S_{O_2}}{K_{O_2,N00} + S_{O_2}} \right) \left(\frac{S_{NO_2}}{K_{NO_2,N00} + S_{NO_2}} \right) X_{N00}$
8	Decay of N00	$1 - f_U$							-1	$1 - f_U$	f_U	$b_{N00} X_{N00}$
9	Hydrolysis	1								-1		$k \left[\frac{XC_B/X_{OHO}}{K_X + XC_B/X_{OHO}} \left(\frac{S_{O_2}}{K_{O_2,OHO} + S_{O_2}} \right) + \eta_h \left(\frac{K_{O_2,OHO}}{K_{O_2,OHO} + S_{O_2}} \right) \left(\frac{S_{NO_2} + S_{NO_3}}{K_{NO_2,OHO} + S_{NO_2} + S_{NO_3}} \right) \right] X_{OHO}$

Table A.6. Parameters used in simulations. If two values are given in bold, the first one indicates values from Matsui and Deguchi (2002) used for the calibrated model and the second value was introduced in this study for the extension to the multispecies model.

Symbol	Value (s)	Expression	Unit	Remark/source
a_b	2800	Specific surface area of biofilm	m^{-1}	Morper (1999)
A_s	500	Specific surface area of sponges per volume sponge	m^{-1}	Morper (1999)
b_{AOO}	0.096	Specific decay rate of X_{AOO}	d^{-1}	Hiatt and Grady (2008)
b_h	0.6	Specific decay rate of X_{OHO}	d^{-1}	Henze <i>et al.</i> (2000)
b_{NOO}	0.096	Specific decay rate of X_{NOO}	d^{-1}	Hiatt and Grady (2008)
c	1.6	Detachment coefficient reduction	-	So <i>et al.</i> (2014)
D	0.0001	Molecular diffusion coefficient	m^2 d^{-1}	Wanner and Gujer (1986)
f_U	0.1	Undegradable fraction from decay	-	Henze <i>et al.</i> (2000)
HRT	0.18, 0.375	Hydraulic retention time	d	Matsui and Deguchi (2002), This study
k_{det}	1000	Detachment coefficient	m^{-1} d^{-1}	Henze <i>et al.</i> (2000)
k_h	3	Max specific hydrolysis rate	d^{-1}	Henze <i>et al.</i> (2000)
$K_{NHX,AOO}$	0.3	Affinity coefficient of X_{AOO} on S_{NHX}	$g\ m^{-3}$	Cuidad <i>et al.</i> (2006)
$K_{NO2,NOO}$	1.1	Affinity coefficient of X_{NOO} on S_{NO2}	$g\ m^{-3}$	Cuidad <i>et al.</i> (2006)

Multi-scale Modelling of Biofilm in Sponge Carrier Media
Magnus So - September 2014

$K_{O_2,A00}$	0.3	Affinity coefficient of X_{A00} on S_{O_2}	$\frac{g}{m^3}$	Cuidad <i>et al.</i> (2006)
$K_{O_2,N00}$	1.4	Affinity coefficient of X_{N00} on S_{O_2}	$\frac{g}{m^3}$	Cuidad <i>et al.</i> (2006)
$K_{NOX,H}$	0.2	Affinity coefficient of X_{OHO} on S_{NO_2} and S_{NO_3}	$\frac{g}{m^3}$	Hiatt and Grady (2008)
$K_{B,OHO}$	4	Affinity coefficient of X_{OHO} on S_B	$\frac{g}{m^3}$	Wanner and Gujer (1986)
K_X	0.03	Affinity coefficient of hydrolysis on X_{CB}	$\frac{g}{m^3}$	Henze <i>et al.</i> (2000)
r	$6 \cdot 10^{-3}$	Radius of sponge	m	This study
$S_{NHX,in}$	0, 30	Influent concentration of S_{NHX}	$\frac{g}{m^3 d^{-1}}$	Matsui and Deguchi (2002), This study
$S_{O_2,bulk}$	0, 2	Oxygen concentrations in bulk	$\frac{g}{m^3}$	This study
$S_{B,in}$	300, 300	Influent concentration of S_B	$\frac{g}{m^3 d^{-1}}$	Matsui and Deguchi (2002), This study
$S_{BN03,in}$	30, 0	Influent concentration of S_{NO_3}	$\frac{g}{m^3 d^{-1}}$	Matsui and Deguchi (2002), This study
U_{ini}	7.1	Internal velocity of an empty sponge	m/d	Equation (A.4)
$X_{F,tot}$	$5 \cdot 10^4$	Concentration of biomass in biofilm	$\frac{g}{m^3}$	This study
Y_{A00}	0.18	Yield coefficient of X_{A00}	-	Hiatt and Grady (2008)
Y_{N00}	0.06	Yield coefficient of X_{N00}	-	Hiatt and Grady (2008)
$Y_{OHO,NOX}$	0.54	Anoxic yield coefficient of X_{OHO}	-	Hiatt and Grady

				(2008)
$Y_{OHO,02}$	0.67	Aerobic yield coefficient of X_{OHO}	-	Henze <i>et al.</i> (2000)
δ_{LB}	$5 \cdot 10^{-5}$	Liquid boundary layer thickness	m	This study
ϵ_{ini}	0.97	Porosity of an empty sponge	-	Morper (1999)
ϵ_{crit}	0.28	Critical hydraulic porosity of sponges	-	This study
η_{NO2}	0.16	Reduction factor for X_{OHO} growth on S_{NO2}	-	Hiatt and Grady (2008)
η_{NO3}	0.28	Reduction factor for X_{OHO} growth on S_{NO3}	-	Hiatt and Grady (2008)
η_h	0.4	Reduction factor for anoxic hydrolysis	-	Henze <i>et al.</i> (2000)
$\mu_{A00,max}$	0.78	Max specific growth rate of X_{A00}	d ⁻¹	Hiatt and Grady (2008)
$\mu_{OHO,max}$	6.25	Max specific growth rate of X_{OHO}	d ⁻¹	Hiatt and Grady (2008)
$\mu_{NO0,max}$	0.78	Max specific growth rate of X_{NO0}	d ⁻¹	Hiatt and Grady (2008)
Φ_s	0.1, 0.2	Volume fraction of sponges	-	Matsui and Deguchi (2002), This study

APPENDIX 5. SHOVING ALGORITHM

```
function [BX,BY] = Shoving_new15(R,BX,BY,x,y,rf,k_shov)
BXT=BX';BYT=BY'; %Coordinates of particles
R3=[k_shov*R';rf]; %Radii of particles
nimax=10; RR= repmat(k_shov*R',1,nimax+1); LBX=length(BX);
i=0; res=1; rmean=mean(k_shov*R);

while i<200 && res > 1e-4
    i=i+1; BX3=[BXT;x]; BY3=[BYT;y];
    BXX=repmat(BXT,1,nimax+1); BYY=repmat(BYT,1,nimax+1);

    %Find nearest neighbour (id10) using knnsearch algorithm
    if mod(i,20)==1 || i==8
        [id10,dist]=knnsearch([BXT BYT],[BXT BYT],'k',nimax+1);
        id10(:,1)=LBX+1; DX=BX3(id10)-BXX; DY=BY3(id10)-BYY;
        dist(:,1)=sqrt(DX(:,1).^2+DY(:,1).^2); %distance
    else
        DX=BX3(id10)-BXX; DY=BY3(id10)-BYY; dist=sqrt(DX.^2+DY.^2);
    end

    ROV=max(RR+R3(id10)-dist,0)/2; %Overlap radii
    BXT=BXT-sum(ROV.*DX./dist,2); BYT=BYT-sum(ROV.*DY./dist,2);

    if mod(i,5)==0
        res=mean(sum(ROV,2)/rmean); %residual convergence check
    end

end
BX=BXT'; BY=BYT';
```

APPENDIX 6. REACTION, ADVECTION AND DIFFUSION ALGORITHM

```
function [C,CB] =
Adv_Diff_React_PL3(C,BOUND,SKELETON,UX,UY,dx,C_bulk,...
    FBH,yi,l_b,ib,jb,Species1,P_VAR,xp,yp,first_flow,BB)

[~,~,~,qmax1,K1,~,rho_b,~,~,~,~,~]=Kinetic_Param(Species1);
[BX,BY,~,~,~,~,~,CB]=Obtain_P_Var(P_VAR(1:8,:));

CC=C';
B=BOUND';SKEL=SKELETON'; H=FBH';
D=2e-9;

%find nodes which are within boundary
iyn=find(yi<0); ybound=yi(1)*sum(sum(B(iyn,:)))/numel(B(iyn,:))-l_b;
i_b=find(yi<ybound);CC(i_b,:)=C_bulk;

[im,jm]=size(UX);
i=2:im-1; e=i+1; w=i-1; j=1:jm; s=mod(j-2,jm)+1;n=mod(j,jm)+1;

U=sqrt(UX.^2+UY.^2);

Umax=max(max(U));

DD=D*ones(size(SKEL)); DD(SKEL==1)=D/10;

Pe_w=UX./DD*dx; Pe_w(isnan(Pe_w))=0;
Pe_s=UY./DD*dx; Pe_s(isnan(Pe_s))=0;

dt=min([dx/Umax,D/Umax^2,K1/(qmax1*rho_b),dx^2/D])/2;

BF=zeros(size(B));BF(i,j)=min(B(i,j)+B(e,j)+B(w,j)+B(i,n)+B(i,s),1);

A=0*CC(i,j); Di=A; R=A; A0=A; Di0=Di;

k=0;res=1;

n_iter=10000;
RES=ones(1,n_iter);

sz=size(CC);

%find skeleton without neighbouring biofilm and set CC to zero
SKEL=SKELETON';
CC(SKEL==1 & (SKEL([2:end 1],:)==1 & SKEL([end 1: end-1],:)==1 & ...
    SKEL(:,[2:end 1])==1 & SKEL(:,[end 1: end-1])==1))=0;

%-----Power law coefficients
AW=DD(w,j).* (max(0,(1-0.1*abs(Pe_w(w,j))))).^5)+max(0,Pe_w(w,j))/dx;
AE=DD(e,j).* (max(0,(1-0.1*abs(Pe_w(e,j))))).^5)+max(0,-Pe_w(e,j))/dx;
```

Multi-scale Modelling of Biofilm in Sponge Carrier Media
Magnus So - September 2014

```

AS=DD(i,s).*(max(0,(1-0.1*abs(Pe_s(i,s))).^5)+max(0,Pe_s(i,s)))/dx;
AN=DD(i,n).*(max(0,(1-0.1*abs(Pe_s(i,n))).^5)+max(0,-Pe_s(i,n)))/dx;

%-----implicit-----
ap0=dx/dt;
AP=AW+AE+AS+AN+UX(e,j)-UX(w,j)+UY(i,n)-UY(i,s)+ap0;

if first_flow
    n_iter=10000;
else
    n_iter=5000;
end

while k<n_iter && res > 1e-8 || k<100

    k=k+1;C0=CC;

    R=-qmax1*CC(i,j)/(K1+CC(i,j)).*H(i,j);
    CC(i,j)=CC(i,j)+dt*R;

    CC(i,j)=(AW.*CC(w,j)+AE.*CC(e,j)+AN.*CC(i,n)+AS.*CC(i,s)...
        +ap0*CC(i,j))./AP;
    CC(isnan(CC))=0;
    CC(end,:)=CC(end-1,:);CC=min(CC,C_bulk);CC=max(CC,0);
    res=mean(mean(abs(C0-CC)/C_bulk));

    RES(k)=res;
    CC(BB==0)=C_bulk;

end

C=CC'; CBB=CC(sz(1)*(ib-1)+jb);
%

[YP,XP]=meshgrid(yp, xp);
BXm=BX;ddx=xp(end)-xp(1)+dx;
ibig=find(BX>xp(end)+dx/2); ismall=find(BX<xp(1)-dx/2);
BXm(ibig)=BX(ibig)-ddx; BXm(ismall)=BX(ismall)+ddx;

CB=interp2(YP,XP,C,BY,BXm);
nann=find(isnan(CB)); CB(nann)=CBB(nann);

```

APPENDIX 7. LATTICE BOLTZMANN METHOD ALGORITHM

This code is a modification of a code developed by Iain Haslam and which can be obtained from

<http://exolete.com/lbm/>

```
function [UX,UY,F]=LB_Haslam_orig(F,BOUND,deltaU,omega)

% 2D Lattice Boltzmann (BGK) model of a fluid.
% c4 c3 c2 D2Q9 model. At each timestep, particle densities
% \ | / propagate outwards in the directions indicated in the
% c5 -c9 - c1 figure. An equivalent 'equilibrium' density is found,
% / | \ and the densities relax towards that state, in a
% c6 c7 c8 proportion governed by omega.
% Iain Haslam, March 2006.

BOUND=BOUND';
t1=4/9; t2=1/9; t3=1/36; c_squ=1/3;
FEQ=F; msize=nx*ny; CI=[0:msize:msize*7];

ON=find(BOUND); %matrix offset of each Occupied Node
TO_REFLECT=[ON+CI(1) ON+CI(2) ON+CI(3) ON+CI(4) ...
            ON+CI(5) ON+CI(6) ON+CI(7) ON+CI(8)];
REFLECTED= [ON+CI(5) ON+CI(6) ON+CI(7) ON+CI(8) ...
            ON+CI(1) ON+CI(2) ON+CI(3) ON+CI(4)];
avu=1; prevavu=1; ts=0; numactivenodes=sum(sum(1-BOUND));
while (ts<10000 & 1e-10<abs((prevavu-avu)/avu)) | ts<500
    % Propagate
    F(:, :, 4)=F([2:nx 1], [ny 1:ny-1], 4); F(:, :, 3)=F(:, [ny 1:ny-1], 3);
    F(:, :, 2)=F([nx 1:nx-1], [ny 1:ny-1], 2); F(:, :, 5)=F([2:nx 1], :, 5);
    F(:, :, 1)=F([nx 1:nx-1], :, 1); F(:, :, 6)=F([2:nx 1], [2:ny 1], 6);
    F(:, :, 7)=F(:, [2:ny 1], 7); F(:, :, 8)=F([nx 1:nx-1], [2:ny 1], 8);
    BOUNCEDBACK=F(TO_REFLECT); %Densities bouncing back at next
timestep
    DENSITY=sum(F, 3);
    UX=(sum(F(:, :, [1 2 8]), 3)-sum(F(:, :, [4 5 6]), 3))./DENSITY;
    UY=(sum(F(:, :, [2 3 4]), 3)-sum(F(:, :, [6 7 8]), 3))./DENSITY;
    UX(1,1:ny)=deltaU; %Increase inlet pressure
    UX(ON)=0; UY(ON)=0; DENSITY(ON)=0;
    U_SQU=UX.^2+UY.^2; U_C2=UX+UY; U_C4=-UX+UY; U_C6=-U_C2; U_C8=-
U_C4;
    % Calculate equilibrium distribution: stationary
    FEQ(:, :, 9)=t1*DENSITY.*(1-U_SQU/(2*c_squ));
    % nearest-neighbours
    FEQ(:, :, 1)=t2*DENSITY.*(1+UX/c_squ+0.5*(UX/c_squ).^2-
U_SQU/(2*c_squ));
    FEQ(:, :, 3)=t2*DENSITY.*(1+UY/c_squ+0.5*(UY/c_squ).^2-
U_SQU/(2*c_squ));
    FEQ(:, :, 5)=t2*DENSITY.*(1-UX/c_squ+0.5*(UX/c_squ).^2-
U_SQU/(2*c_squ));
    FEQ(:, :, 7)=t2*DENSITY.*(1-UY/c_squ+0.5*(UY/c_squ).^2-
U_SQU/(2*c_squ));
    % next-nearest neighbours
    FEQ(:, :, 2)=t3*DENSITY.*(1+U_C2/c_squ+0.5*(U_C2/c_squ).^2-
U_SQU/(2*c_squ));
```

Multi-scale Modelling of Biofilm in Sponge Carrier Media
Magnus So - September 2014

```
FEQ(:, :, 4) = t3 * DENSITY .* (1 + U_C4 / c_squ + 0.5 * (U_C4 / c_squ) .^2 -  
U_SQU / (2 * c_squ));  
FEQ(:, :, 6) = t3 * DENSITY .* (1 + U_C6 / c_squ + 0.5 * (U_C6 / c_squ) .^2 -  
U_SQU / (2 * c_squ));  
FEQ(:, :, 8) = t3 * DENSITY .* (1 + U_C8 / c_squ + 0.5 * (U_C8 / c_squ) .^2 -  
U_SQU / (2 * c_squ));  
F = omega * FEQ + (1 - omega) * F;  
F(REFLECTED) = BOUNCEDBACK;  
prevavu = avu; avu = sum(sum(UX)) / numactivenodes; ts = ts + 1;  
end
```

APPENDIX 8. LEVEL SET METHOD ALGORITHM

```
function [P_VAR,XL,YL,XIN,YIN,F0,BOUND]=...

Level_Set_fast(dx,P_VAR,deltaU,cf,ppp,kdet,dt_b,x,y,c,yi,BOUND,XP,YP)

BOUND=zeros(size(BOUND));

if numel(cf)>5
[BX,BY,R,~,~,~,ipc,~]=Obtain_P_Var(P_VAR(1:8,:));

tags=find(cf(2,:)>0.9 | cf(2,)==0);
tm=[tags(2:end)-1 length(cf)];
r2t=(1.5e-5)^2;

%1. Obtain Solid fraction curves SFH
%6. Loop of liquid boundary regions, solid fraction regions

LT=length(tags);
XL=nan(LT,round(length(cf)/LT*3)); YL=XL; XIN=XL; YIN=XL;

Lxl=0; Lxin=0;

F0=nan(LT,length(x)); LF=0;

REMAIN=zeros(size(BX));

n_ok=0;

for ii=1:LT

    %-----positions at interface-----      OBS ONLY SINGLE
    FIBRE!!!
        x_in=cf(2,tags(ii)+1:tm(ii))'; y_in=cf(1,tags(ii)+1:tm(ii))';
        dx_in=diff([x_in(end);x_in;]); dy_in=diff([y_in(end);y_in;]);
        f00=find((dx_in.^2+dy_in.^2)>r2t);
    %-----

    %if ~isempty(f0)
    if any(f0)
        x_in=x_in(f0); y_in=y_in(f0);
        f0=find(inpolygon(x,y,x_in,y_in));

        if any(f0)
            n_ok=n_ok+1;

            fff=find(ipc==f0);

            bx=BX(fff); by=BY(fff); r=R(fff);
            pa=polyarea(x_in,y_in);
```

Multi-scale Modelling of Biofilm in Sponge Carrier Media
Magnus So - September 2014

```

dd=sqrt(pa*4/pi);
Re=deltaU*dd*1e6;
Sh=0.3+0.62*Re^0.5*500^(1/3);

l_bound=dd/Sh/2;
nd=ceil(l_bound/dx*1.3+1);

x_min=round(min(x_in-nd*dx)/dx)*dx+dx/2;
x_max=round(max(x_in+nd*dx)/dx)*dx-dx/2;
y_min=round(min(y_in-nd*dx)/dx)*dx+dx/2;
y_max=round(max(y_in+nd*dx)/dx)*dx-dx/2;
x_d=x_min:dx:x_max; y_d=y_min:dx:y_max;

[YD,XD]=meshgrid(y_d,x_d); XDS=XD(1:end)'; YDS=YD(1:end)';

nxd=length(x_d); nyd=length(y_d);

DIST_S=nan(nxd,nyd);

for iii=1:length(x_d)
    for jjj=1:length(y_d)

        dist=sqrt(min((x_d(iii)-x_in).^2+(y_d(jjj)-
            y_in).^2));
        if inpolygon(x_d(iii),y_d(jjj),x_in,y_in)
            DIST_S(iii,jjj)=-dist;
        else
            DIST_S(iii,jjj)=dist;
        end
    end
end

%2. Select curves that enclose fibres
%-----positions for liquid boundary-----
%3. Obtain distance function from the solid fraction
    curves
%4. Create liquid boundary curves by slicing the distance
    function at lb
[cf2,~]=contours(y_d,x_d,DIST_S,[l_bound l_bound]);
[cf2]=Contour_connection(cf2,x,y);

xl=cf2(2,2:end)'; yl=cf2(1,2:end)';
if any(xl)

    dx_in=diff([xl(end);xl;]); dy_in=diff([yl(end);yl;]);
    f02=find((dx_in.^2+dy_in.^2)>r2t); xl=xl(f02);
    yl=yl(f02);
    %-----

%-----positions for near surface-----
[cf3,~]=contours(y_d,x_d,DIST_S,[-30e-6 -30e-6]);

```

Multi-scale Modelling of Biofilm in Sponge Carrier Media
Magnus So, September 2014

```

[cf3]=Contour_connection(cf3,x,y);

xn=cf3(2,2:end)'; yn=cf3(1,2:end)';
dx_in=diff([xn(end);xn;]); dy_in=diff([yn(end);yn;]);
f03=find((dx_in.^2+dy_in.^2)>r2t); xn=xn(f03);
yn=yn(f03);

xv=[x1 NaN xn(end:-1:1)']; yv=[y1 NaN yn(end:-
1:1)'];

near_s= inpolygon(bx,by,xv,yv);

[NY_S,NX_S] = gradient(DIST_S,dx);

BXN=bx(near_s==1); BYN=by(near_s==1);
idxnp=knnsearch([YDS XDS],[BYN' BXN'],'k',1);

DISTW_S=ones(size(DIST_S));
for kkk=1:length(f0)
    DISTW_S0=(XD-x(f0(kkk))).^2+(YD-y(f0(kkk))).^2;
    DISTW_S(1:end)=min([DISTW_S(1:end);DISTW_S0(1:end)]);
end
DISTW_S=sqrt(DISTW_S);

DW=DISTW_S(idxnp)';

DXN=-kdet*dt_b*NX_S(idxnp)'.*DW.^2.*exp(-c*BYN./(5e-
3));
DYN=-kdet*dt_b*NY_S(idxnp)'.*DW.^2.*exp(-c*BYN./(5e-
3));

%extrapolate velocities in points to interface
[idxs,~]=knnsearch([BYN' BXN],[y_in x_in],'k',3);

DXS=mean(DXN(idxs),2);
DYS=mean(DYN(idxs),2);

%extrapolate to liquid boundary
idl=knnsearch([y_in x_in],[y1 x1],'k',2);
ULBX=mean(DXS(idl),2); ULBY=mean(DYS(idl),2);

FFX=TriScatteredInterp([[y_in;y1]
[x_in;x1]], [DXS;ULBX]);
FFY=TriScatteredInterp([[y_in;y1]
[x_in;x1]], [DYS;ULBY]);

ULX_S=FFX(YDS,XDS)'; ULY_S=FFY(YDS,XDS)';

n_iter=ceil(max(max(sqrt(ULX_S.^2+ULY_S.^2)))/dx);

[lx,~]=size(DIST_S);

P0=zeros(size(DIST_S));P0(1:end)=1:numel(P0);
Pm=P0(2:end-1,2:end-1); p=Pm(1:end);

e=p+lx; w=p-lx; n=p+1; s=p-1;

```

Multi-scale Modelling of Biofilm in Sponge Carrier Media
Magnus So - September 2014

```

%switch east, west with north, south
an=min(ULX_S(p),0); as=max(ULX_S(p),0);
ae=min(ULY_S(p),0); aw=max(ULY_S(p),0);

for kk=1:n_iter
    ui=DIST_S(p);
    ue=(DIST_S(e)-ui)/dx; uw=(ui-DIST_S(w))/dx;
    un=(DIST_S(n)-ui)/dx; us=(ui-DIST_S(s))/dx;
    DIST_S(p)=ui-(ae.*ue+aw.*uw+an.*un+as.*us)/n_iter;
end

[x_in,y_in]=Slice(YD,XD,DIST_S,0);
[x_det,y_det]=Slice(YD,XD,DIST_S,0);
[xl,yl]=Slice(YD,XD,DIST_S,l_bound);

Lxl0=length(xl); Lxl=max(Lxl,Lxl0);
XL(n_ok,1:Lxl0)=xl; YL(n_ok,1:Lxl0)=yl;
Lxin0=length(x_in); Lxin=max(Lxin,Lxin0);
XIN(n_ok,1:Lxin0)=x_in; YIN(n_ok,1:Lxin0)=y_in;

LF0=length(f0); LF=max(LF0,LF); F0(n_ok,1:LF0)=f0;

if kdet>0 && length(BX)>100 && mean(DW)>2*dx && ppp>5
    in=inpolygon(bx,by,x_det,y_det) | by>yi(end)-2*dx;
else
    in=ones(size(fff));
end
REMAIN(fff(in))=1;

in2=inpolygon(XP(1:end),YP(1:end),x_det,y_det);
BOUND(in2)=1;

end
end
end
if ppp>5

P_VAR=P_VAR(:,REMAIN==1);
end

XL=XL(1:n_ok,1:Lxl); YL=YL(1:n_ok,1:Lxl); XIN=XIN(1:n_ok,1:Lxin);
YIN=YIN(1:n_ok,1:Lxin);
F0=F0(1:n_ok,1:LF);

end

figure(3)
clf
hold on
if ppp>5
    plot(BY(REMAIN==0),BX(REMAIN==0),'r')
end
plot(YIN',XIN','k',YL',XL','b')
pause(eps)

```